2016

Circumstellar Dust Shells: Clues to the Evolution of R Coronae Borealis Stars

Edward Joseph Montiel
Louisiana State University and Agricultural and Mechanical College, edward.j.montiel@gmail.com

CIRCUMSTELLAR DUST SHELLS: CLUES TO THE EVOLUTION OF R CORONAE BOREALIS STARS

A Dissertation

Submitted to the Graduate Faculty
of the Louisiana State University and
Agricultural and Mechanical College
in partial fulfillment of the
requirements for the degree of
Doctor of Philosophy

in

The Department of Physics and Astronomy

by
Edward Joseph Montiel
B.S., The University of Arizona, 2010
M.S., Louisiana State University, 2015
August 2016

For Lynne, Ida, and Michael

Acknowledgements

"If I have seen further it is by standing on the shoulders of giant" is an expression that Isaac Newton used in a letter to Robert Hooke to describe how his successes were only possible due to the previous work of others. I have also been extremely fortunate to stand on the shoulders of some incredible giants during the pursuit of my Ph.D. I would like to start by thanking my mother, Lynne Montiel, Bubby, Ida Weintraub, and younger brother, Michael Montiel. Their combined love and support have carried me throughout this entire process. I would also like to thank, on an equal level, my advisor, Geoffrey Clayton. There is no way that I would be finishing in four years without your incomparable skill to rein me in whenever I started to stray too far from or too long on any one task. I want to thank Jarita Holbrook for all of the mentorship she has provided me ever since I showed up at her office in Tucson as a wide–eyed freshman. To Jay Lockman, thank you for being so patient in teaching me how to be a radio astronomer. To the other members of the RCB community: Tom Geballe, Warrick Lawson, Patrick Tisserand, and Doug Welch, thank you for all of the feedback and encouragement you have provided.

I would like to acknowledge all of the exceptional research mentors I have had the privilege of working with over my very short career: Gina Brissenden, Heather Morrison, Paul Smith, Kenneth Mighell, Charles Engelbracht, Joannah Hinz, Karl Misselt, Kate Su, and Margaret Meixner. I'm forever indebted that you took a chance on working with me, for making me a better astronomer and person, and for continuing to support me in the form of countless letters of recommendations. Further, I would like to say to Charles Engelbracht, who passed away much too soon, that I miss you everyday.

I would also like to thank the numerous friends that I have made over the years. You are simply too many to list and I hope that you will not take any omission as a slight. To Chris Johnson, thank you for being the best "comrade–in–arms", from the start of graduate school to the finish it has been a great adventure. To everyone that made my stay in Louisiana one of the best experiences of my life: Alison Dreyfuss, Robert Baker, Jon Brown, Robin Cobb, Jon Cripe, Elissa DeLoach, Zach Edwards, Aaron Grocholski, Brittany Fortmayer, Anton Joe, Kundan Kadam, Marianne Konikoff, Kelsie Krafton, Amber Lauer, Amy LeBleu, Ishita Maity, Dominic Marcello, Ischelle Martin, Noah Morris, Kat Munley, Jonny Olson, D. J. Pleshinger, Alison Schreckengast, Paige Thibodeaux, Zhichao Xue, Julia Yarbrough. To Rachelle Baker, Sean Cronin, Jeremy Disque, Jason Dittmann, Shannon Macke, Colin Meyers, Drew Milsom, Rita Morris, Leigh Moyer, Trevor Olson, Jesse Ross, Chris Stanley, Sarah Wiersma, Chris Wittoesch thank you likewise for all of the wonderful experiences in Tucson and beyond.

Table of Contents

Acknowledgements . . . iii

List of Tables . . . vi

List of Figures . . . vii

Abstract . . . ix

1. Introduction . . . 1
    1.1 R Coronae Borealis Variables . . . 1
    1.2 Single vs. Double Degenerate Origins . . . 2
        1.2.1 Stellar Mass & Multiplicity . . . 3
        1.2.2 Elemental Abundances . . . 5
        1.2.3 Diffuse Dust Shells . . . 6
    1.3 Goals . . . 8

2. Observations and Analysis . . . 9
    2.1 Observations . . . 9
        2.1.1 Ultraviolet Data . . . 10
        2.1.2 Optical Monitoring . . . 13
        2.1.3 Near Infrared Monitoring . . . 14
        2.1.4 Two Micron All Sky Survey . . . 14
        2.1.5 Infrared Space Observatory . . . 14
        2.1.6 Spitzer Space Telescope . . . 15
        2.1.7 Wide-field Infrared Survey Explorer . . . 15
        2.1.8 AKARI . . . 15
        2.1.9 Infrared Astronomical Satellite . . . 16
        2.1.10 Herschel Space Observatory . . . 16
        2.1.11 Radio . . . 17
    2.2 Spectral Energy Distribution Modeling . . . 17
        2.2.1 Photometry . . . 17
        2.2.2 MOCASSIN . . . 20

3. What is the Shell Around R Coronae Borealis? . . . 23
    3.1 Origin of the R CrB Dust Shell . . . 23
        3.1.1 The R CrB Dust Shell . . . 23
        3.1.2 A Planetary Nebula Shell? . . . 23

3.1.3 Mass Loss from a White Dwarf Merger? . . . 26
3.1.4 RCB Phase Mass Loss? . . . 27
3.2 Chapter Summary . . . 28

4. The Circumstellar Shells of R Coronae Borealis Stars . . . 29
4.1 MV Sgr . . . 29
4.1.1 Image Inspection . . . 29
4.1.2 Radiative Transfer Modeling . . . 30
4.2 R CrB . . . 33
4.2.1 Image Inspection . . . 33
4.2.2 Radiative Transfer Modeling . . . 35
4.3 RY Sgr . . . 38
4.3.1 Image Inspection . . . 38
4.3.2 Radiative Transfer Modeling . . . 41
4.4 SU Tau . . . 44
4.4.1 Image Inspection . . . 44
4.4.2 Radiative Transfer Modeling . . . 48
4.5 UW Cen . . . 51
4.5.1 Image Inspection . . . 51
4.5.2 Radiative Transfer Modeling . . . 52
4.6 V854 Cen . . . 55
4.6.1 Image Inspection . . . 55
4.6.2 Radiative Transfer Modeling . . . 56
4.7 V CrA . . . 59
4.7.1 Image Inspection . . . 59
4.7.2 Radiative Transfer Modeling . . . 61
4.8 Sample Properties . . . 63
4.8.1 CSM Morphology . . . 63
4.8.2 Envelope Masses & Decline Activity . . . 66
4.8.3 Comparison to an HdC Star & FF Object . . . 68
4.9 MCRT Model Summary . . . 74

5. Discussion & Conclusions . . . 76

Bibliography . . . 81

Appendix. Permission to Reproduce Copyrighted Material . . . 90
A.1 Copyright Agreement with AAS . . . 90
A.2 Permission to use Figure 1.2 . . . 90
A.3 Permission to use Figure 1.3 . . . 91
A.4 Permission to use Figure 1.4 . . . 91
A.5 Permission to use Figure 1.5 . . . 91
A.6 Permission to use Figure 4.20 . . . 92

Vita . . . 93

List of Tables

2.1 Stellar Properties and New Observations of Sample RCB Stars 9

3.1 Model Results 27

3.2 Shell Types 27

4.1 MV Sgr Photometry 31

4.2 R CrB Photometry 36

4.3 RY Sgr Photometry 42

4.4 SU Tau Photometry 49

4.5 UW Cen Photometry 53

4.6 V854 Cen Photometry 57

4.7 V CrA Photometry 62

4.8 V605 Aql Photometry 69

4.9 HD 173409 Photometry 72

5.1 Derived MOCASSIN Properties and Measured Outer Radii 78

List of Figures

1.1 AAVSO Lightcurve of UW Cen from 1975 to 2005 2

1.2 RCB Mass Determination via Pulsation Analysis 4

1.3 NIR Spectra of RCB stars showing ^{18}O 5

1.4 Optical Spectra of RCB stars showing ^{19}F 6

1.5 IRAS 100 μm Contour Map of the R CrB Shell 7

2.1 AAVSO Light Curves of R CrB & RY Sgr 10

2.2 AAVSO Light curves of SU Tau & UW Cen 11

2.3 AAVSO Light Curves of V854 Cen & V CrA 12

2.4 AAVSO Light Curve of MV Sgr 13

2.5 Cartoon of Aperture Photometry 18

2.6 *Spitzer*/MIPS PSFs 19

2.7 *Herschel*/PACS PSFs 19

2.8 *Herschel*/SPIRE PSFs 20

2.9 MOCASSIN Dust Grid Accounting for Spherical Symmetry 21

2.10 MOCASSIN Dust Grid for a Full Sphere 22

3.1 L–band Observation of the Field containing R CrB 24

3.2 Background–Subtracted Temperature vs. HI Velocity of Field around R CrB 25

4.1 *Spitzer* Observations of MV Sgr 30

4.2 MOCASSIN fit of the MV Sgr SED 32

4.3 *Spitzer* & *Herschel* Observations of R CrB 34

4.4 MOCASSIN fit of the R CrB SED 37
4.5 *Spitzer* & *Herschel* Observations of RY Sgr 40
4.6 MOCASSIN fit of the RY Sgr SED 43
4.7 *Spitzer* & *Herschel* Observations of SU Tau 45
4.8 3–color *Herschel*/PACS & *Herschel*/SPIRE Image of SU Tau 46
4.9 Zoom of the SU Tau Bow Shock 47
4.10 *Herschel* & 2MASS Observations of the SU Tau Bow Shock 48
4.11 MOCASSIN fit of the SU Tau SED 50
4.12 *Spitzer* and *Herschel* Observations of UW Cen 52
4.13 MOCASSIN fit of the UW Cen SED 54
4.14 *Spitzer* Observations of V854 Cen 56
4.15 MOCASSIN fit of the V854 Cen SED 58
4.16 *Spitzer* & *Herschel* Observations of V CrA 60
4.17 MOCASSIN fit of the V CrA SED 61
4.18 Single Shell Comparison 64
4.19 Thick vs. Thin Shells 65
4.20 V605 Aql SED presented by Clayton et al. (2013b) 70
4.21 *Herschel* Observations of HD 173409 71
4.22 Blackbody fitting of the HD 173409 SED 73

Abstract

The existence of extended, cold dust envelopes surrounding R Coronae Borealis (RCB) stars has been known about for over 30 years. RCB stars are an exotic group of extremely hydrogen-deficient, carbon-rich supergiants that are known for their spectacular declines in brightness (up to 8 mags) at irregular intervals. There are three possible origins of these envelopes: (1) they are fossil planetary nebulae (PNe), indicating that RCB stars formed via a final Helium-shell flash; (2) they are the remnant material from the merger of a CO and a He white dwarf binary, (3) they have been constructed from dust ejection events during the current phase of the central stars. In the first scenario we expect to find the shell H–rich, while in the remaining two scenarios the shell is H–poor.

I have directly investigated the hydrogen abundance of the envelope surrounding R Coronae Borealis, itself, with archival observations from the Galactic Arecibo L-band Feed Array HI (GALFA-HI) Survey. Further, I have examined new and archival *Spitzer* Space Telescope and *Herschel* Space Observatory images in the far infrared and submillimeter of these envelopes to examine the morphology of these dusty shells. *Herschel* has, in particular, revealed the first ever bow shock associated with an RCB star with its observations of SU Tauri. I have also put together some of the most comprehensive spectral energy distributions (SEDs) of these stars ever made with multi–wavelength data from the ultraviolet to the submillimeter. I will discuss all these results and their implications for the origins of the circumstellar material of RCB stars and the origins of RCB stars themselves.

1. Introduction

A complete observational and theoretical understanding of stellar evolution is one of the fundamental goals of astrophysics. Over the past century, myriad advances and discoveries have contributed to filling in the details of this picture. The later phases of stars' lives progress more rapidly than their earlier ones (e.g., a star will spend $\sim$ 90% of its lifetime as a main sequence star). This makes observing these later periods more difficult due to their short nature. R Coronae Borealis (RCB) stars comprise a peculiar and transitory phase that also offers an excellent opportunity to reveal crucial insights into the advanced stages of stellar evolution.

1.1 R Coronae Borealis Variables

The first star of this class, R Coronae Borealis (R CrB), was discovered to be variable over two centuries ago (Pigott & Englefield, 1797). Since the discovery of R CrB, the known population of RCB stars has only grown to about 150 stars in the Galaxy and the Magellanic Clouds (MC) (Clayton, 1996, 2012; Alcock et al., 2001; Zaniewski et al., 2005; Tisserand et al., 2008; Kraemer et al., 2005; Tisserand et al., 2013; Tisserand et al. 2016, in prep). The hallmark behavior of RCB stars are brightness fluctuations that are manifested in extreme, irregular declines as demonstrated in Figure 1.1. These declines can take an RCB star up to 9 magnitudes fainter than its peak brightness.

The culprit for these declines, the formation of thick carbon dust, has also been determined for some time (Loreta, 1935; O'Keefe, 1939). The dust does not condense in complete shells but rather in discrete clouds (Clayton, 1996), which means that a cloud must condense along the line of sight for a decline to occur. It is less understood how these clouds condense out of the stellar atmosphere before moving outward to join the surrounding circumstellar medium (CSM). It is thought that the stellar pulsations, which RCB stars also exhibit in addition to their declines, cause temperature and density perturbations that help promote dust formation (Feast, 1986; Woitke et al., 1996; Crause et al., 2007).

In addition to this behavior, the composition of RCB stars is nothing short of bizarre. The RCB stars are largely cool (T_{eff} = 5,000–7,000 K), carbon-rich supergiants but have almost no hydrogen. Adding to the mystery of this stellar class is the existence of a small subgroup that is significantly hotter (T_{eff} = 15,000–20,000 K) than the rest of the RCB stars (De Marco et al., 2002; Clayton et al., 2011b). The overwhelming majority of RCB stars have an atmospheric abundance that is $\sim$98%

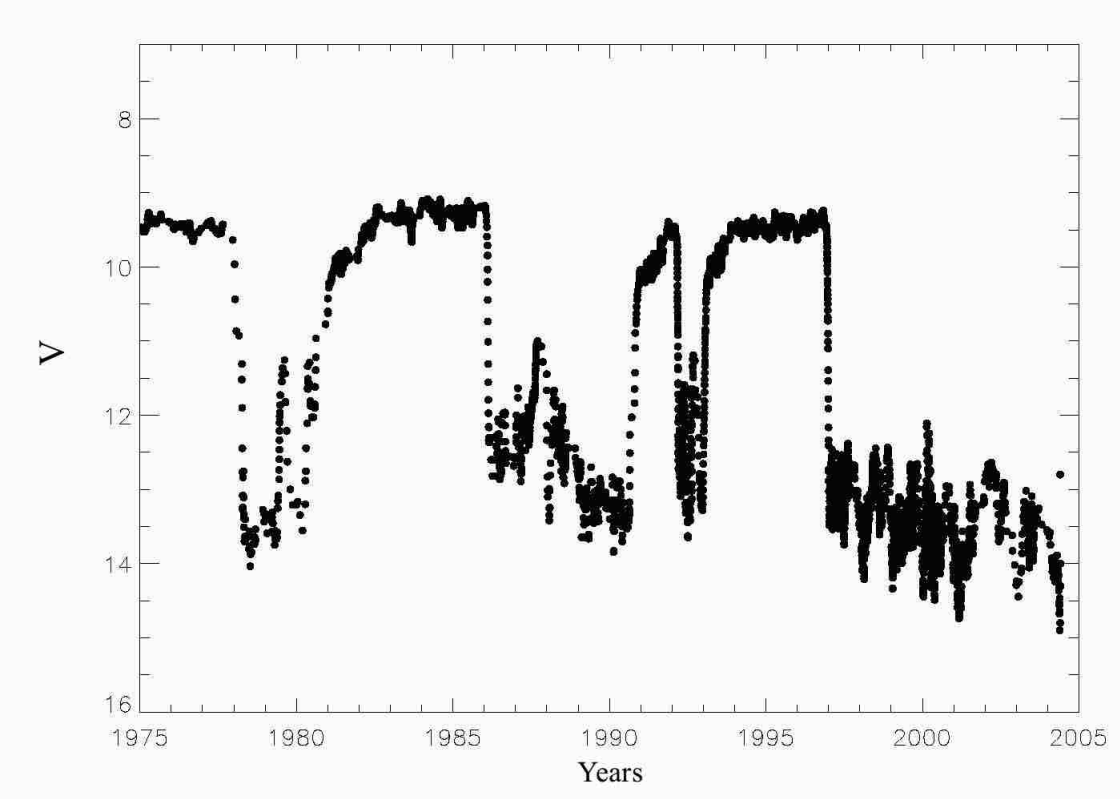

Figure 1.1: American Association of Variable Star Observers (AAVSO) light curve of the RCB star UW Centauri (UW Cen) spanning from 1975 to 2005. Notice the irregularity in both the onset of the declines and the recovery time to maximum light. Variations in the light curve at maximum light are also visible due to intrinsic pulsation.

He and 1% Carbon. The exceptions to this composition are two of the hot RCB stars, V348 Sagittarii and HV 2671, which appear to be 50% He and 50% Carbon (De Marco et al., 2002; Clayton, 2012).

Further, RCB stars are excellent laboratories for studying carbon chemistry (Feast, 1986; Woitke et al., 1996; Rao & Lambert, 2010). IR spectra of most RCB stars are featureless indicating that the dust is likely amorphous carbon but recent observations have revealed the presence of complex carbon bonding, in the form of C60 and C70 emission, taking place around some RCB stars (García-Hernández et al., 2011a, 2012).

1.2 Single vs. Double Degenerate Origins

Two formation scenarios have been proposed for the origin of RCB stars: the single degenerate (SD) final helium-shell flash (FF) model and the double degenerate (DD) white dwarf (WD) merger model (Iben et al., 1996; Saio & Jeffery, 2002). The latter involves the merger of a CO and a He WD (Webbink, 1984), which could produce the unique isotopic abundances found in the RCB stars (see below). While the former takes the hot evolved central star of a planetary nebula (PN) and turns it into a cool

supergiant (Fujimoto, 1977; Renzini, 1979).

The identification of the proper progenitors of RCB stars has not been a case of simply collecting evidence to explain the observed properties of this stellar class. Some RCB characteristics point towards formation via the DD scenario while others point to the FF scenario. This means that both channels are possibly producing RCB stars, and it is important to know the relative percentage of RCB stars made from each channel. However, further complicating this matter is that some properties are common between both scenarios. Hence, those properties cannot be used to distinguish between scenarios. A review of the observed properties and how they support or reject one of the formation scenarios is presented below.

1.2.1 Stellar Mass & Multiplicity

RCB stars show periodic or semi–periodic light and radial velocity fluctuations due to both radial and non–radial pulsations (see Figure 1.1). These stars show pulsation periods in the 40–100 d range (Lawson et al., 1990a). These variations are separate from the large declines in brightness caused by dust forming around the star. The pulsations in RCB stars are thought to arise through strange–mode instabilities. Strange modes occur in stars with high luminosity where radiation pressure dominates (Saio 2008, and references therein).

RCB stars are thought to be $\sim$0.8-0.9 $M_{\odot}$ from stellar pulsation modeling of WD merger products, as shown in Figure 1.2 (Saio, 2008). This estimated mass agrees well with the predicted mass of the merger products of a CO- and a He-WD (Han, 1998). Final–flash stars, since they are single white dwarfs, should typically have masses of 0.55-0.6 $M_{\odot}$ (Bergeron et al., 2007). To date, the only RCB star in a known binary is DY Cen (Rao et al., 2012). It is, however, part of the small subset of RCB stars that have effective temperatures between 15,000 and 20,000 K.

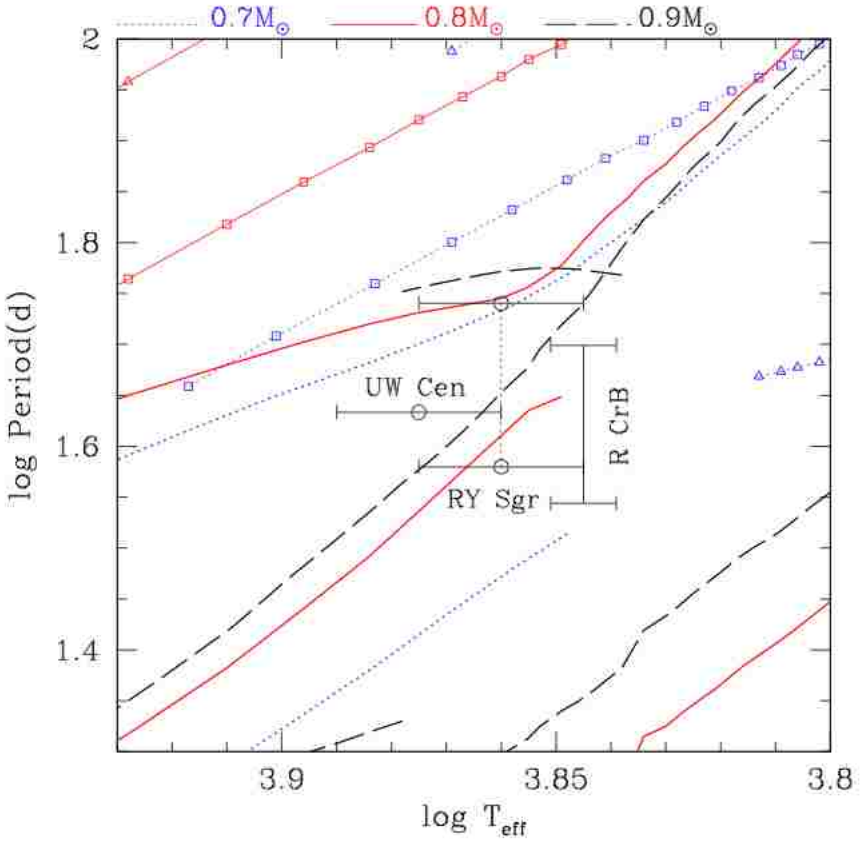

Figure 1.2: Periods of radial and non–radial pulsations excited in the luminous hydrogen–deficient star models versus effective temperature for a parameter range appropriate for pulsations of RCB stars. Lines with and without symbols are for nonradial and radial pulsations of RCB stars, respectively. Lines with triangles are for non–radial l = 1 modes, and lines with squares are for non–radial l = 2 modes (Saio, 2008).

1.2.2 Elemental Abundances

Most amazingly, in the last decade RCB stars were found to have unique chemical abundances. Clayton et al. (2005, 2007) discovered that RCB stars have $^{16}O/^{18}O$ ratios (see Figure 1.3) that are $\sim$500 times lower than the Sun or any known star. Soon after, Pandey et al. (2008) found that ^{19}F was also overabundant, see Figure 1.4. The combination of extreme levels of ^{18}O and ^{19}F, which are both by-products of partial He-burning, suggests that additional nucleosynthesis must have occurred but was then interrupted and ultimately quenched during the formation of the RCB stars (Menon et al., 2013).

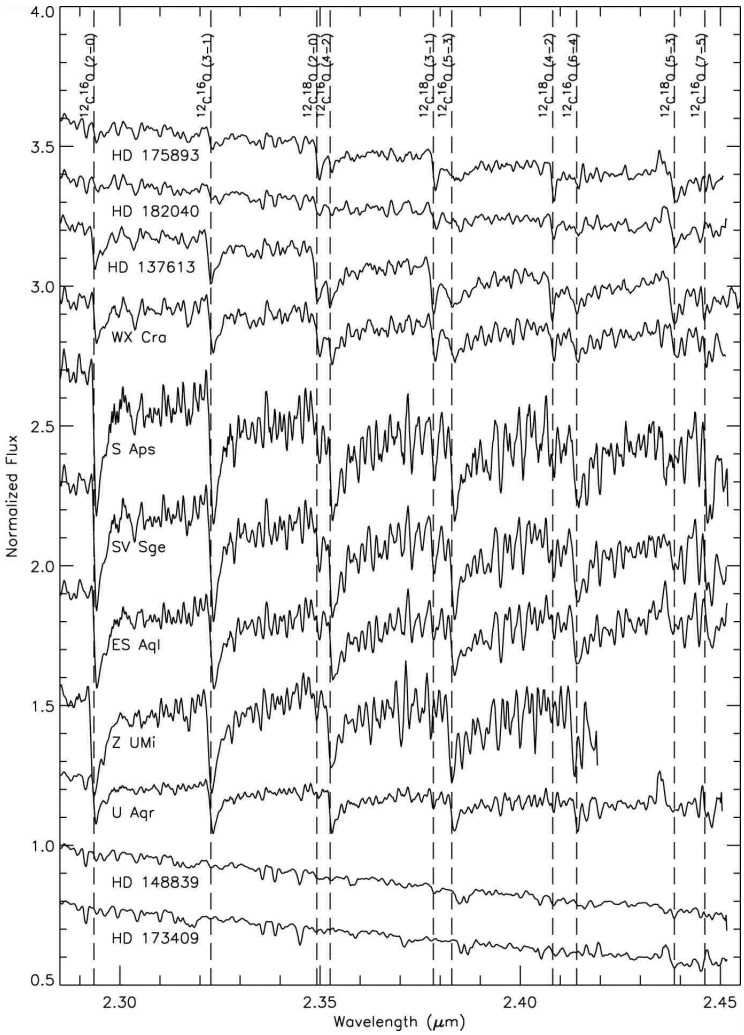

Figure 1.3: The discovery of excess ^{18}O in RCB stars by Clayton et al. (2007) is one of the strongest indicators that RCB stars are possibly the products after the merger of binary WDs.

However, several RCB stars show significant Li in their atmospheres (e.g., Asplund et al., 2000). Renzini (1990) suggested that in a final flash the ingestion of the H-rich envelope leads to Li production through the Cameron–Fowler mechanism (Cameron

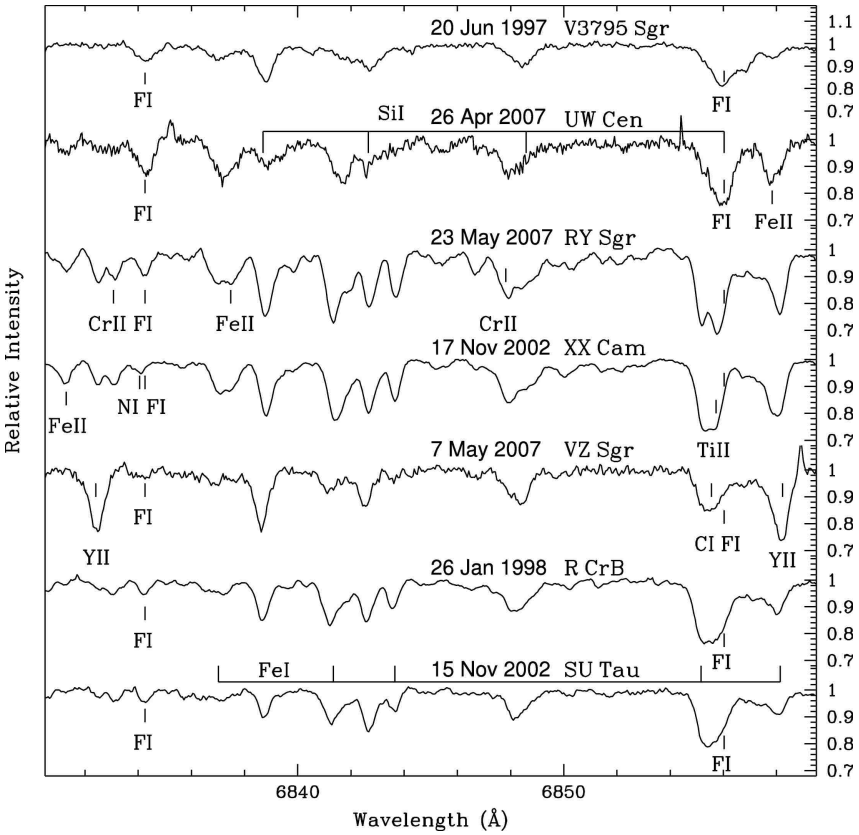

Figure 1.4: Figure originally published in Pandey et al. (2008), who discovered the overabundance of ^{19}F in RCB stars. The enrichment of ^{19}F is also evidence for the scenario that RCB stars are the product of WD mergers.

& Fowler, 1971). Yet, the production of ^{18}O and ^{19}F requires temperatures large enough to completely destroy any Li present. The presence of Li in some RCB stars, as well as in Sakurai's object, is extremely difficult to explain with a WD merger (Asplund et al., 1998). Sakurai's Object, a final-flash star, shows no evidence for enhanced ^{18}O (Geballe et al., 2002).

Hence, the simultaneous enrichment of Li, ^{18}O, and ^{19}F is not expected in the WD merger or final flash scenarios. No RCB star has been found to be simultaneously enriched in Li, ^{18}O, and ^{19}F (Clayton, 2012). However, recent studies have suggested that modeling has ignored the presence of ^{3}He during the merger, which, also via the Cameron-Fowler mechanism, could explain the coexistence of ^{18}O, ^{19}F and Li following a WD merger (Longland et al., 2012; Zhang & Jeffery, 2012; Menon et al., 2013).

1.2.3 Diffuse Dust Shells

The dust shells surrounding the RCB stars may provide important clues to their evolution. Extended infrared dust shells were first detected around several RCB stars, as shown in Figure 1.5 with IRAS (Walker, 1985; Gillett et al., 1986). One

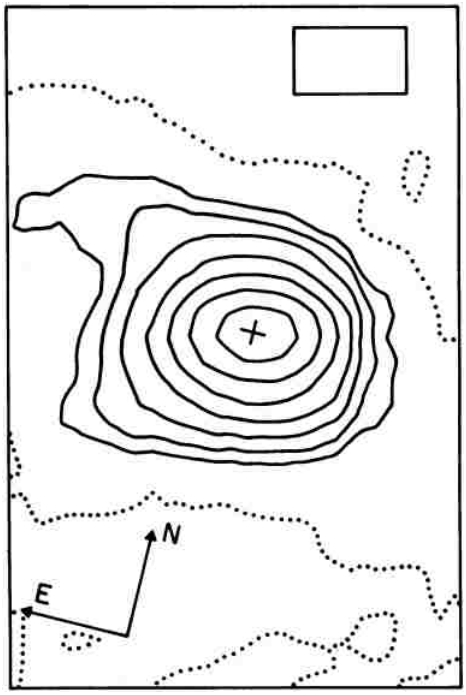

Figure 1.5: Contour map of the IRAS 100 μm observation of R CrB from Gillett et al. (1986). The cross represents the position of R CrB, while the contours trace out the large shell ($18'$) that had been discovered. Dashed lines represent the median surface brightness of the entire pointed observation map, which is larger than region shown. The rectangular box represents the size of the IRAS detector, which was $3'\times5'$.

important difference between the RCB stars formed in the two scenarios is that in the FF model, they would be surrounded by a fossil, neutral hydrogen-rich (HI-rich) PN shell (Walker, 1985; Gillett et al., 1986; Lawson et al., 1990a; Clayton et al., 1999, 2011a).

Three stars (Sakurai's Object, V605 Aquilae, and FG Sagittae) have been observed to undergo FF outbursts that transformed them from hot evolved stars into cool giants with spectroscopic properties similar to RCB stars (Clayton & De Marco, 1997; Gonzalez et al., 1998; Asplund et al., 1998, 1999, 2000; Clayton et al., 2006). These FF stars are all surrounded by active PNe. However, cooler RCB central stars are no longer able to provide the needed ionizing radiation so the atoms in the shell have recombined. The velocity of the fossil PN shell would be similar to its velocity while it was hot and ionized, $\sim 20 - 30$ km s^{-1}. In the DD scenario, the stars may have had PN phases but they would have occurred so long ago, $\sim10^9$ years ago, that no structure resembling a fossil envelope would remain when the two WDs finally merge to form an RCB star.

However, the shell could be material lost during the merger event, itself. This would have happen much more recently, $\lesssim10^4$ years ago, and would imply these structures are much less massive than previously estimated (Gillett et al., 1986; Clayton et al., 2011a). A third explanation for the observed shells is that they could have

formed during the RCB phase. RCB stars are thought to produce dust at a rate of 10^{-7} to 10^{-6} $M_{\odot}$ yr^{-1} (Clayton, 2012). Clayton et al. (2013a) have found that newly forming clouds are propelled away from the central star at speeds up to 400 km s^{-1}. This also could result in the observed envelopes on a timescale of about 10^4 years.

1.3 Goals

The origins of this CSM material as well as the progenitors of the central RCB stars still remain shrouded in mystery. We are now in an era where high spatial resolution and high sensitivity far-IR (FIR), sub-millimeter (sub-mm), and even radio observations exist of RCB stars in order to study their cold CSM material. For example, infrared spectroscopy of RCB stars has been possible thanks to the Infrared Space Observatory (ISO) and the *Spitzer* Space Telescope, which has permitted the extraction of the characteristics of the IR emitting dust shell around RCB stars (Lambert et al., 2001; García-Hernández et al., 2011a,b, 2013). However, these prior works lacked information in the FIR and sub-mm to appropriately study the older, colder dust far from the central stars.

The primary goal of my thesis is to determine the nature of these shells. I have also used this newly acquired information in order to improve our knowledge of the evolutionary status of the RCB stars. This was accomplished with a twofold approach:

- Determining the mass, size, and morphology of the diffuse material surrounding a sample of RCB stars
- Examining the H I abundance of the R CrB envelope

The RCB stars included in my sample are: MV Sagittarii (MV Sgr), R Coronae Borealis (R CrB), RY Sagittarii (RY Sgr), SU Tauri (SU Tau), UW Centauri (UW Cen), V854 Centuari (V854 Cen), and V Coronae Australis (V CrA). I have constructed multi–wavelength datasets ranging from the ultraviolet (UV) to sub-mm to accomplish the first method. These observations provide unprecedented wavelength coverage for both the central stars and their CSM. The majority of the properties of the dust shells will come from analysis of the spectral energy distribution (SEDs) of these stars. Archival observations with the largest single aperture radio telescope in the world were used for studying the H I abundance.

I have combined the information learned from my thesis work to better understand the evolutionary history of RCB stars. In the subsequent chapters I will fully describe the observations, data reduction techniques, analysis, and results of my sample of RCB stars. We are entering the exciting era of all-sky surveys, which will culminate in the LSST. It is expected to discover as many as 100,000 new transient objects a night. A theoretical understanding of transient events such as WD mergers and final helium shell flashes will be very important in an era when these types of objects are being discovered on a regular basis. The study of RCB stars gives us the opportunity to learn more about the potential products of mergers and final flashes.

2. Observations and Analysis

2.1 Observations

This thesis consists of multiwavelength observations ranging from the ultraviolet (UV) to the radio. The radio observations are used only for determining the H I abundance of the R CrB dust shell. The remaining observations are used for generating maximum light spectral energy distributions (SEDs). The facilities/instruments or catalogs that were used to acquire these observations will be described in the following subsections. Observations for R CrB and V605 Aql were obtained from Clayton et al. (2011a) and Clayton et al. (2013b), respectively. Stellar properties for my sample of RCB stars are presented in Table 2.1. These properties include, beginning with column 2: Galactic longtitude (l) and latitude (b); maximum apparent V–band magnitude ($[m_V]_{max}$) (Clayton, 2012); calculated (see Chapter 4) distance (D) in kiloparsecs (kpc) and luminosity (L) in solar luminosities ($L_\odot$); and effective temperature (T_{eff}) in Kelvin (K) (Asplund et al., 1998, 2000). The last column denotes what new FIR and/or sub-mm data are being presented in my thesis. The coding is defined as *Spitzer*/MIPS (M), *Herschel*/PACS (P), and *Herschel*/SPIRE (S). Figures 2.1–2.4 show the light curves from the American Association of Variable Star Observers (AAVSO) of my sample RCB stars with the epochs of the various observations that are included in my SED analysis marked.

Table 2.1: Stellar Properties and New Observations of Sample RCB Stars

Star	l (°)	b (°)	$[m_V]_{max}$	D (kpc)	L ($L_\odot$)	T_{eff} (K)	Observations
MV Sgr	13.40	−7.93	12.0	11.5	5200	16000	M
R CrB	45.05	50.98	5.8	1.40	9150	6750	P
RY Sgr	4.43	−19.44	6.5	1.50	8900	7250	M,P,S
SU Tau	188.86	−4.42	9.5	3.30	10450	6500	M,P,S
UW Cen	301.74	8.32	9.6	3.50	7320	7500	M,P
V854 Cen	323.77	19.10	7.0	2.28	11760	6750	M
V CrA	357.66	−15.65	9.4	5.50	6550	6250	M,P,S

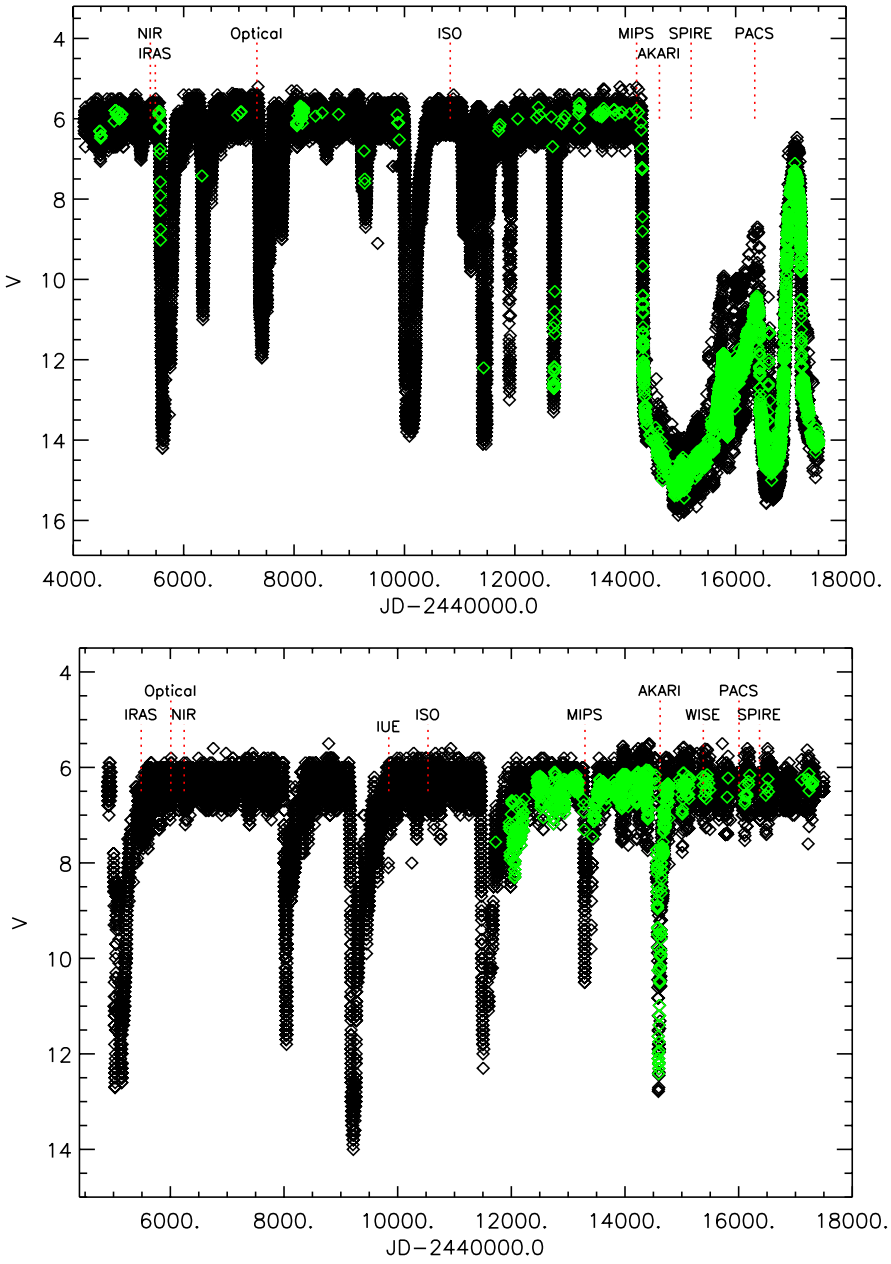

Figure 2.1: AAVSO observations of R CrB (top) and RY Sgr (bottom) since November 1979 and October 1981, respectively. Black diamonds are visual observations and green diamonds are Johnson V observations. The dates of the observations that went into my SED analysis are marked by the red,dashed vertical lines.

2.1.1 Ultraviolet Data

Many of the RCB stars were observed with the *International Ultraviolet Explorer* (IUE). The IUE was a Ritchey–Chretien design with a 0.45–m primary mirror. The satellite contained two spectrographs, which operated at "short" (1150–2000 Angstroms) and "long" (1850–3300) wavelengths. The spectrographs operated with either a small

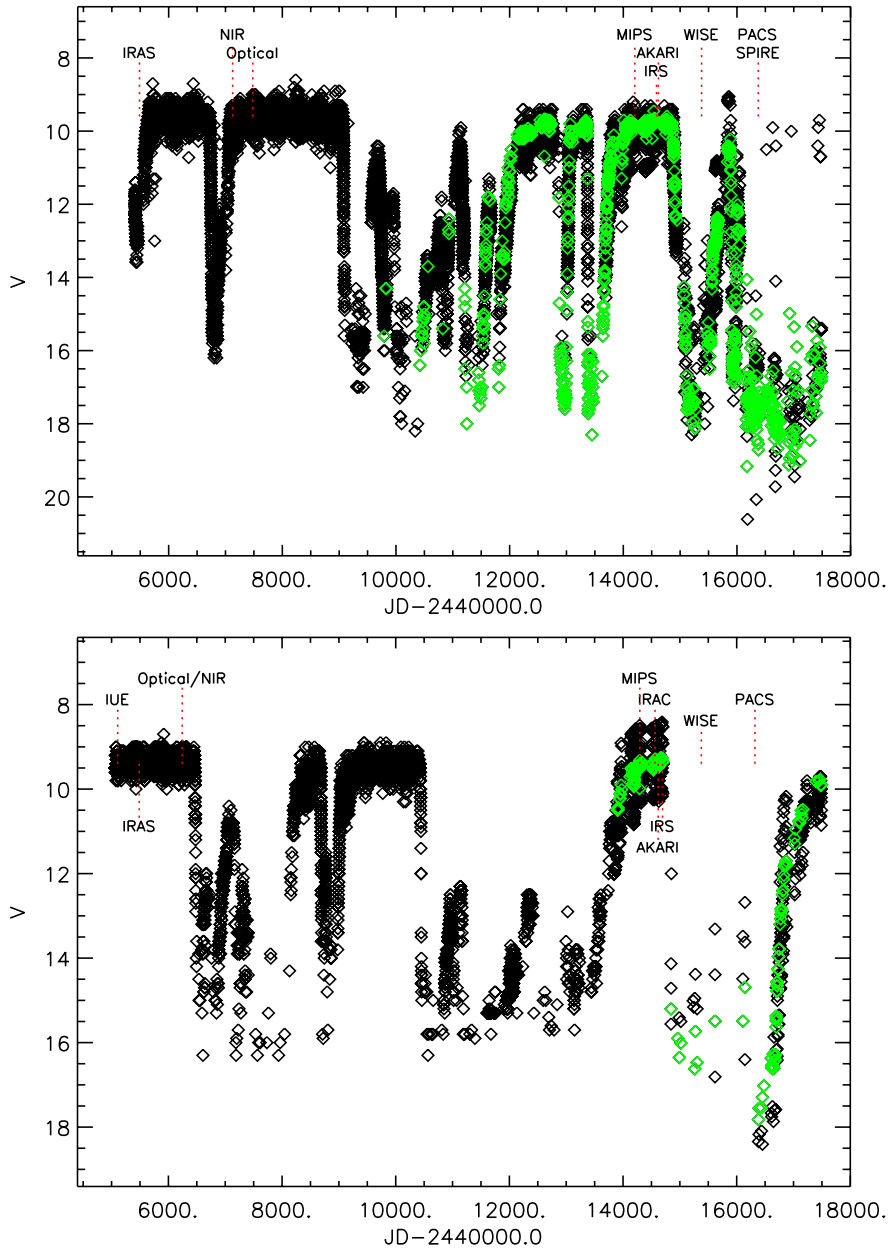

Figure 2.2: AAVSO observations of SU Tau (top) and UW Cen (bottom) since March 1983 and April 1982, respectively. Black diamonds are visual observations and green diamonds are Johnson V observations. The dates of the observations that went into my SED analysis are marked by the red,dashed vertical lines.

($\sim 3''$) circular or large ($10'' \times 20''$) slot aperture. Each spectrograph also had two cameras: a prime and a redundant. Both cameras were operational for the long wavelength channel, while only the prime camera worked for short wavelength observations.

Archival IUE data from the long wavelength spectrograph in large aperture mode of MV Sgr, UW Cen, RY Sgr, and V854 Cen were retrieved from the Barbara A.

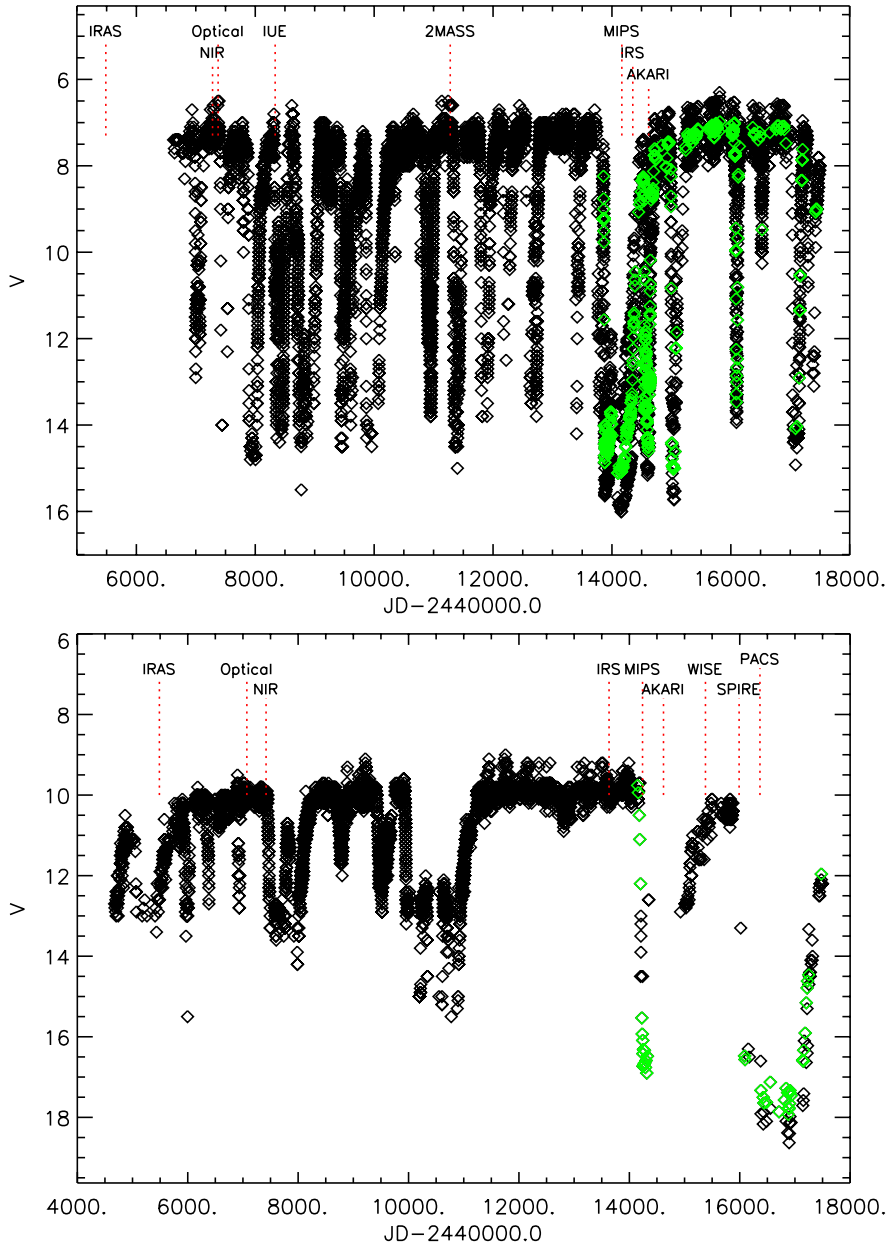

Figure 2.3: AAVSO observations of V854 Cen (top) and V CrA (bottom) since July 1986 and November 1979, respectively. Black diamonds are visual observations and green diamonds are Johnson V observations. The dates of the observations that went into my SED analysis are marked by the red,dashed vertical lines.

Mikulski Archive for Space Telescopes (MAST). The V854 Cen observation, LWP19951, was originally a part of the IUE program "RCMBW" (PI Barbara A. Whitney) and has been previously published in papers by Clayton et al. (1992b) and Lawson et al. (1999). RY Sgr, LWP30613, came from the IUE program "HERAH" (PI Albert V. Holm) and appeared in Holm (1999). The IUE observation of MV Sgr (LWR09008) came from Angelo Cassatella's program, AC414. The spectrum was included in a

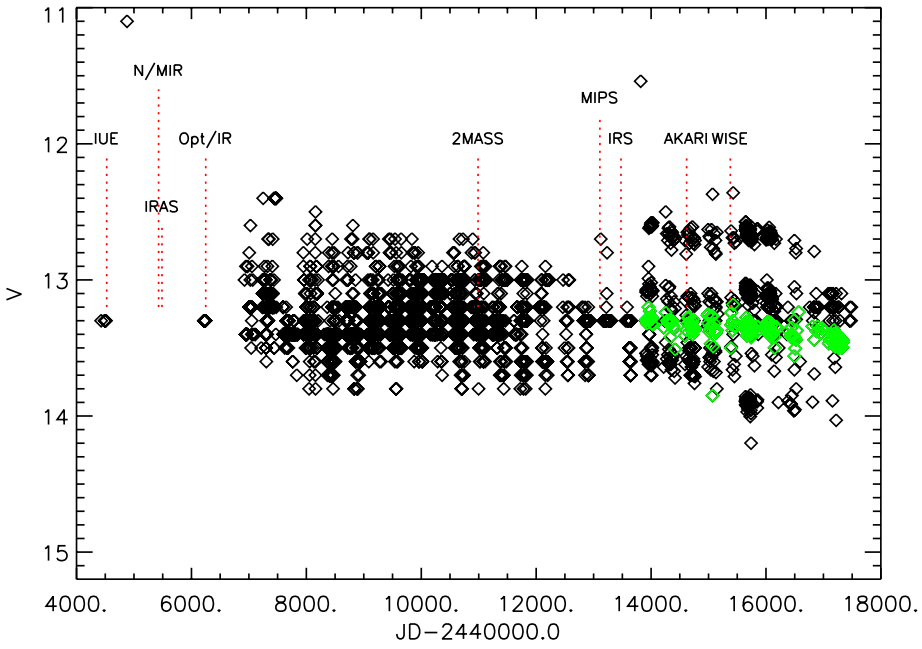

Figure 2.4: AAVSO observations of MV Sgr since October 1980. Black diamonds are visual observations and green diamonds are Johnson V observations. The time that the observations that went into my SED analysis are marked by the red,dashed vertical lines.

publication by Jeffery (1995). Finally the observation for UW Cen, LWR 13260, originated in a program by Aneurin Evans (EC228). This spectrum has not appeared in any refereed publications.

2.1.2 Optical Monitoring

RCB stars have been observed at all states between maximum and minimum light. Extensive ground-based monitoring in the optical was performed by multiple groups during the last century. Maximum light observations of SU Tau and V CrA were taken from Lawson et al. (1990a). They observed from the Mount John University Observatory (MJUO) located in New Zealand with either 0.6–m or 1.0–m telescopes and photomultiplier tubes. SU Tau was imaged in $BVR_{\rm C}I_{\rm C}$ photometric filters, while V CrA only in UBV. RY Sgr was observed near maximum light by Menzies & Feast (1997) with the South African Astronomical Observatory (SAAO) 0.5–m and 1.0–m telescopes in Sutherland, South Africa. Menzies & Feast provide coverage $UBVR_{\rm C}I_{\rm C}$ filters. Observations for MV Sgr and UW Cen at maximum light were retrieved from Goldsmith et al. (1990). Goldsmith et al. used the SAAO 0.5–m telescope with the Peoples photometer and $UBVR_{\rm C}I_{\rm C}$ filters. Maximum–light observations of V854 Cen were taken from Lawson & Cottrell (1989). The observations were taken at MJUO with the 0.6–m telescope with $UBVR_{\rm C}I_{\rm C}$ filters. HD 173409, the only Hydrogen–deficient (HdC) star and used as a comparison star (see Section 4.8.3), observations come from the SAAO 0.5–m telescope in Sutherland in from a $UBVR_{\rm C}I_{\rm C}$ monitoring

campaign by Marang et al. (1990).

2.1.3 Near Infrared Monitoring

Ground-based monitoring campaigns in the near Infrared (NIR) have been conducted at a similar level to the optical. These observations are usually done with the $JHKLM$ from the Johnson photometric system (Johnson, 1966). JH observations are primarily of the stellar photosphere, so they follow the fluctuations between maximum and minimum light that is the trademark of the RCB class. LM track the warm dust that has recently formed around an RCB star. Even if the dust is not in the line of sight.

NIR photometry for UW Cen also comes from Goldsmith et al. (1990), who provided MN observations of MV Sgr. These observations were taken simultaneously with their optical campaign described in the previous section. They also relied on an 0.75–m telescope located at the SAAO site. $JHKLMN$ observations from Kilkenny & Whittet (1984) were used for MV Sgr as well. Long term NIR monitoring of HD 173409, RY Sgr, SU Tau, V854 Cen, and V CrA were reported by Feast et al. (1997). They observed from the same SAAO 0.75–m telescope as Goldsmith et al.

2.1.4 Two Micron All Sky Survey

Additionally, the Two Micron All Sky Survey (2MASS) was a ground–based program to observe the entire sky in the NIR regime (Skrutskie et al., 2006). The survey ran from 1997 June to 2001 February. It observed effectively the entire celestial sphere in the $JHK_{\rm S}$, which correspond to central wavelengths of 1.25, 1.6, and 2.16 μm, respectively (Skrutskie et al., 2006). Observations were carried out with two 1.3–m telescopes; one located on Mt. Hopkins in Arizona and the other at Cerro Tololo Inter-American Observatory in Chile (Skrutskie et al., 2006). The photosphere of RCB stars still dominate at these wavelengths with the signature of very hot dust being able to be detected in $K_{\rm S}$. If an RCB star happened to be at maximum light while observed by 2MASS then the photometry from the 2MASS Point Source Catalog (Cutri et al., 2003), which contains 471 million unique sources, was retrieved. This applied to only two RCB stars in my sample, MV Sgr and V854 Cen, as well as the HdC star, HD 173409.

2.1.5 Infrared Space Observatory

The Infrared Space Observatory (ISO) was a joint European Space Agency (ESA), Japanese Aerospace Exploration Agency (JAXA), and NASA mission launched November 17, 1995. One of its instruments, the Short Wave Spectrometer (SWS Leech et al., 2003), provided spectroscopy between 2.4 and 45 μm. Calibrated SWS spectra of RY Sgr and R CrB (Sloan et al., 2003) were retrieved from an ISO SWS science archive hosted by Gregory C. Sloan[1].

[1]http://isc.astro.cornell.edu/ sloan/library/swsatlas/aot1.html

2.1.6 Spitzer Space Telescope

Spitzer Space Telescope (*Spitzer*, Werner et al., 2004) observations of RCB stars were acquired with all three instruments on board the satellite. These instruments are the Infrared Array Camera (IRAC, Fazio et al., 2004), the Infrared Spectrograph (IRS, Houck et al., 2004) and the Multiband Imaging Photometer for *Spitzer* (MIPS, Werner et al., 2004). IRAC was the NIR imager on *Spitzer* and provided simultaneous observations at 3.6, 4.5, 5.8, and 8.0 μm (central wavelengths). Only UW Cen was observed with IRAC (PI A. Evans, ID 40061).

IRS provided wavelength coverage in the range 5.3 to 38 μm with both low (R $\sim$ 90) and high (R $\sim$ 600) resolution (Houck et al. 2004). Archival IRS observations of RCB stars at both resolutions (PI D. Lambert, ID 50212) were previously published by García-Hernández et al. (2011b). Low resolution IRS observations were retrieved from the Cornell Atlas of *Spitzer*/IRS Sources (CASSIS, Lebouteiller et al., 2011), which provides a standard reduction of all the sources observed with the IRS. This was performed using the Spectroscopy Modeling Analysis and Reduction Tool (SMART, Higdon et al., 2004; Lebouteiller et al., 2010).

MIPS was the FIR imager on *Spitzer* and observed at (central) wavelengths of 24, 70, and 160 μm. Archival MIPS observations of RCB stars come from two programs, PIs G. Clayton (ID 30029) and A. Evans (ID 3362). The raw data were processed using the MIPS DAT package (Gordon et al., 2005), which performs standard reductions for IR array detectors as well as MIPS specific routines. The output images were then calibrated according to the methods established by Engelbracht et al. (2007), Gordon et al. (2007), and Stansberry et al. (2007) for the 24, 70, and 160 μm bands, respectively.

2.1.7 Wide-field Infrared Survey Explorer

The Wide-Field Infrared Survey Explorer (WISE, Wright et al., 2010) was a NASA medium-class explorer mission that was launched on December 14, 2009. Its mission was to survey the entire sky over 10 months at 3.4, 4.5, 12, and 22 μm with a 0.4–m primary. Two catalogs of WISE sources were released in 2012 (WISE All-Sky, Cutri et al., 2012) and 2013 (ALLWISE, Cutri, 2014), which encompass over 500 million and 700 million objects, respectively. The differences between the catalogs are detailed in Cutri (2014). I have adopted the ALLWISE photometry for my SED analysis and this photometry can be found in the individual tables for my sample stars in Chapter 4. The WISE observations of R CrB and V854 Cen are saturated, which makes the published photometry in both catalogs unreliable and not useable.

2.1.8 AKARI

AKARI was a JAXA satellite launched February 21, 2006 with 0.6–m primary mirror (Murakami et al., 2007). It was operated in two modes: an all-sky survey, similar to WISE, and a pointed mode for specific targets. It had two instruments: the Infrared Camera (IRC, Onaka et al., 2007) and the Far Infrared Surveyor (FIS, Kawada et al., 2007). The IRC contained three individual cameras observing at central wavelengths

of 3.6, 9, and 18 μm. The FIS had two detectors arrays that enabled both wide and narrow band FIR imaging. The central wavelengths of the narrow band imaging were 65 and 160 μm, while for wide band imaging it was 90 and 140 μm.

Two all-sky catalogs were released by the AKARI team. They are a MIR/IRC catalog (Ishihara et al., 2010), which published photometry at 9 and/or 18 μm for $\sim$870,000 individual sources, and FIR/FIS catalog (Yamamura et al., 2009) in one of the four FIS bands for $\sim$430,000 sources. AKARI photometry, in at least one of the six bands, was published for all of the RCB stars in this thesis.

2.1.9 Infrared Astronomical Satellite

The Infrared Astronomical Satellite (IRAS, Neugebauer et al., 1984) was the first space-based observatory to survey the entire sky in the IR. It operated in the MIR and FIR at central wavelengths of 12, 25, 60, and 100 μm. Two catalogs of IRAS photometry have been published and updated since the end of the mission. They are the IRAS Faint Source Catalog (FSC, Moshir & et al., 1990) and the Point Source Catalog (PSC, Helou & Walker, 1988). Both catalogs provide photometry in at least one of the four IRAS bands for a total of $\sim$300,000 individual sources. All of the RCB stars in my sample have IRAS observations in at least one of the four bands.

2.1.10 Herschel Space Observatory

The *Herschel* Space Observatory (*Herschel*, Pilbratt et al., 2010) has allowed for improved space-based resolution in both the FIR and sub-mm to detect and map cold dust surrounding stars. My sample of RCB stars was observed with *Herschel* in a guest observer campaign led by PI G. Clayton. Observations were conducted with both the Photodetector Array Camera and Spectrometer (PACS) at 70, 100, and 160 μm (Poglitsch et al., 2010) and the Spectral and Photometric Imaging REceiver (SPIRE) at 250, 350, and 500 μm (Griffin et al., 2010).

The IDL routine *Scanamorphos* (version 21.0, Roussel, 2013) was used for generating all of the final PACS and SPIRE maps for analysis. The map making process begins by downloading the raw satellite telemetry (Level 0 products) from the *Herschel* Science Archive (HSA). These products are then converted to physical units (Level 1 products), such as temperatures or voltages, with the *Herschel* Interactive Processing Environment (HIPE, version 12). HIPE is both a GUI and command line based software written in Jython (Java+Python). It is at these Level 1 products where the typical HIPE pipeline is interrupted (further processing with HIPE all the way to image products is possible) to generate FITS binary files that *Scanamorphos* can read and interact with. PACS maps are generated in the units of Jy pixel^{-1} with $1\farcs0$, $1\farcs4$, and $2\farcs0$ pixels at 70, 100, and 160 μm, respectively. SPIRE maps are generated in the units of Jy beam^{-1} and are then converted into Jy pixel^{-1} through a multiplicative constant derived from the individual SPIRE beams for each wavelength band. The maps have pixel sizes of $6\farcs0$, $10\farcs0$, and $14\farcs0$ at 250, 350, and 500 μm, respectively.

2.1.11 Radio

Radio observations containing the region around R CrB have been obtained from the first data release (DR1[2]) of the Galactic Arecibo L-band Feed Array H I (GALFA-HI) Survey (Peek et al., 2011). The GALFA-HI survey provides both high resolution ($4'$) and high sensitivity (typical rms $\sim$ 80 mK) due to their 305-m aperture and the installation of the Arecibo L-band Feed Array (ALFA) (Peek et al., 2011). Fully reduced "narrow" and "wide" band data cubes were retrieved from the survey. The former provided 0.18 km s^{-1} resolution in the local standard of rest (LSR) in the range $v_{LSR} = \pm 190$ km s^{-1}, while the latter provided 0.74 km s^{-1} resolution in the range $v_{LSR} = \pm 750$ km s^{-1}. A full description of the data acquisition, which includes both drift and basketweave scanning, and reductions for the GALFA-HI survey are presented by Peek et al. (2011) (see their Sections 3 and 4, respectively).

2.2 Spectral Energy Distribution Modeling

In order to understand what these observations contain, I needed to model the RCB star surrounded by its diffuse CSM. This was done by modeling the spectral energy distribution (SED) for the star + dust envelope.

2.2.1 Photometry

Photometry was done on the *Spitzer* and *Herschel* images in order to generate SEDs for the stars in my sample. There are two primary techniques for performing photometry on astronomical images: "aperture" and "point–spread function" (PSF) photometry. Aperture photometry is the simpler of the two methods. It involves defining a aperture (typically a circle) that encloses as much of the source for which flux information is desired. Next, the sky background needs to be subtracted. This "sky–annulus" is used to determine the average local background count per pixel, which is then subtracted from each pixel in the source aperture. Finally, the total of all the pixels within the originally defined aperture is calculated, which gives the brightness of the source. An example of a source with an aperture and sky–annulus is displayed in Figure 2.5.

A point–spread function (PSF) is the shape of any point source as "seen" by a telescope and instrument. Traditionally, PSFs are made from isolated bright point sources from the image(s) photometry is going to be performed on. This allows for a better characterization of how individual stars appear in a given astronomical image. Fortunately, the individual instrument teams for both the *Spitzer* and *Herschel* telescopes have spent a significant amount of time working to understand the shape of their PSFs. These PSFs are then provided freely to the community. The *Spitzer*/MIPS, *Herschel*/PACS, and *Herschel*/SPIRE PSFs are displayed in Figures 2.6 through 2.8, respectively.

PSF photometry works in theory much like aperture photometry in that the goal is to measure all of the flux of a particular source. Instead of defining an aperture and

[2]https://purcell.ssl.berkeley.edu/

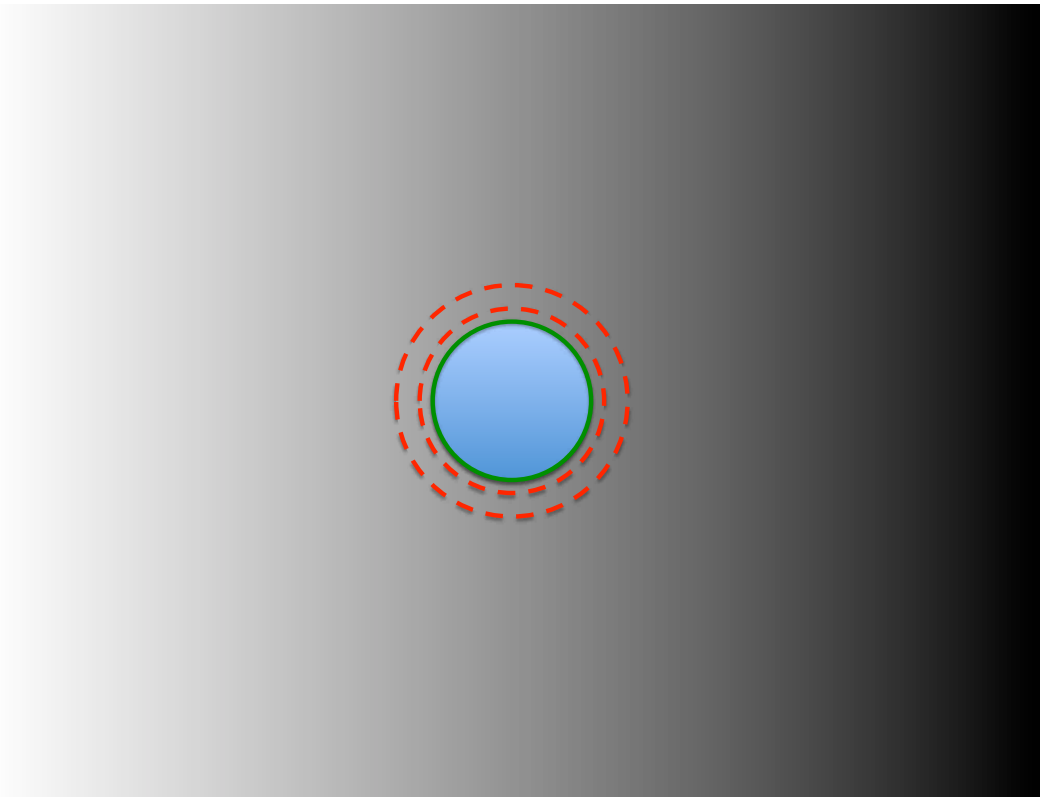

Figure 2.5: A cartoon representing aperture photometry of a point source (blue circle) with background (gray–to–black gradient). The green ring represents the aperture chosen to encircle all of the flux from the source, and the dashed red lines represent the sky–annulus.

sky annulus, the profile for any source is fit directly against the given PSF. This is why PSF photometry is going to do much better than aperture photometry in crowded regions where individual sources often become blended and in cases with complex backgrounds, which is when a sky annulus will not capture the true background. This is primarily caused by background galaxies becoming increasingly brighter in the FIR and sub-mm. See Chapter 4 for *Spitzer* and *Herschel* observations of individual stars where the background point sources are all distant galaxies. A limitation of PSF photometry is when the sources of interest are themselves extended, which is the case for many of the stars in my sample as their CSM is what is actually being observed at these wavelengths. Thus, PSF photometry of my sources served more as the occasional sanity check on the results of any aperture photometry, or to remove background galaxies from an image in order to better highlight diffuse nebulosity.

There are many different programs that have been written to perform automated aperture and PSF photometry. I chose to use the automated aperture routine Source Extractor (SExtractor, Bertin & Arnouts, 1996) because of prior experience with the

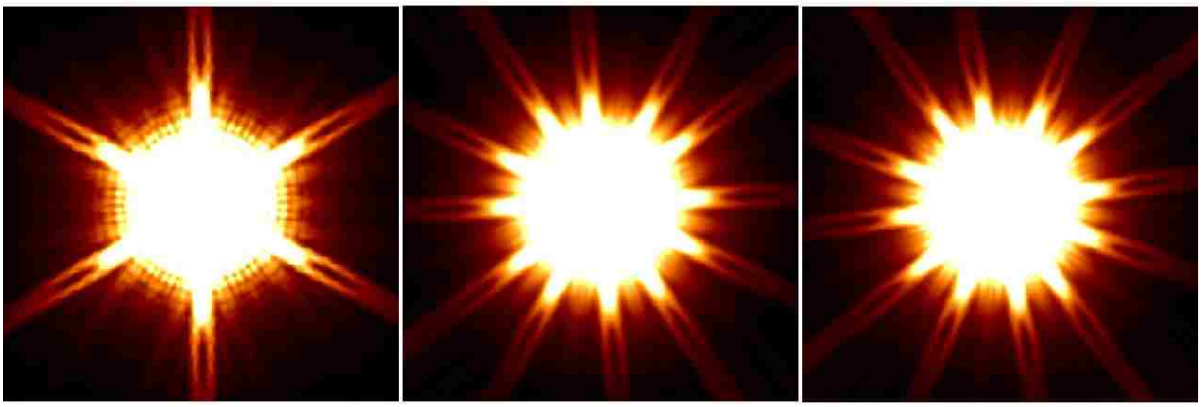

Figure 2.6: A 3-panel mosaic showing, from left to right, the *Spitzer*/MIPS 24, 70, and 160 μm PSFs, respectively. The images are presented on a linear scale to display their full dynamic range.

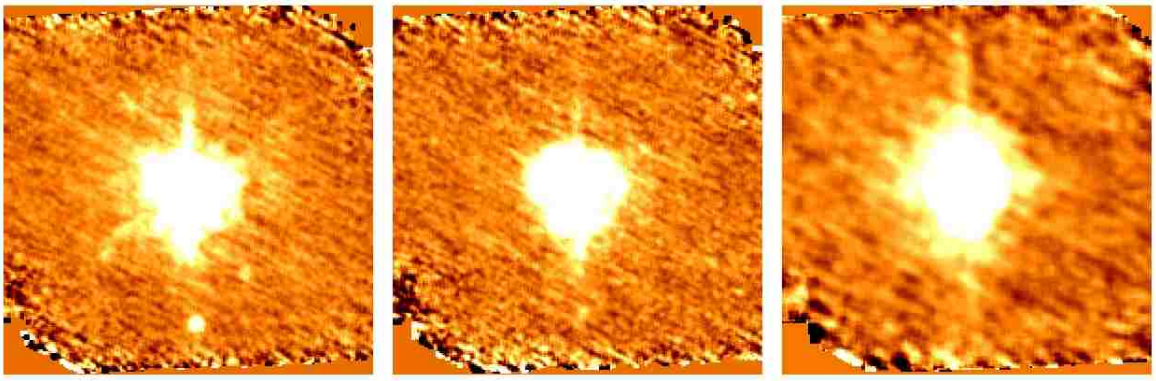

Figure 2.7: A 3-panel mosaic showing, from left to right, the *Herschel*/PACS 70, 100, and 160 μm PSFs, respectively. The images are presented on a linear scale to display their full dynamic range.

software (Montiel et al., 2015). The power of SExtractor is that there are many tunable parameters that allow the user to maximize the program to perform photometry on their desired objects, whether they be point source or extended. SExtractor also provides robust post–run ancillary products such as residual, background, object, and aperture images in addition to performing aperture photometry on any given input images. These diagnostics were used to judge the success of any run. Further, I chose to use the Interactive Data Language (IDL) routine StarFinder (Diolaiti et al., 2000a,b), which performs PSF photometry, also based on prior experience (Montiel et al., 2015). StarFinder, similar to SExtractor, provides a suite of post–run images for the purposes of diagnostics. In particular, the point source subtracted image is of great use for investigating the presence of any faint nebulosity. SExtractor was used for all the photometry except for the *Spitzer*/MIPS observations of V CrA, which are

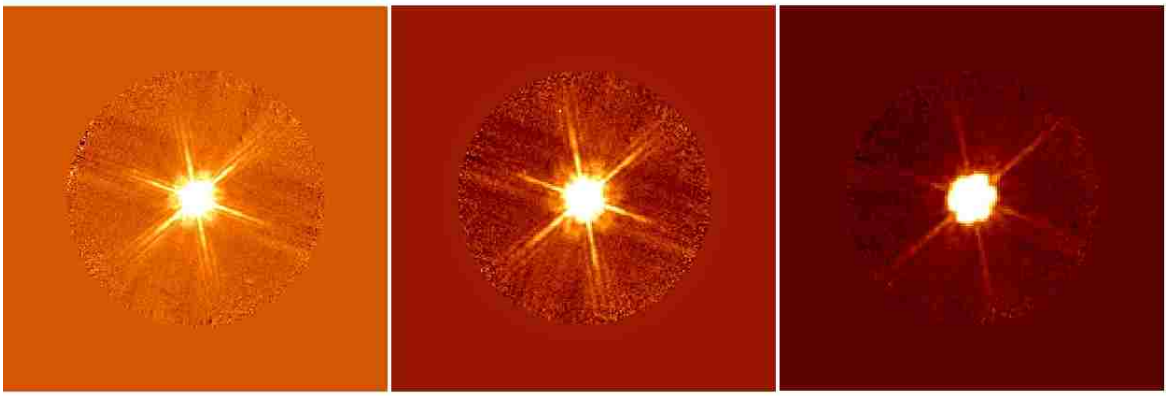

Figure 2.8: A 3-panel mosaic showing, from left to right, the *Herschel*/SPIRE 250, 350, and 500 μm PSFs, respectively. The images are presented on a linear scale to display their full dynamic range.

from StarFinder.

2.2.2 MOCASSIN

I performed Monte Carlo radiative transfer (MCRT) modeling on the SEDs for the stars in my thesis to better constrain the morphology and physical parameters of the dust surrounding these objects. MCRT relies on tracking the paths of photons as they propagate through a predefined, discrete dust grid. As the photon propagates through the grid, a probability is calculated at each step in order to determine the next "random" step. In the case of an interaction between a photon and dust grain, a second probability is calculated to determine if the photon is going to be absorbed and re–emitted, or scattered.

I used the fully 3D MOnte CArlo SimulationS of Ionized Nebulae (MOCASSIN) code. MOCASSIN is a MCRT modeling code (Ercolano et al., 2003, 2005, 2008). The code is written in Fortran 90 and is able to be run with parallel processing, through message passage interface (MPI) in order to speed up the modeling. I compiled MOCASSIN with Intel's "ifort" compiler, because it decreases the run time per model over free compilers such as gfortran. I also used Open MPI for the MPI implementation. MOCASSIN is a fully self–consistent 3D Cartesian dust RT code (Ercolano et al., 2005), which built on the previous version (Ercolano et al., 2003) and introduced the version 2.0 series. The code is run by first defining a series of user inputs, such as: number of dimensions, grid size, dust density, composition, and distribution. This reveals the robustness of the code as any arbitrary geometry and viewing angle can be modeled. Any interactions, whether absorption or scattering, between photons and dust grains are governed by Mie scattering theory (Ercolano et al., 2005). MOCASSIN is able to return temperature, mass, opacity, and composition of the dust shells. The SED modeling was performed with the latest version of MOCASSIN: 2.02.70.

For my sample, I choose to model these systems as a central point source sur-

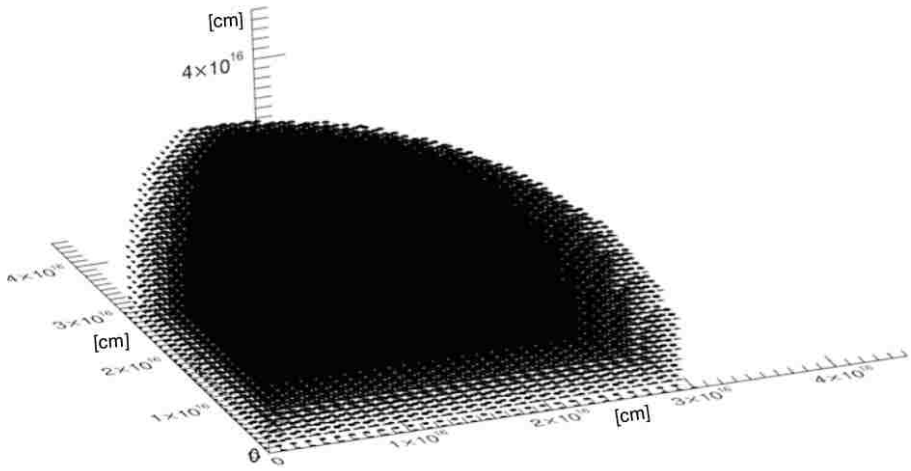

Figure 2.9: An IDL representation of the MOCASSIN dust grid representing the R CrB inner shell. This is how the shell appears when spherical symmetry is accounted for. Only one octant is modeled with the radiating source placed in the corner.

rounded by a gas–free dust shell. These shells are further assumed to be "smooth", which means that there are no inhomogeneities ("clumps"), with the dust density profile falling by r^{-2} from the inner radius (R_{in}) to the outer radius (R_{out}). I was able to take advantage of the axial symmetry (see Figure 2.9) to model only one–eighth of my envelope rather than a full envelope (see Figure 2.10). This choice resulted in not only a decreased run time per model, but also allowed an effectively higher resolution shell (in grid space) to be modeled. MOCASSIN, by default, places the origin/photon source at the middle of the user defined grid, which means that a $30 \times 30 \times 30$ cells runs only ± 15 in all directions. Thus, by modeling an octant, the origin, (0,0,0), and "star" are placed on the corner of the grid space. Next, the grid is defined moving outward from 0 to +30 in all three Cartesian directions.

The composition of the dust grains was determined by prior analysis of the spectra of RCB stars. The spectra were examined, in wavelengths ranging from the UV to the IR, for any features that would reveal the grain composition (Hecht et al., 1984; Clayton et al., 2011b; García-Hernández et al., 2011b, 2013). These previous studies all found that the composition of the dust is consistent with being amorphous Carbon (amC) grains. This is due to the extinction curve peaking between 2400 and 2500 Å (Hecht et al., 1984) and the featureless nature of the spectra in the optical and IR (García-Hernández et al., 2011b). Thus, my MCRT models were performed with 100% amC grains. The grain size, a, distribution was motivated by the findings of

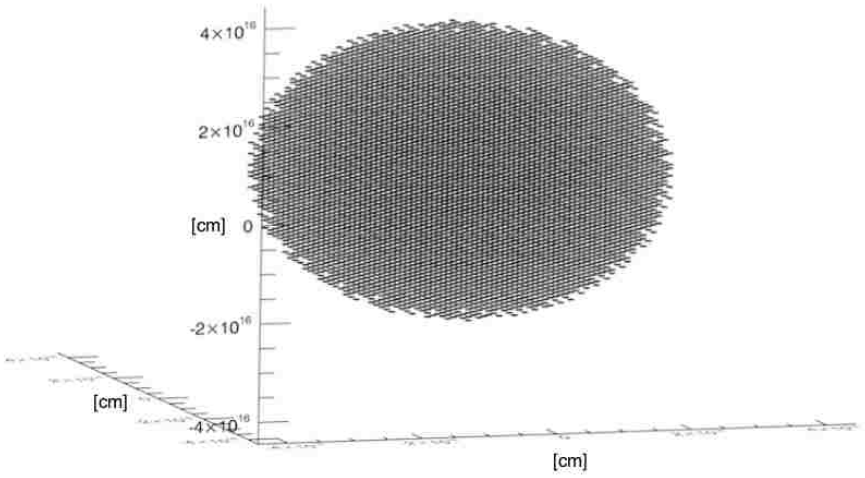

Figure 2.10: An IDL representation of the MOCASSIN dust grid representing the R CrB inner shell. This is how the shell would have appeared without taking advantage of the spherical symmetry.

Hecht et al. (1984), who used IUE observations of R CrB and RY Sgr to find that dust grain sizes appeared consistent with a distribution between 5–60 nm (0.005 to 0.06 μm). An MRN–like (Mathis et al., 1977) power law distribution, $a^{-3.5}$, was selected for determining the bin spacing and abundances.

The number of photons (N_{phot}) to include in my MOCASSIN modeling was motivated by needing to find the minimum number that would provide a balance between the best resolution at all wavelengths of interest and the run time per model. MOCASSIN uses the input source temperature and luminosity to determine the initial energy distribution of the photons before they diffuse outward through the grid. This means that changing the total number of photons will directly affect the total number of higher energy photons that will be absorbed, emitted, and re-absorbed multiple times throughout an individual run. An N_{phot} of 5.0×10^7 photons was found through trial and error to provide model coverage out to 500 μm while taking a reasonable amount of time (15 – 30 minutes) per run. Lower values of ($N_{phot} < 10^7$) lacked the necessary resolution in the FIR and sub-mm regime. Higher values ($N_{phot} > 10^8$) take longer than 1 hour per run, which is too inefficient for fine tuning the other parameters that control shell properties.

Detailed discussion of the modeling of individual stars can be found in Chapter 4.

3. What is the Shell Around R Coronae Borealis?[1]

3.1 Origin of the R CrB Dust Shell

3.1.1 The R CrB Dust Shell

The foreground extinction toward R CrB is quite small, E(B–V)$\sim$0.035 mag, since it lies at high Galactic latitude ($b^{II} = +51^{\circ}$) (Schlegel et al., 1998; Schlafly & Finkbeiner, 2011). At maximum light, R CrB is V=5.8 mag and B–V =0.6 mag (Lawson et al., 1990b). Based on the absolute magnitude/effective temperature relationship found for the Large Magellanic Cloud RCB stars, the absolute magnitude of R CrB is estimated to be M_V=–5 mag (Alcock et al., 2001; Tisserand et al., 2009). For the analysis in this work, we thus adopt a distance to R CrB of 1.4 kpc. The large extended far–IR shell, with a radius of $\sim 10'$, surrounding R CrB was discovered with *IRAS* and then studied further with the *Spitzer* and *Herschel* telescopes (Gillett et al., 1986; Clayton et al., 2011a; García-Hernández et al., 2011b, 2013). At the assumed distance of R CrB, the radius of the shell corresponds to 4 pc. Prior Monte Carlo radiative transfer (MCRT) modeling of the R CrB shell suggests that it contains 10^{-2} $M_{\odot}$ of dust (Clayton et al., 2011a).

3.1.2 A Planetary Nebula Shell?

The PNe around the FF stars, V605 Aql, Sakurai's Object, and FG Sge are still ionized. The shell around R CrB is not. There is a small subclass of RCB stars that are much hotter (T_{eff}= 15,000–20,000 K) than the typical RCB stars and are surrounded by PNe (Pollacco et al., 1991; De Marco et al., 2002). They are not hot enough at present to ionize their surrounding PNe, but the nebulae have not had time to recombine. The shells around the cooler RCB stars could be old PNe that have recombined. There are some strong similarities between the morphology

[1]This chapter previously appeared in the *The Astronomical Journal* under the same title as Montiel et al. (2015, AJ, 150, 14). The introduction has been omitted due to the overlap with the information presented in Chapter 1 of my thesis. The description of the radio observations that appeared as Section 2 of the paper can also be found Section 2.1.10 of my thesis. In addition to my advisor, I was aided in this particular project by Dr. Dominic C. Marcello, my advisor's postdoctoral researcher, and Dr. Felix J. Lockman of the National Radio Astronomy Observatory. Dr. Lockman guided me in how to analyze radio data. Dr. Marcello contributed the findings from his simulations of white dwarf mergers. It is reprinted by permission of the American Astronomical Society (see Appendix A).

of the shells of UW Cen and R CrB, and some PNe such as the Eskimo Nebula. Cometary features seen in PNe such as the Eskimo are similar to those seen in these two RCB stars (Clayton et al., 2011a). The recombination time depends on the electron densities of the shells and could range from hundreds to thousands of years. If n_e=200 cm^{-3}, as assumed for Sakurai's Object, the recombination time for R CrB's PN shell would be ∼380 yr (Pollacco, 1999). The amount of time that R CrB has been an RCB star is unknown but it is one of the first variable stars to be discovered (Pigott & Englefield, 1797), so we know that it has been in its RCB star phase for at least 200 yr.

The PNe seen around the FF stars, Sakurai's Object and V605 Aql, are thought to be $\sim 2 \times 10^4$ yr old, both with expansion velocities of ∼30 km s^{-1} and radii of 0.35 pc for V605 Aql and 0.7 pc for Sakurai's Object (Pollacco et al., 1992; Guerrero & Manchado, 1996; Pollacco, 1999). A FF star may not be old enough to produce a PN shell of the size seen around R CrB as it only takes a few years for the star to reach its RCB–like phase after the FF (Herwig, 2001).

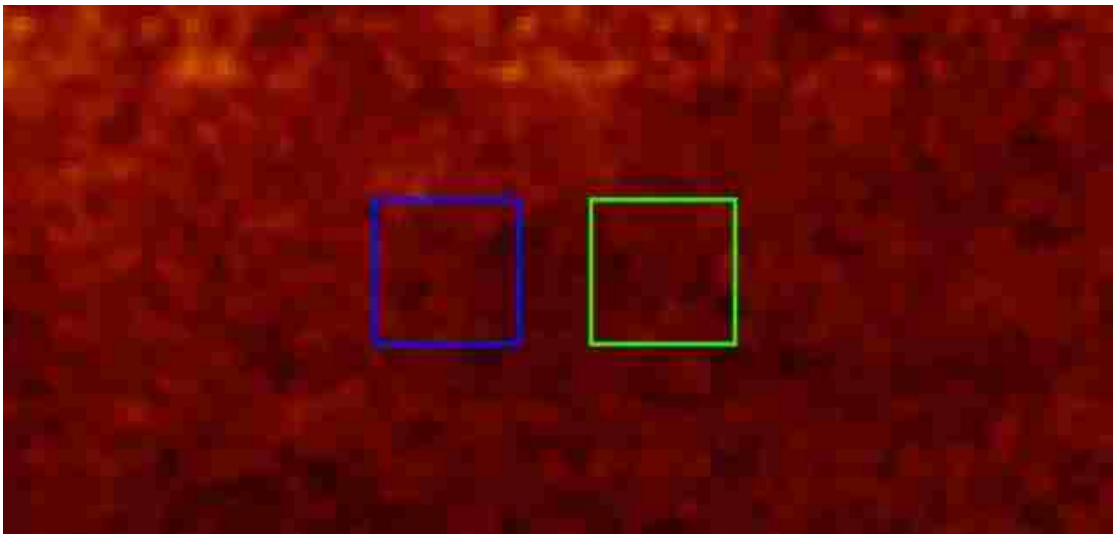

Figure 3.1: GALFA-HI field (2.25° × 1.15°) showing the location of the R CrB shell (green square) and the area used for background subtraction (blue square). The squares are 20′ × 20′.

If the R CrB shell is, in fact, a PN shell then it should be hydrogen rich (Gillett et al., 1986). No pointed 21-cm measurements of any RCB circumstellar shells have been published previously. A visual inspection of the narrow band GALFA-HI data cube through velocity space was performed to see if there were any obvious H I features. The search focused on ±30 km s^{-1} of the v_{LSR} of R CrB ∼ 37 km s^{-1} (The barycentric radial velocity of R CrB ∼ 22.3 km s^{-1} (Lawson & Cottrell, 1997)). No obvious structure was discerned.

Next, a 20′×20′ square region, roughly the size of the dust shell, centered on R CrB was selected, as well as a background region of the same size as shown in Figure 3.1. The background reference spectrum were subtracted from the spectrum toward the

R CrB shell to determine if there is any H I emission that might be associated with the shell. While fluctuations in the background H I limit the comparison in many directions, one reference position, shown in Figure 3.1, has an H I spectrum that is identical within the noise to the spectrum averaged over the shell at the relevant velocities, and the difference spectrum (Figure 3.2) can be used to limit the H I mass of R CrB.

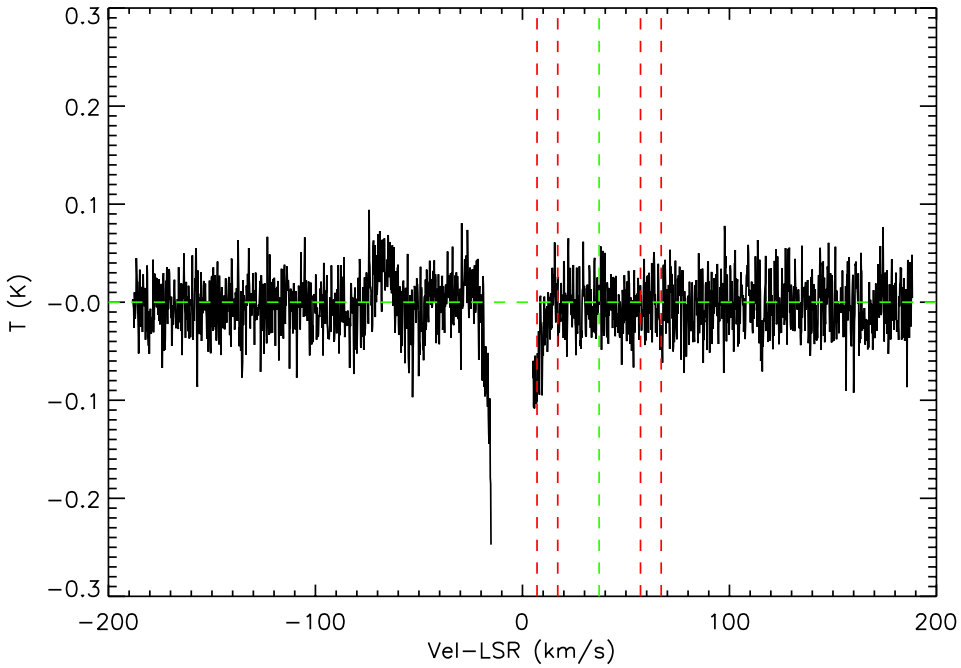

Figure 3.2: A background–subtracted temperature vs. radial velocity plot for area around R CrB. The vertical green dashed line is the position of R CrB in radial velocity and the two vertical red lines mark ±20 and ±30 km s^{-1} from the velocity of R CrB. The feature at -70 km s^{-1} is part of a large elongated emission not associated with the R CrB shell. The horizontal green dashed line is at temperature = 0°.

The rms noise ($\sigma_{\rm rms}$) in the 0.18 km s^{-1} channels of Figure 3.2 is 27 mK. Over a ±30 km s^{-1} interval, this gives a 3σ limit on column density, N_H (atoms cm^{-2}) in the R CrB shell of 4.9×10^{17}. This was derived using $N_H = 3.0 \times 1.82 \times 10^{18} \times \sigma_{\rm rms} \times {\rm dv} \times \sqrt{n_{\rm ch}}$, where dv is the 21cm channel spacing (0.18 km s^{-1}) and $n_{\rm ch}$ is the number of channels (∼330) over the relevant velocity range (Dickey & Lockman, 1990). The mass of any neutral hydrogen, in solar masses, is then less than $M_H = 6.9 \times 10^{-28} \times N_H \times D^2 \times \Omega$, where D is the distance in pc (1400 pc), and Ω is the solid angle of the region in $arcmin^2$. With our upper limit on N_H, the corresponding 3σ limit on H I in the R CrB shell is 0.3 $M_\odot$. Assuming that the mass loss is contained in a shell that has been moving outward at 30 km s^{-1}, the PN shell would take ∼10^5 yr to expand to r= 4 pc. A shell of that age would almost certainly have had time to recombine and become neutral.

The number density of H in this shell would be low, similar to that seen in the diffuse interstellar medium. Therefore, the fraction of H_2 will be near zero, and all of the H will be atomic and neutral (Rachford et al., 2009). The 21-cm measurements presented here put a strong upper limit on the H mass in the R CrB shell. A study of the gas and dust masses in the shell of the PN, NGC 6781, gives a total shell mass of 0.86 $M_\odot$ and a dust mass of 4×10^{-3} $M_\odot$ and therefore a gas-to-dust ratio of about 215 (Ueta et al., 2014). Assuming a gas-to-dust ratio of 200, the amount of dust in the R CrB shell would be $\lesssim 10^{-3}$ $M_\odot$.

3.1.3 Mass Loss from a White Dwarf Merger?

We have simulated the RCB DD formation scenario by running three binary WD merger models using our fully three-dimensional adaptive mesh refinement (AMR) code (Marcello et al. 2016, in prep). This code evolves density, total energy, and angular, vertical, and radial momenta on a rotating Cartesian mesh. Once started, the model is driven into closer contact by artificially removing angular momentum from the system at a rate of 1% per orbit for several orbits. Through AMR, we are able to run the models in large grids whose box dimensions are 20–30 times larger than the orbital separation. This allows for a more accurate determination of mass loss during the merger than on a smaller grid, where much of the material exiting the grid does not possess enough energy to escape. The initial conditions were created using the self-consistent field technique (SCF) to create a detached synchronously rotating binary WD in equilibrium just shy of becoming semi-detached (Hachisu, 1986; Even & Tohline, 2009). Each model run follows the merger of a CO- and a He-WD in a close binary orbit, and is primarily described by the mass ratio of the binary: q, which is defined as the mass of the donor ($M_{\rm Donor}$; the He-WD) divided by the mass of the accretor ($M_{\rm Accretor}$; the CO-WD). The q=0.8 and q=0.5 models have a hybrid CO/He accretor, which as described by Staff et al. (2012) is a WD with a CO core and a He envelope of about 0.1 $M_\odot$. The results, along with the initial conditions, of our simulations are summarized in Table 3.1.

In the models presented here between 0.9 and 3.3% of the initial mass escapes and is not expected to fall back onto the new merged star. Therefore, in the three models described in Table 3.1 the mass lost from the two WDs, which could form into a circumstellar shell around the new RCB star, is $\sim 10^{-2}$ $M_\odot$. The gas that has escape velocity is >95% He so a maximum of 5% of the gas could condense into dust. Assuming this and the average Galactic gas-to-dust ratio of 100 (Whittet, 2003), the amount of dust in such a shell would be $\sim 5 \times 10^{-6}$ $M_\odot$. A different gas-to-dust ratio was adopted, since in this scenario the envelope is not PN-like. The merger event itself only takes a few minutes after which there is a rapid expansion to supergiant size (Staff et al., 2012). Zhang et al. (2014) estimate that the new star will expand to ~200 $R_\odot$ in 500 yr. The estimated velocities of the gas escaping the grid in the simulations listed in Table 3.1 is 600–900 km s^{-1}. This gas would take $\sim 10^4$ yr to expand to the size of the R CrB shell. These velocities are the same order of magnitude as the winds measured in RCB stars in the He I λ10830 line (Clayton et al., 2013a). This analysis assumes that any PN/common envelope phases of the two stars in the binary

Table 3.1: Model Results

Parameter	Model 1	Model 2	Model 3
Mass Ratio (q)	0.51	0.70	0.80
Accretor Mass ($M_\odot$)	0.503	0.526	0.561
Donor Mass ($M_\odot$)	0.255	0.366	0.45
Total Mass ($M_\odot$)	0.758	0.892	1.011
% Mass Lost	2.3	0.90	3.3
Initial Period (s)	181	118	90.9
Final/Initial Period	9.9	2.9	6.9
Initial separation ($R_\odot$)	6.30×10^{-2}	5.00×10^{-2}	4.38×10^{-2}
Grid Box Dim. ($R_\odot$)	1.74	1	1.38
Orbits driven at 1%	2.5	4	2.5
dx ($R_\odot$)	5.66×10^{-4}	6.51×10^{-4}	4.49×10^{-4}
Init. Sep. in Cells	111	77	98

occurred long before the merger but this time period is not known.

Table 3.2: Shell Types

Type	v_{exp} (km s^{-1})	Time (yr)	Dust Mass ($M_\odot$)	Total Mass ($M_\odot$)
Planetary Nebula	30	10^5	$<10^{-3}$	<0.3
WD merger	600–900	10^4	5×10^{-6}	10^{-2}
RCB star	400	10^4	$>10^{-3}$	Unknown

3.1.4 RCB Phase Mass Loss?

It is thought that dust forms in puffs near the atmosphere of an RCB star (Clayton, 1996). We adopted the assumption that during a single dust formation event a puff forms at 2 $R_\star$ ($R_\star$=85 $R_\odot$) and subtends a fractional solid angle of 0.05, which results in the photosphere of the star being obscured and a dust mass of $\sim 10^{-8}$ $M_\odot$ (Clayton et al., 1992a, 2011a). Declines occur when a puff forms along the line of sight, but other puffs are likely forming around the star that do not cause declines. These puffs can be detected in the IR. Recent studies pertaining to IR variability of RCB stars has found that the covering factor can vary from RCB star to RCB star and find an average covering factor of 0.28±0.04 for R CrB (García-Hernández et al., 2011b; Rao & Lambert, 2015). Other studies find a higher covering factor (Hecht et al., 1984; Clayton et al., 1999). In addition, a correlation between pulsation phase and the timing of dust formation has been found in several RCB stars (Crause et al., 2007) and they typically show regular or semi-regular pulsation periods in the 40–100 d range (Lawson et al., 1990b). R CrB, itself, does not have one regular period but

has shown periods of 40 and 51 d (Fernie & Lawson, 1993). Therefore, if a dust puff forms somewhere around R CrB every 50 days then $\sim 10^{-7}$ $M_\odot$ of dust will form per year around the star.

There is strong evidence from observations at He I λ10830 that the dust, once formed, is accelerated quickly by radiation pressure from the star to $\sim$400 km s^{-1} (Clayton et al., 1992a, 2003, 2013a). The He gas is likely dragged outward by the dust. Therefore, dust produced during the RCB phase could fill the R CrB shell in only $\sim 10^4$ yr. In that time, R CrB will produce at least 10^{-3} $M_\odot$ of dust depending how many puffs form around the star. Considering the assumptions made here and those made in the radiative transfer modeling, this estimated dust mass is close to the 10^{-2} $M_\odot$ estimated by Clayton et al. (2011a). The mass of gas in an RCB shell is unknown. The gas will be primarily He with little or no H.

The observed far-IR shell around R CrB appears nearly spherical. The suggestion that the present day mass loss from R CrB is bipolar would not support this morphology (Kameswara Rao & Lambert, 1993). Further polarimetric or interferometric observations are needed to determine the morphology of the RCB-star dust mass loss (e.g., Clayton et al., 1997; Bright et al., 2011).

3.2 Chapter Summary

The estimated masses of the circumstellar shells in the FF/PN, WD merger (DD), and RCB scenarios are summarized in Table 3.2. If the shell is an old fossil PN in the FF scenario, then the gas should be H-rich. In the other two cases, it would be H-poor and dominated by He gas. The results of the 21-cm observations find no detectable H in the R CrB shell. The observations place an upper limit of $\sim$0.3 $M_\odot$ on the mass of the PN. The ionized masses observed for some PNe are in this range (e.g., Boffi & Stanghellini, 1994; van Hoof & van de Steene, 1999). The radius of R CrB shell is very large for a PN shell. The PN shells of the FF stars, V605 Aql and Sakurai's Object, are 0.35 and 0.7 pc, respectively. A 4 pc radius PN shell would take $\sim 10^5$ yr to fill at 30 km s^{-1}. The gas mass loss in a WD merger is $\sim 10^{-2}$ $M_\odot$. Since this gas is mostly He, little dust could form in such a shell.

The gas mass of the R CrB shell is not known, but the dust mass has been estimated to be as high as 10^{-2} $M_\odot$ (Clayton et al., 2011a). If it formed during the RCB phase then the shell would be filled with He gas, the mass of which cannot be measured so the gas-to-dust ratio is unknown. Based on the analyses above, we would expect only 10^{-3} – 10^{-6} $M_\odot$ of dust in the PN and WD merger mass loss scenarios. Thus the suggestion that the R CrB shell has formed from the dust forming during its present RCB phase seems most likely since it can form $\gtrsim 10^{-3}$ $M_\odot$ of dust. If true, this model implies that R CrB has been an RCB star for $\sim 10^4$ yr to have produced a 4 pc radius shell. More sensitive 21-cm observations of R CrB and other RCB star shells are needed to place more stringent constraints on their H masses.

4. The Circumstellar Shells of R Coronae Borealis Stars

This chapter contains an analysis of both new and archival observations of the sample stars in this thesis. The sources of these data are described in Chapter 2. A twofold approach was adopted for this investigation. The unpublished, archival *Spitzer* and *Herschel* images were examined by eye to identify morphological features that cannot be determined through traditional photometry methods. This technique is easily performed due to the small number of stars contained in my sample. Next, the results from aperture and/or PSF photometry (see Chapter 2) were used to fill in the FIR and sub-mm regime for the maximum–light SEDs of the stars in my sample. Building on the findings in the previous chapter for the R CrB envelope, the goal of these two methods is to achieve a better understanding of the CSM of RCB stars. This, by extension, allows for a more accurate picture of the mass loss history for these stars and clearer idea of the progenitors of the RCB stars.

4.1 MV Sgr

Variability in MV Sgr was first discovered by Woods (1928). It would be another 30 years until it was identified as being an RCB star (Hoffleit, 1958, 1959). Hoffleit (1959) also discussed the results of early spectra obtained by Herbig (1964), which confirmed the hydrogen–deficiency of MV Sgr. However, what was unexpected was that the effective temperature of MV Sgr was more similar to a star with a surface temperature of 20,000 K. This extreme temperature makes this star a member of the unique subset of "hot" RCB stars (of which only 4 are known total) (De Marco et al., 2002).

MV Sgr is inferred to have a planetary nebula-like shell that is currently still ionized (De Marco et al., 2002). This inference comes from the presence of Hα and forbidden emission lines in the MV Sgr spectrum. The other two Galactic hot RCB stars (DY Cen & V348 Sgr) are known to have ionized CSM (De Marco et al., 2002). If there is a PN associated with MV Sgr then the effective temperature of the star itself, $\sim$16,000 K, is too cool to provide the necessary photons to keep it ionized.

4.1.1 Image Inspection

MV Sgr was unfortunately not observed with either PACS or SPIRE on *Herschel*. This makes the *Spitzer*/MIPS observations the only instrument with which information

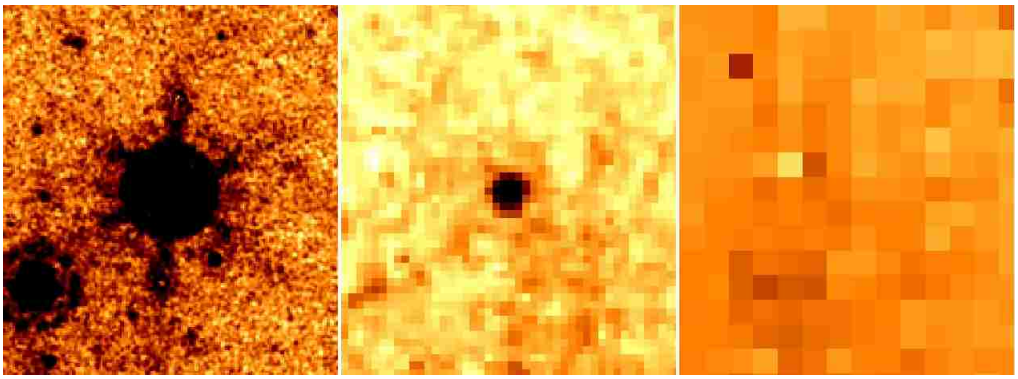

Figure 4.1: The *Spitzer*/MIPS view of MV Sgr. The panels are (left to right) 24, 70, and 160 μm, respectively, and the field–of–view is $3.6' \times 4.0'$. North is up and East is left.

from wavelengths longer than 100 μm can be learned. Postage stamp images from MIPS can be seen in Figure 4.1 and display from left to right the 24, 70, and 160 μm observations. The images are all oriented in the astronomical format of North–up and East–left and colors have been inverted to show positive flux as darker. MV Sgr appears as a point source, namely the MIPS PSF at 24 μm, which is because of the existence of warm dust around MV Sgr. While at 70 μm MV Sgr appears as a point source as well, which indicates cold dust further from the central source. Neither MV Sgr nor any CSM appears in the MIPS 160 μm observation.

4.1.2 Radiative Transfer Modeling

Archival photometry and spectroscopy were combined with new photometry from the *Spitzer*/MIPS observations to construct the SED for MV Sgr. See Table 4.1 for the input values. The maximum–light SED is presented in Figure 4.2 along with the best–fit MOCASSIN models. The SED in the UV/optical is fit well by a T_{eff} =16,000 K blackbody as determined by Drilling et al. (1984) and 2002AJ....123.3387D. The input luminosity for the MOCASSIN modeling was determined by assuming an absolute magnitude M_V=−3.0 for the hot RCB stars (Tisserand et al., 2009). This corresponded to a distance of 11.5 kpc and luminosity of ∼5,200 $L_\odot$.

Table 4.1: MV Sgr Photometry

Band	Flux (Jy)	σ (Jy)
U (0.365)	0.013	1.20e-04
B (0.433)	0.015	1.40e-04
V (0.550)	0.018	1.60e-04
$R_{\rm C}$ (0.640)	0.015	1.4e-04
$I_{\rm C}$ (0.790)	0.025	2.3e-04
2MASS/J (1.235)	0.060	0.001
J (1.25)	0.075	0.007
H (1.60)	0.130	0.012
2MASS/H (1.66)	0.117	0.003
2MASS/$K_{\rm S}$ (2.16)	0.188	0.004
K (2.20)	0.213	0.020
L (3.40)	0.344	0.032
WISE/3.4	0.180	0.004
WISE/4.6	0.199	0.004
M (4.80)	0.874	0.402
M (4.80)	0.551	Upper limit
AKARI/9	0.330	0.019
N (10.2)	0.814	0.150
N (10.2)	0.742	0.068
IRAS/12	0.597	0.130
WISE/12	0.409	0.006
AKARI/18	1.00	0.008
WISE/22	1.11	0.017
MIPS/24	1.00	0.004
IRAS/25	1.57	0.140
IRAS/60	0.777	0.078
AKARI/65	0.257	Upper Limit
MIPS/70	0.286	0.009
AKARI/90	0.496	0.103
IRAS/100	3.47	Upper Limit

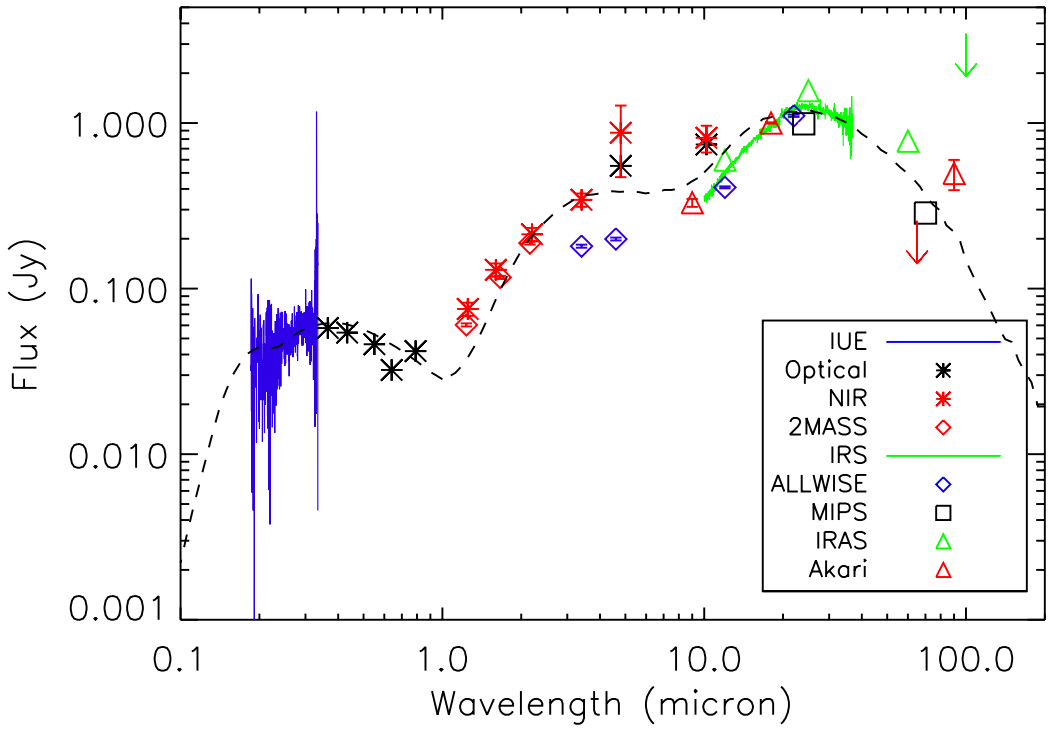

Figure 4.2: The maximum–light SED of MV Sgr. Blue line: IUE spectrum; black asterisks: $UBVR_{\rm C}I_{\rm C}MN$; red asterisks: $JHKLMN$; open red diamonds: 2MASS $JHK_{\rm S}$; open blue diamonds: WISE (3.4, 4.6, 12.0, 22.0 μm); green line: *Spitzer*/IRS spectrum; open black squares: *Spitzer*/MIPS (24 and 70 μm); open green triangles and arrow (3σ): IRAS (12, 25, 60, 100 μm); open red triangle and arrow (3σ): AKARI (60 and 100 μm). The sum of the best–fit MOCASSIN models for the central source, warm, and cold dust shells is represented by the dashed black line.

The effect of a strong IR excess can be seen after 1.0 μm as the SED continues to rise as wavelength increases. The IR component was best–fit by two concentric, smooth shells with density falling as r^{-2}. This modeling strategy is reinforced with a "by eye" examination of the SED where the presence of two separate components in the IR can be easily seen. The first peak is at $\sim$4.6 μm, and corresponds to an envelope beginning at 3.45×10^{14} cm and extending to 9.45×10^{15} cm. The dust mass is 7.59×10^{-8} $M_{\odot}$ while temperatures range from 1,000 K down to 200 K at the inner and outer radius, respectively. The second peak occurs at $\sim$ 25 μm with a best–fit envelope having an inner radius 3.25×10^{16} cm and outer radius 9.45×10^{17} cm. Dust temperatures in the shell range from 150 K to 50 K with a mass of 3.27×10^{-4} $M_{\odot}$.

The shape of the SED in the IR regime was also examined by García-Hernández et al. (2011b, 2013). García-Hernández et al. (2011b) found that the two blackbody curves have temperatures 1500 and $\sim$200 K, which agree with temperatures from my MCRT modeling. MV Sgr has been among the least active of RCB stars in terms of decline events. In all the years of monitoring this star there have only been 2 observed declines with the last significant decline recorded by Hoffleit (1959). In spite of this seemingly low level of activity, the dust mass in the outer envelope is about the same

with other RCB stars in this thesis. This is due the puff like nature of dust formation events. Declines only happen when the cloud condenses along our line of sight with the RCB star. There can be any number of puffs, at any time, forming around the central RCB star that we are not able to detect in the visible (García-Hernández et al., 2011b, 2013; Rao & Lambert, 2015). Thus, an appreciable envelope with a reservoir of cold dust can still be constructed even if a star remains at maximum light.

4.2 R CrB

R CrB is the eponymous member of the RCB class having been first discovered as variable in the late 18th Century (Pigott & Englefield, 1797). Keenan & Greenstein (1963) first identified the star as having Li via the 6707 Å feature. R CrB has also been found to be enriched with ^{19}F via lines at 6902.47 and 6834.26 Å (Pandey et al., 2008).

4.2.1 Image Inspection

Observations of R CrB in the FIR and sub-mm were previously inspected and discussed by Clayton et al. (2011a), which included both *Spitzer*/MIPS and *Herschel*/SPIRE. *Herschel*/PACS observations were taken after the paper was published and are presented here for the first time. Figure 4.3 contains the complete 9–panel postage stamp series of the MIPS, PACS, and SPIRE images of R CrB. The images have been rotated such that North–left and East–down and colors have been inverted to show positive flux as darker.

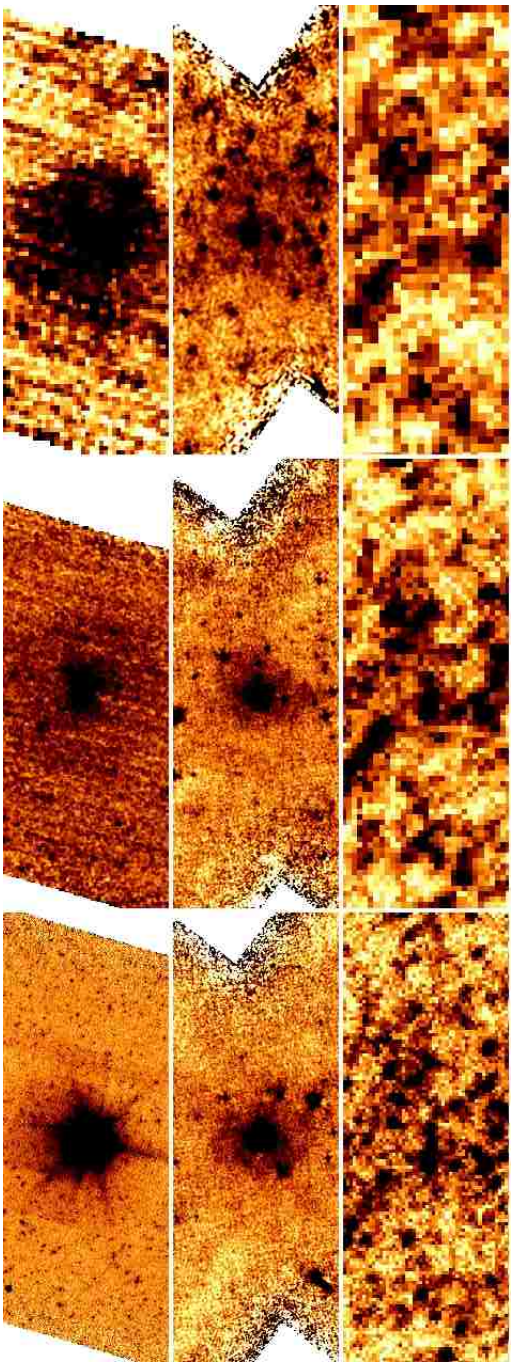

Figure 4.3: First row (beginning lower left corner):*Spitzer*/MIPS observations of R CrB 24, 70, 160 μm, respectively. The field–of–view shown for all three bands is $25' \times 10'$. Second row: *Herschel*/PACS observations of R CrB at 70, 100, and 160 μm, respectively. The field–of–view shown for all three bands is $12' \times 5'$. Third row: *Herschel*/SPIRE observations of R CrB at 250, 350, and 500 μm, respectively. The field–of–view shown for all three bands is $13.5' \times 5.0'$. North is left and East is down.

Previous discussions of R CrB's nebulosity point the spherical nature of its morphology (Gillett et al., 1986; Clayton et al., 2011a). These works had at their disposal the highest sensitivity and angular resolution FIR/sub-mm observations for their time. The diffuse structure seen prior at other wavelengths is also resolved at these wavelengths (as well as the background galaxy cluster). These observations reinforce the apparent spherical shape to the nebulosity.

4.2.2 Radiative Transfer Modeling

The maximum–light SED of R CrB was originally modeled and presented by Clayton et al. (2011a). New photometry from the *Herschel*/PACS observations of R CrB were added to the Clayton et al. (2011a) SED and remodeled using MOCASSIN. The SED is displayed in Figure 4.4 with the input photometry held in Table 4.2. The best–fit MOCASSIN model is represented by the dashed line. Parameters from Clayton et al. (2011a) were adopted for our own MCRT modeling. These include an effective temperature of 6,750 K and distance of 1.40 kpc, which results in a luminosity of 9,150 $L_{\odot}$.

Table 4.2: R CrB Photometry

Band	Flux (Jy)	σ (Jy)
U (0.365)	4.53	0.039
B (0.433)	11.60	0.107
V (0.550)	17.90	0.166
$R_{\rm C}$ (0.640)	20.50	0.190
$I_{\rm C}$ (0.790)	20.70	0.191
J (1.25)	17.70	0.165
H (1.60)	14.30	0.100
K (2.20)	14.30	0.133
L (3.40)	25.60	0.236
AKARI/9	53.00	2.440
IRAS/12	38.90	1.550
AKARI/18	21.50	0.029
IRAS/25	17.10	0.684
IRAS/60	3.94	0.315
MIPS/70	2.03	0.034
PACS/70	2.13	0.003
AKARI/90	1.49	0.114
IRAS/100	2.00	0.160
PACS/100	1.04	0.0023
MIPS/160	0.297	0.00936
PACS/160	0.335	0.00211
SPIRE/250	0.0781	0.01170
SPIRE/350	0.0340	0.00510
SPIRE/500	0.0125	0.00434

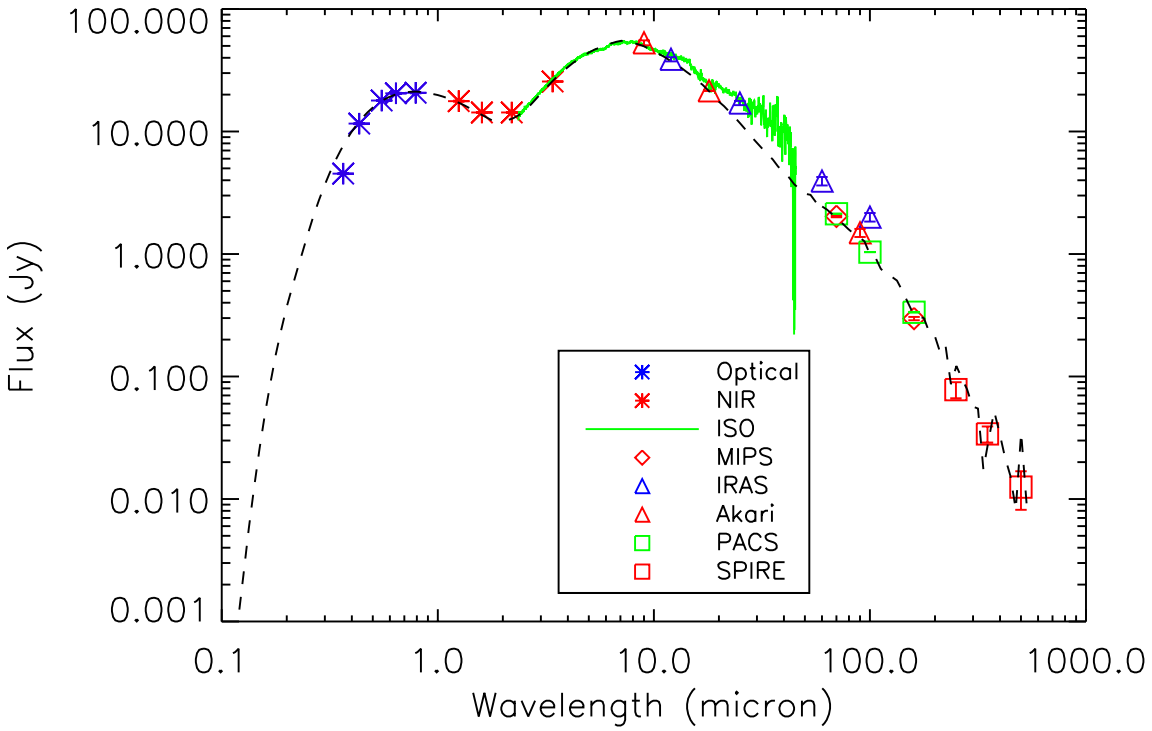

Figure 4.4: The maximum–light SED of R CrB. Blue asterisks: $UBVR_{\rm C}I_{\rm C}$; red asterisks: $JHKL$; green line: ISO spectrum; open red triangles: AKARI (9, 18, 90 μm); open red diamonds: *Spitzer*/MIPS (24 and 70 μm); open blue triangles: IRAS (12, 25, 60, 100 μm); open green squares: *Herschel*/PACS (70, 100, 160 μm); open red squares: *Herschel*/SPIRE (250, 350, 500 μm). The sum of the best–fit MOCASSIN models for the central source, warm, and cold dust shells is represented by the dashed black line.

The R CrB SED was best modeled using two concentric dust envelopes. The inner shell extends from 1.00×10^{15} cm to 3.00×10^{16} cm. The mass of this envelope was found to be 9.09×10^{-7} $M_{\odot}$ with dust temperatures ranging from 700 K down to 180 K. A second envelope was modeled to account for the presence of additional colder material that one envelope cannot entirely account for. This outer shell has an inner radius of 3.40×10^{17} cm and outer radius of 1.00×10^{19} cm. The dust mass contained in this envelope is 2.42×10^{-4} $M_{\odot}$ with temperatures ranging from 80 K to 20 K.

R CrB has been the most studied of any RCB star, so it comes as no surprise that its SED has also been extensively studied (Gillett et al., 1986; Rao & Nandy, 1986; Goldsmith et al., 1990; Young et al., 1993b,a; Nagendra & Leung, 1996; Walker et al., 1996; Lambert et al., 2001; García-Hernández et al., 2011b; Clayton et al., 2011a; Rao & Lambert, 2015). The decade long gap following Lambert et al. (2001) before any new works were published coincides with the launch of several space–based IR missions (i.e., *Spitzer*, *Herschel*, AKARI, WISE) that were able to provide additional wavelength coverage as well as overlap with IRAS.

I have compared my MOCASSIN results to those of García-Hernández et al. (2011b) and Clayton et al. (2011a). Rao & Lambert (2015) builds on the work

presented by García-Hernández et al. (2011b) and focuses more on tracking changes in the brightnesses of RCB stars in the 30 years of space–based MIR observations. A two component (star + single IR excess) blackbody fit was used by García-Hernández et al. (2011b) to describe the R CrB SED. They described the stellar component with a blackbody of $T_{star} = 6750$ K (derived from Asplund et al. 2000), and the IR excess with a blackbody that had a maximum dust temperature of 950 K, which was based off *Spitzer*/IRS spectrum between 10 and 20 μm (García-Hernández et al., 2011b).

Clayton et al. (2011a) presented the results of their full 3D (spherical polar grid) MCRT code. The code included non–isotropic scattering, polarization, and thermal emission from dust (Whitney et al., 2003b,a; Robitaille et al., 2006). The dust was assumed to be 100% amorphous carbon grains and followed an MRN size distribution (Mathis et al., 1977). The best–fit model found that the observed SED could be explained by the presence of a dusty disk surrounded by a larger envelope. The disk extended from 6.28×10^{14} cm to 2.24×10^{15} cm and had a dust mass of 3.5×10^{-6} $M_{\odot}$ (Clayton et al., 2011a). The shell had radii of 1.95×10^{18} cm and 1.32×10^{19} cm at the inner and outer boundaries, respectively (Clayton et al., 2011a). The dust mass of the Clayton et al. envelope was also found to be roughly two orders of magnitude higher ($\sim 2.0 \times 10^{-2}$ $M_{\odot}$). The discrepancy in our results for the mass of the larger envelope is most likely due to the non–uniqueness of RT modeling.

4.3 RY Sgr

RY Sgr was first suspected to be variable in 1893 while under observation by Colonel E. E. Markwick while he was stationed in Gibraltar (Pickering, 1896; Shears, 2011). Pickering (1896) also noted that the spectrum of the new variable was found to be peculiar after being discovered by Williamina Fleming. By the early 1950s, RY Sgr was known to be hydrogen–deficient and classified as an RCB star (Bidelman, 1953). Lambert & Rao (1994) found no evidence for Li overabundance in the spectrum of RY Sgr. The presence of ^{19}F was found in RY Sgr's atmosphere from absorption lines located at 6902 and 6834 Å (Pandey et al., 2008).

RCB stars, as a class, are known to show brightness fluctuations via pulsations in addition to their spectacular declines. RY Sgr was first discovered to be pulsating with 0.5 magnitude variations and a period of ∼39 days by (Campbell & Jacchia, 1946). An analysis of the long time light curve of RY Sgr revealed that its period appears to be decreasing over time (Kilkenny, 1982; Marraco & Milesi, 1982). This change has been attributed by Kilkenny and Marraco & Milesi as typical evolution of hydrogen–deficient stars or changes in the mass loss behavior of RY Sgr.

4.3.1 Image Inspection

Diffuse nebulosity surrounding RY Sgr was searched for in the unpublished, archival *Spitzer*/MIPS, *Herschel*/PACS, and *Herschel*/SPIRE observations. These observations provide the highest angular resolution and sensitivity for RY Sgr from 24 to 500 μm. A 9–panel mosaic containing these images are found in Figure 4.5. The frames displayed are from lower–left to top–right *Spitzer*/MIPS 24, 70, 160 μm,

Herschel/PACS 70, 100, and 160 μm, and *Herschel*/SPIRE 250, 350, 500 μm, respectively. They are all $3.2' \times 7.6'$, except for the *Spitzer*/MIPS 24 μm image which is $6.1' \times 15.5'$. The colors have also been reversed such that darker regions represent where there is more flux.

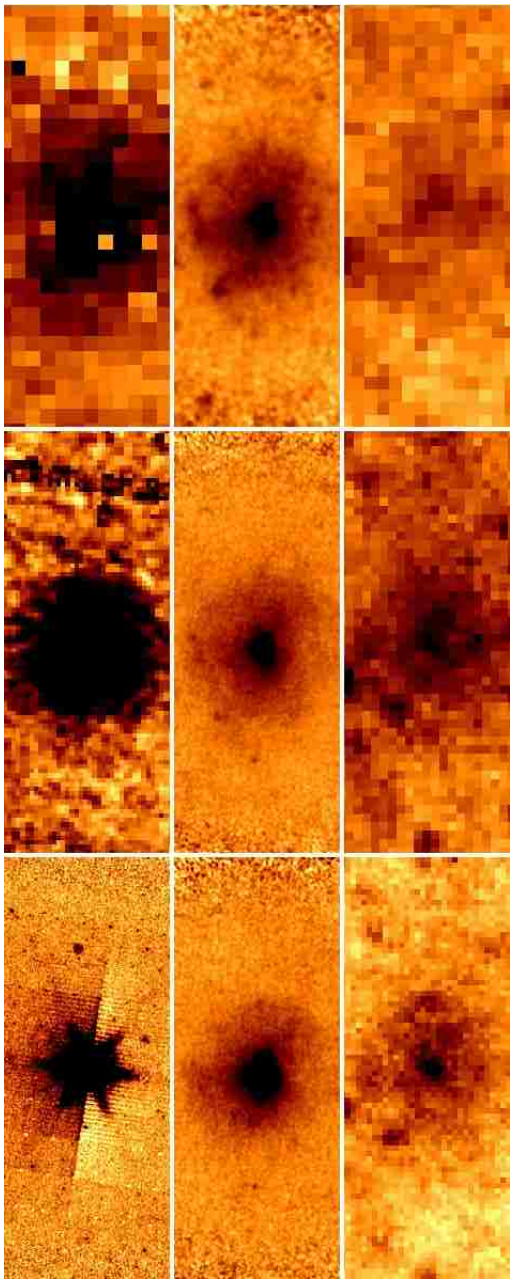

Figure 4.5: First row (beginning lower left corner): *Spitzer*/MIPS observations of RY Sgr 24, 70, 160 μm, respectively. Second row: *Herschel*/PACS observations of RY Sgr at 70, 100, and 160 μm, respectively. Third row: *Herschel*/SPIRE observations of RY Sgr at 250, 350, and 500 μm, respectively. The field–of–view in the *Spitzer*/MIPS 24 μm is $15.5' \times 6.1'$, while the remaining panels are all $7.6' \times 3.2'$. North is left and East is down.

RY Sgr at 24 μm is essentially the PSF for *Spitzer*/MIPS. RY Sgr begins to become more extended in the 70 and 160 μm observations, however the angular resolution at MIPS is not high enough to separate out the PSF from any diffuse nebulosity. *Herschel*/PACS was able to provide the necessary jump in angular resolution to resolve the diffuse nebulosity surrounding RY Sgr. The diffuse structure appears as spherical in shape. Yet, the density of the shell appears to be higher in the northern region when compared with the southern. This is reinforced with the *Herschel*/SPIRE observations at 250 and 350 μm where the angular resolution is still high enough. However, by 500 μm the resolution and sensitivity have degraded that only a rough determination of where the nebulosity lies can be made and nothing stronger.

4.3.2 Radiative Transfer Modeling

The available photometry and spectroscopy for RY Sgr (while at maximum–light) were combined to construct its SED, which can be seen in Figure 4.6. The dashed line represents the best–fit MCRT model from MOCASSIN. The photometry is found in Table 4.3. A blackbody with $T_{eff} = 7250$ K was adopted from atmosphere modeling by Asplund et al. (2000). A distance of 1.5 kpc was determined by assuming an absolute V–band magnitude of -5 (Tisserand et al., 2009). This results in an input luminosity of 8,900 $L_{\odot}$ for RY Sgr.

Table 4.3: RY Sgr Photometry

Band	Flux (Jy)	σ (Jy)
U (0.365)	4.31	0.040
B (0.433)	9.77	0.090
V (0.550)	13.3	0.122
$R_{\rm C}$ (0.640)	14.30	0.132
$I_{\rm C}$ (0.790)	14.10	0.130
J (1.25)	13.5	0.124
H (1.60)	15.2	0.140
K (2.20)	23.8	0.219
L (3.40)	54.0	0.497
WISE/3.4	18.9	2.72
WISE/4.6	46.2	8.20
AKARI/9	48.0	3.66
IRAS/12	77.2	5.40
WISE/12	36.2	0.966
AKARI/18	20.2	1.02
WISE/22	14.0	0.232
IRAS/25	26.2	1.048
IRAS/60	5.43	0.489
AKARI/65	3.50	0.104
MIPS/70	2.92	0.021
PACS/70	4.39	0.008
AKARI/90	2.61	0.139
IRAS/100	4.60	0.414
PACS/100	3.31	0.007
AKARI/140	2.08	Upper Limit
MIPS/160	1.34	0.030
AKARI/160	2.60	Upper Limit
PACS/160	1.79	0.005
SPIRE/250	0.766	0.010
SPIRE/350	0.324	0.007
SPIRE/500	0.126	0.006

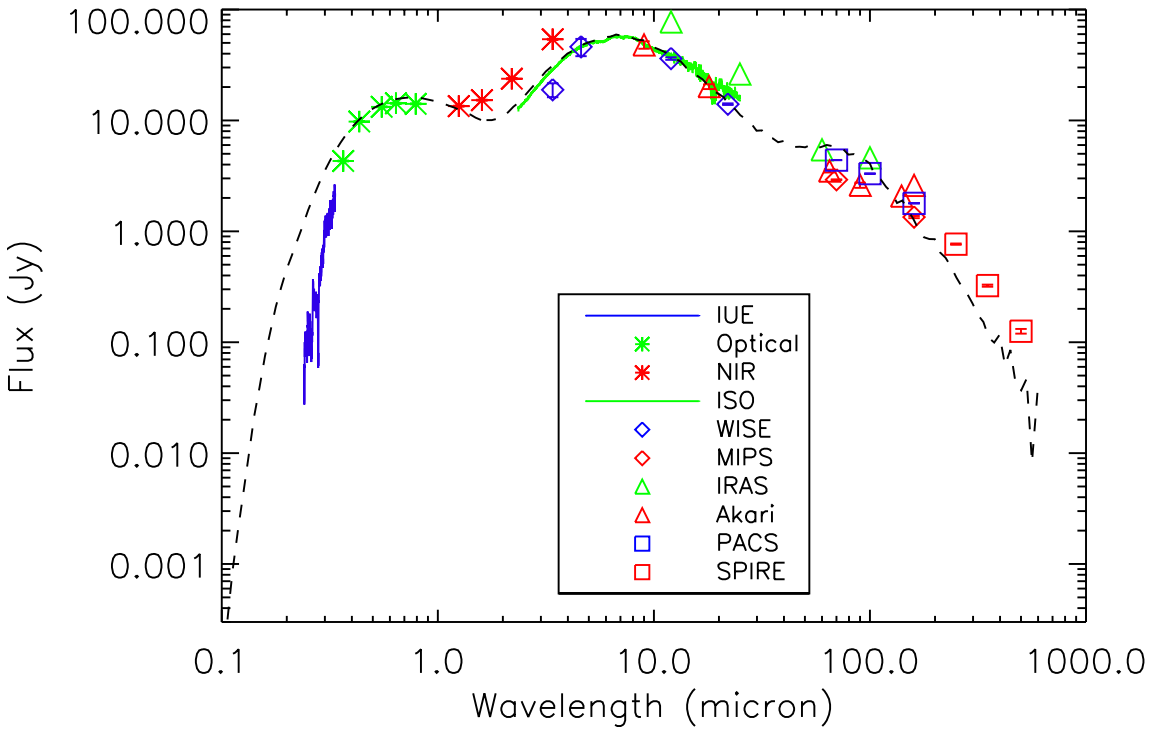

Figure 4.6: The maximum–light SED of RY Sgr. Blue line: IUE spectrum; green asterisks: $UBVR_{\rm C}I_{\rm C}$; red asterisks: $JHKL$; green line: ISO spectrum; open blue diamonds: WISE (3.4, 4.6, 12.0, 22.0 μm ; open red triangles: AKARI (9, 18, 90, 140, 160 μm); open red diamonds: *Spitzer*/MIPS (70 and 160 μm); open green triangles: IRAS (12, 25, 60, 100 μm); open blue squares: *Herschel*/PACS (70, 100, 160 μm); open red squares: *Herschel*/SPIRE (250, 350, 500 μm). The sum of the best–fit MOCASSIN models for the central source, warm, and cold dust shells is represented by the dashed black line.

The SED begins to be dominated by the RY Sgr CSM after 1.6 μm (H–band) due to contribution from warm dust close to the central star. A spherical envelope with inner radius at 8.62×10^{14} cm and outer radius at 5.00×10^{16} cm describes the SED between 1.6 and ∼25.0 μm. The dust mass of this envelope is 8.90×10^{-7} $M_{\odot}$ with temperatures ranging from ∼500 K down to ∼200 K. This wavelength region of the RY Sgr SED was also examined by García-Hernández et al. (2011b). The central star was represented by a blackbody of 7200 K. This is not a significant departure from the temperature used in this thesis, 7250 K, and supported by Asplund et al. (2000). The maximum temperature of the blackbody used to fit this dust component was found to be 675 K (García-Hernández et al., 2011b).

However, a second excess can be seen to arise as the photometry longer than 40 μm do not lie on the Rayleigh–Jeans tail of the first IR excess. This component was most likely missed by García-Hernández et al. (2011b), since they restricted themselves to observations shorter than 40 μm. A second envelope was modeled with an inner radius at 5.15×10^{17} cm and extending outward to 4.50×10^{18} cm. The dust mass of this envelope is 7.25×10^{-4} $M_{\odot}$ with temperatures ranging from ∼60 K down to ∼30

K. The dust mass in the modeled outer envelope is the second highest in dust mass.

4.4 SU Tau

Variability in SU Tau was first noted by Cannon & Pickering (1908) with a note that it could be an RCB star. This classification was strengthened further in a later *Harvard College Observatory Bulletin* (Barnard, 1916). SU Tau, like R CrB, has been found to be rich in Li and ^{19}F (Lambert & Rao, 1994; Pandey et al., 2008).

4.4.1 Image Inspection

Unpublished FIR and sub-mm observations of SU Tau exist from *Spitzer*/MIPS, *Herschel*/PACS, and *Herschel*/SPIRE. These observations are presented as a 9–panel postage image in Figure 4.7. The panels are from lower–left to top–right: *Spitzer*/MIPS 24, 70, 160 μm, *Herschel*/PACS 70, 100, and 160 μm, and *Herschel*/SPIRE 250, 350, 500 μm, respectively. The images are all oriented such that North–left and East–right and colors have been inverted to show positive flux as darker. The sensitivity with *Spitzer*/MIPS is more than enough to detect the presence of any dust surrounding SU Tau, however the angular resolution is not sufficient enough to separate nebulosity from the PSF. Further highlighting the need for improved angular resolution is how the galaxy that lies along line of sight of SU Tau, 2MFGC 4715 (Mitronova et al., 2004), is blended in the *Spitzer*/MIPS 70 μm PSF.

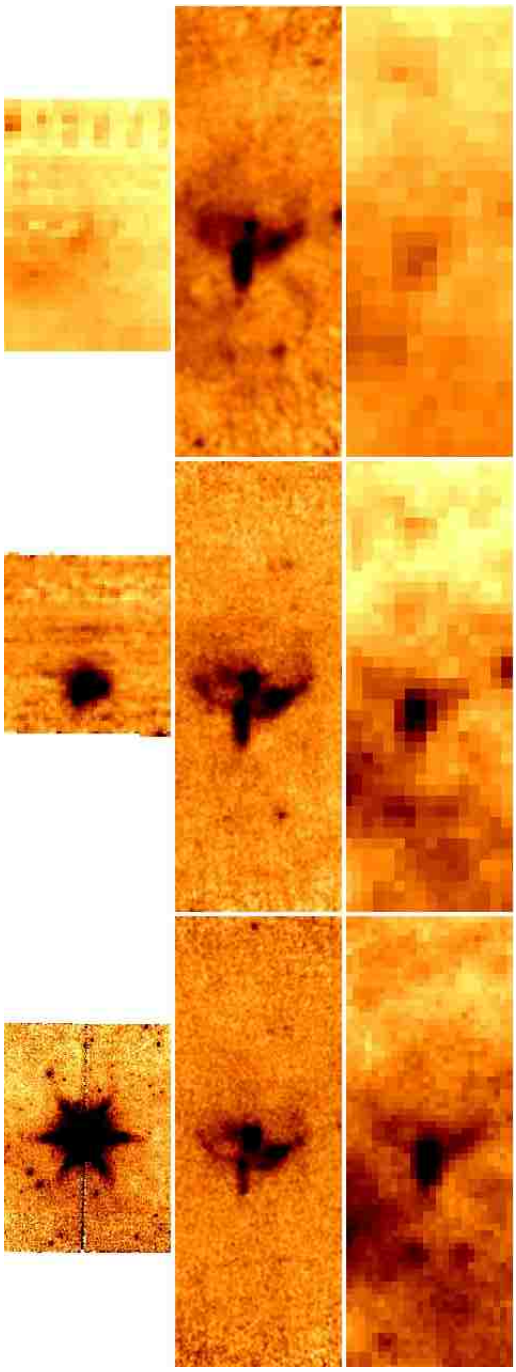

Figure 4.7: First row (starting lower left corner):*Spitzer*/MIPS observations of SU Tau 24, 70, 160 μm, respectively. The field–of–view of the observations (not including white space) are: $8.5' \times 5.75'$, $5.45' \times 5.0'$, and $8.4' \times 5.25'$, respectively. Second row: *Herschel*/PACS observations of SU Tau at 70, 100, and 160 μm, respectively. Third row: *Herschel*/SPIRE observations of SU Tau at 250, 350, and 500 μm, respectively. The field–of–view of the *Herschel* observations are all $7' \times 2.5'$. North is left and East is down.

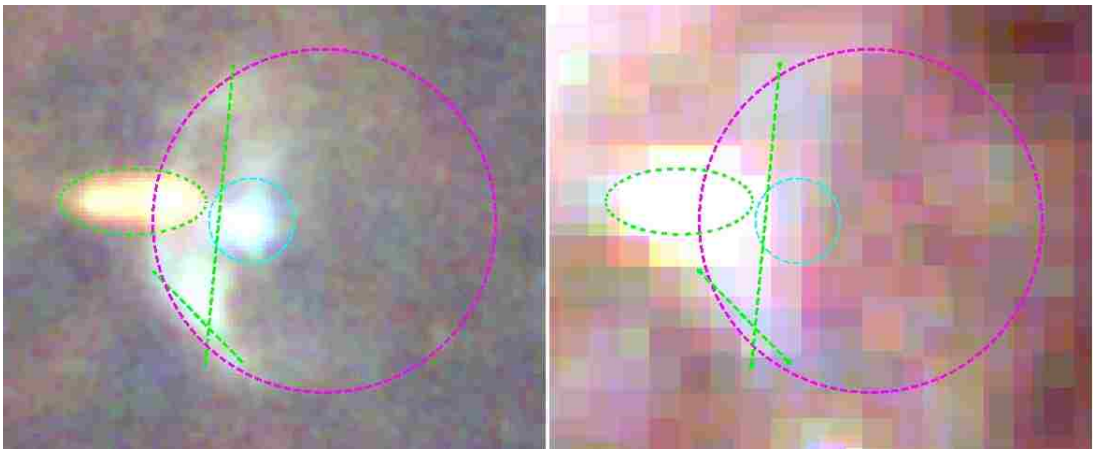

Figure 4.8: Left: Three color *Herschel*/PACS image with the 70, 100, and 160 μm observations being represented by blue, green, and red, respectively. Right: Three color *Herschel*/SPIRE image with 250, 350, and 500 μm observations being represented by blue, green, and red, respectively. The field–of–view in both frames is $3' \times 2.4'$. The cyan circle (radius = 14") is centered on the position of SU Tau, the green ellipse shows the background galaxy separate from SU Tau, and the green lines (1.66' & 0.7' in length) are there to guide the eye to the bow shock feature being associated with SU Tau. The magenta circle (radius = $0.95'$ is centered to have a section of its arc pass through the bow shock and to highlight the diffuse emission west of SU Tau. These observations are now oriented in the traditional astronomical sense: North is up and East is left.

The necessary angular resolution becomes quickly apparent when examining the *Herschel* observations. 2MFGC 4715 and the SU Tau CSM are well separated and can be further distinguished in 3–color images, which can be found in Figure 4.8. PACS is displayed on the left and SPIRE on the right. They are simply 3–color images where the blue, green, and red correspond to the shortest, intermediate, and longest wavelengths within the specific instrument, respectively. The morphology of SU Tau's CSM is unlike that found around any other RCB star. A bow shock type feature, which dominates the eastern half of the image, immediately jumps out in observations with both *Herschel* instruments with definitive detections out to 350 μm. Diffuse nebulosity can be discerned in the western half of the PACS 3–color image.

The outer edge of the bow shock extends from $\sim 30''$ to $50''$ from the central position of SU Tau (see Figure 4.9). This corresponds to a physical distance of 7.41 to 10.8 pc assuming the distance to SU Tau is 3.3 kpc (see Section 4.4.2). The flux of the large overdensity, located in the southeast, was sampled in the *Herschel*/*PACS* observations with an elliptical region with semi–major axis of $2.9''$ and semi–minor axis of $1.8''$. The determined fluxes were 0.0284, 0.0328, and 0.0193 Jy at 70, 100, and 160 μm, respectively. These values correspond to 5%, 10%, and 15% of the calculated flux for the dust emission centered on SU Tau (see Section 4.4.2). Estimated dust temperatures at the location of the outer edge of the bow shock are about 30 K. This is consistent with a blackbody with a peak wavelength of 100 μm, which is exactly

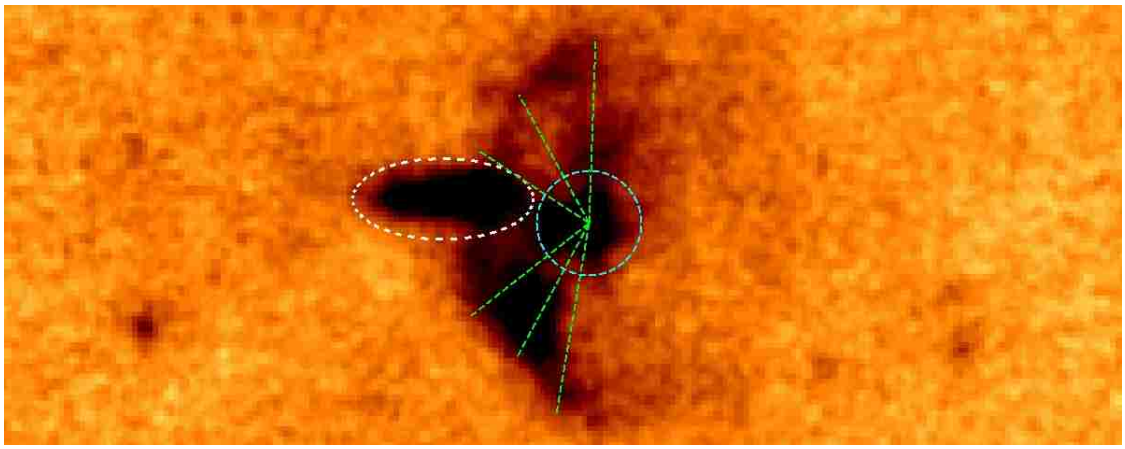

Figure 4.9: A zoom–in ($5.0' \times 2.0'$) of the *Herschel*/PACS 100 μm observation of SU Tau. The white ellipse marks the background galaxy, 2MFGC 4715, while the cyan circle (radius = $14''$) is centered on SU Tau. The six rays beginning from the central coordinates of SU Tau mark extend out to the bow shock are about $30''$ to $50''$ in length. North is up and East is left.

where the maximum flux value for the overdensity was found to be.

It is difficult to determine for certain how long any interaction between the SU Tau CSM and the ISM has been occurring. If we assume that any interaction is much less than the time for the material to expand outward to its current distance from the central star, then we can at least put some bound on its age. Should this material be part of a fossil PN structure, as predicted in the FF scenario, then it would take the material between 2.4×10^5 to 5.3×10^5 years to reach its current location. This assumes that the initial shell was expanding at typical PNe velocities (20–30 km s^{-1}). However, in the DD scenario, the dust would have outward velocities of at least 400 to 900 km s^{-1}. The lower limit comes observations of the He I λ10830 line (Clayton et al., 1992a, 2003, 2013a), while the upper limit comes from simulations of WD mergers (see Section 3.1.3). These velocities indicate the dust would reach the determined distances on the order of 10^4 years.

A search for evidence of this feature in archival observations of SU Tau only come up with a partial detection in the 2MASS J–band (see Figure 4.10). The 2MASS J–band filter has a central wavelength of 1.235 ± 0.006 μm with a bandwidth of 0.162 ± 0.001 μm (Cohen et al., 2003). The wavelength of the electron transition between the fifth to third energy levels of Hydrogen (Paschen–β) is 1.282 μm, which falls within the 2MASS J–band bandwidth.

Stellar bow shocks typically manifest due to interactions between the stellar wind of a rapidly moving star and the denser, slower ISM through which the star is currently moving. Bow shocks have been in the FIR previously (e.g, Ueta et al., 2006; Decin et al., 2012; Cox et al., 2012). The obvious difference between SU Tau, as well as other RCB stars, and these other stars is the extreme hydrogen–deficiency that RCB stars are known to have. In the case of Betelgeuse, the shocks are most likely from hydrogen–rich material that has been previously shed in the star's lifetime (Decin

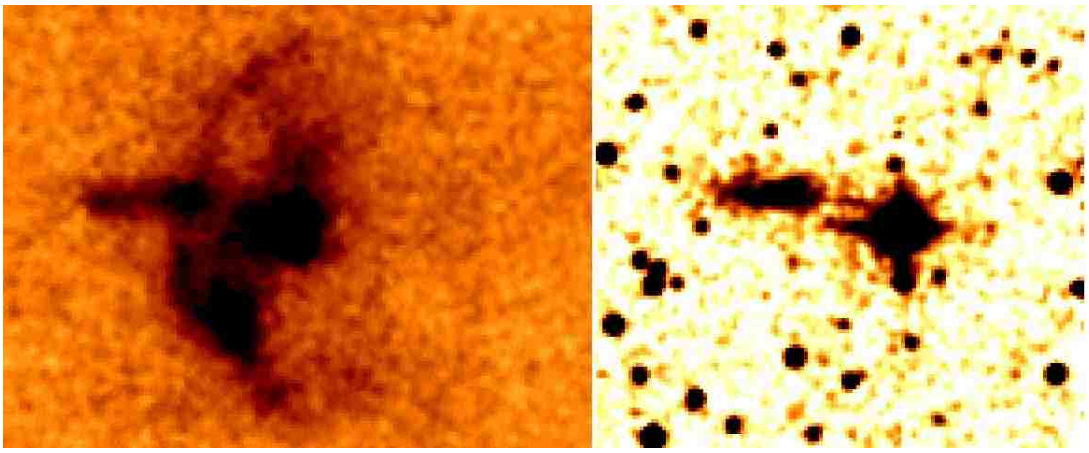

Figure 4.10: Left: A zoom–in ($2.6' \times 2.0'$) of the *Herschel*/PACS 70 μm observation of SU Tau. Right: A $2.0' \times 2.0'$ field of the 2MASS J–band tile containing SU Tau. The bow shock that is prominently seen on the left can be partly seen as a $0.5'$ vertical line to the East of SU Tau in the 2MASS observation. North is up and East is left.

et al., 2012) moving against denser ISM in front of the central star's motion through the Galaxy. In the case of SU Tau, this lends itself to the question: what is the composition of the material being shocked? If SU Tau was formed via the FF scenario, then having H–rich material at the outskirts of its CSM is not surprising. Although if the dust envelopes of RCB stars are mostly helium filled, then the presence of shocked H–rich material could be from the ISM that SU Tau is moving into.

4.4.2 Radiative Transfer Modeling

SU Tau's archival maximum–light photometry and spectroscopy were combined with photometry from the unpublished *Spitzer*/MIPS, *Herschel*/PACS, and *Herschel*/SPIRE (3σ upper limits) observations to construct its SED, which can be seen in Figure 4.11. The bow shock feature was not included in the photometry aperture, and the background galaxy was masked out in all *Herschel* observations. Further, it is highly likely that the IRAS 60 μm, 100 μm, and AKARI 100 μm points are contaminated by flux from the background galaxy. These points are still included on the SED, but had no influence on determining the final fit model. The dashed line represents the best–fit MCRT model from MOCASSIN. The photometry is found in Table 4.4. A blackbody with $T_{eff} = 6500$ K was adopted from atmosphere modeling by Asplund et al. (2000). A distance of 3.3 kpc was determined by assuming an absolute V–band magnitude of -5 (Tisserand et al., 2009). This results in an input luminosity of 10,450 $L_{\odot}$ for SU Tau.

Table 4.4: SU Tau Photometry

Band	Flux (Jy)	σ (Jy)
B (0.433)	0.241	0.004
V (0.550)	0.560	0.010
$R_{\rm C}$ (0.640)	0.827	0.015
$I_{\rm C}$ (0.790)	0.977	0.018
J (1.25)	1.60	0.044
H (1.60)	1.70	0.047
K (2.20)	1.94	0.054
L (3.40)	3.57	0.099
WISE/3.4	3.62	0.260
WISE/4.6	11.1	0.675
AKARI/9	14.7	0.050
IRAS/12	9.48	0.759
WISE/12	7.77	0.079
AKARI/18	6.16	0.046
WISE/22	3.38	0.037
MIPS/24	3.07	0.037
IRAS/25	4.12	0.288
IRAS/60	1.54	0.139
AKARI/65	0.351	Upper Limit
MIPS/70	0.322	0.003
PACS/70	0.523	0.002
AKARI/90	1.18	0.080
IRAS/100	2.87	0.315
PACS/100	0.318	0.002
MIPS/160	0.142	0.007
PACS/160	0.133	0.001
SPIRE/250	0.117	Upper Limit
SPIRE/350	0.064	Upper Limit
SPIRE/500	0.028	Upper Limit

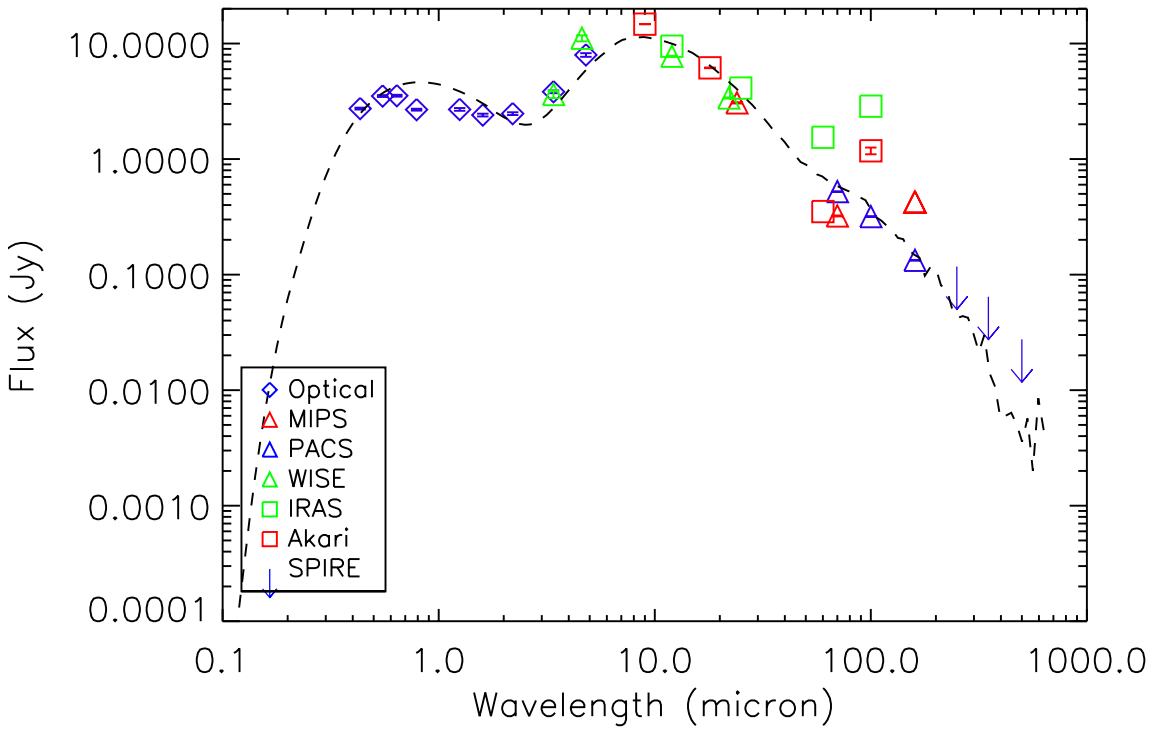

Figure 4.11: The maximum–light SED of SU Tau. Open blue diamonds: $BVR_{\rm C}I_{\rm C}JHKL$; open green triangles: WISE (3.4, 4.6, 12.0, 22.0 μm ; open red squares: AKARI (9, 18, 65, 90 μm); open red triangles: *Spitzer*/MIPS (24, 70, 160 μm); open green squares: IRAS (12, 25, 60, 100 μm); open blue triangles: *Herschel*/PACS (70, 100, 160 μm); blue arrows (3σ): *Herschel*/SPIRE (250, 350, 500 μm). The sum of the best–fit MOCASSIN models for the central source, warm, and cold dust shells is represented by the dashed black line.

The SU Tau CSM begins to be dominate the SED beginning around 2.2 μm (K–band), which indicates the presence of warm dust. A spherical envelope with inner radius at 2.10×10^{15} cm and outer radius at 4.25×10^{16} cm describes the SED from 1.6 μm out to barely before the 70.0 μm points. The dust mass of this envelope is 2.27×10^{-6} $M_{\odot}$ with temperatures ranging from ∼600 K down to ∼150 K. This regime was also included in the blackbody fitting analysis by García-Hernández et al. (2011b). They were able to fit a blackbody temperature of 6500 K, which agrees with the temperature determined by Asplund et al. (2000). The IR excess was fit with a 635 K blackbody (García-Hernández et al., 2011b), which is in agreement with the temperature range from my MOCASSIN RT modeling.

However, a second excess can be seen to arise for photometry longer than 70 μm as the points lie above where a dust envelope model would predict them to be. A second envelope was modeled with an inner radius at 1.00×10^{18} cm and extending outward to 9.00×10^{18} cm. The dust mass of this envelope is 6.80×10^{-4} $M_{\odot}$ with temperatures ranging from ∼50 K down to ∼25 K.

4.5 UW Cen

Brightness fluctuations in UW Cen were first noticed by Leavitt & Pickering (1906) when it exhibited a 1.6 mag change. No comments as to what kind of variable were made by Leavitt & Pickering. The earliest mention of UW Cen exhibiting RCB–like behavior is in the *Annals of Harvard College Observatory* (Gaposchkin, 1952). UW Cen is one of two stars (the other V854 Cen–see below) that has been examined for ^{18}O, ^{19}F, and Li. Lithium has been known about in UW Cen since Lambert & Rao (1994) found the Li resonance doublet at 6707 Å in its spectrum. Pandey et al. (2008) discovered ^{19}F by absorption lines at 6834.26, 6902.47, 7398.68, and 7425.6 Å. The search for ^{18}O resulted in a null detection owing to the large amount of CSM and the effective temperature of UW Cen being too warm to display molecular features (García-Hernández et al., 2009).

The CSM of UW Cen is unique among all of the RCB stars. It is the only RCB star discovered to have a reflection nebula surrounding it (Pollacco et al., 1991; Clayton et al., 1999). The nebula is ~ 15" in diameter. It is only visible either during deep declines when the dust along the line of sight serves as a "natural" coronagraph or an actual coronagraph is used to block the light from the central star. Clayton et al. (1999) found that the morphology of the nebula had changed between their observations and those of Pollacco et al. (1991). These changes were too fast for any physical changes in the nebula to be occurring. Clayton et al. (1999) deduced that the changes in the shell were due to simply the changing pattern of clouds, which affect how light from UW Cen illuminates the reflection nebula.

4.5.1 Image Inspection

The longest wavelength photometric observations of UW Cen that had been previously examined where the IRAS observations from the 1980s (Walker, 1986; Schaefer, 1986). Archival, unpublished *Spitzer*/MIPS (top row) 24, 70, 160 μm and *Herschel*/PACS (bottom row) 70, 100, and 160 μm observations are presented in Figure 4.12. The images are all oriented in the astronomical format of North–up and East–left and colors have been inverted to show positive flux as darker. The *Spitzer*/MIPS images represent a significant step forward in both sensitivity and angular resolution of the nebulosity surrounding UW Cen. However, the UW Cen CSM still appears as a point source at all three wavelengths.

The higher angular resolution provided by *Herschel*/PACS allows for a better determination of the morphology of the UW Cen CSM. The 70 μm image reinforces the brightness seen at the matching wavelength in *Spitzer*/MIPS. The morphology of the observations are mostly the same, spherical, at 100 and 160 μm. However, a noticeable difference between the *Spitzer* and *Herschel* observations is the diffuse nebulosity that can be discerned from the brighter central material. This material, found in all three *Herschel*/PACS wavelengths, lies beyond the reflection nebula (diameter $\sim 15''$) known to exist around UW Cen.

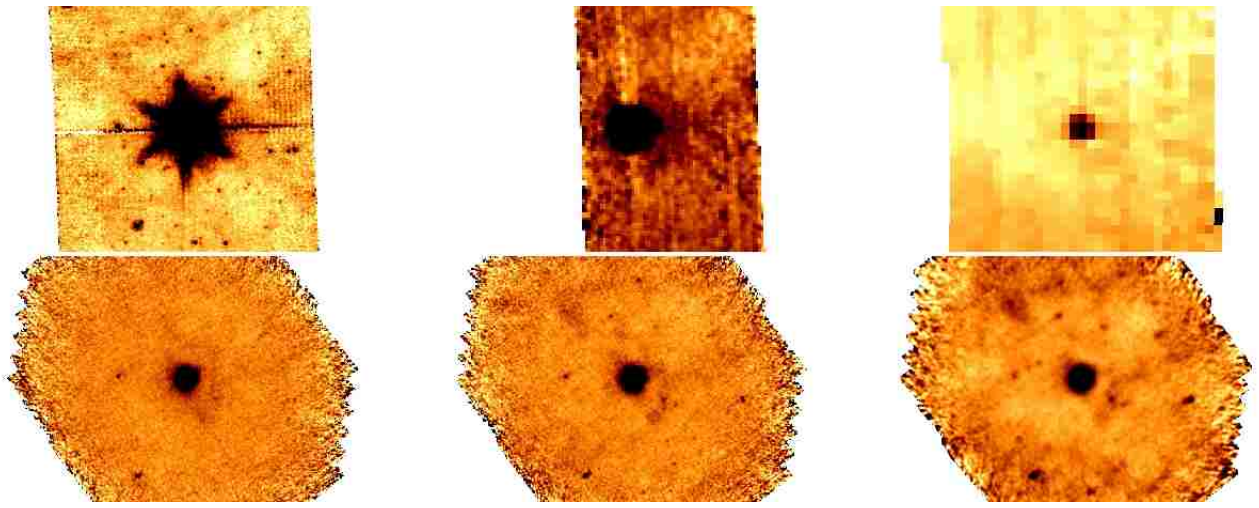

Figure 4.12: Top row:*Spitzer*/MIPS observations of UW Cen 24, 70, 160 μm, respectively. Bottom row: *Herschel*/PACS observations of UW Cen at 70, 100, and 160 μm, respectively. The field–of–view in the *Spitzer* images are all $8.0' \times 7.5'$ and in the *Herschel* images are all $10.6' \times 7.5'$. North is up and East is left.

4.5.2 Radiative Transfer Modeling

The maximum–light UW Cen SED was made by combining archival photometry and spectroscopy with unpublished photometry from *Spitzer*/MIPS and *Herschel*/PACS observations. The SED can be found in Figure 4.13, and all input photometry in Table 4.5. The dashed line plotted over the SED represents the best–fit MCRT model from MOCASSIN. Asplund et al. (2000) found from their modeling of spectra against line–blanketed models of stellar atmospheres that the effective temperature of UW Cen is most likely 7500 K. This temperature has been adopted for my MCRT modeling. The distance to UW Cen, 3.5 kpc, was calculated from the relation between absolute V–band magnitude and $V - I$ color presented in (Tisserand et al., 2009). This is a departure from the previous distance calculation of 5.5 kpc (Lawson et al., 1990a; Clayton et al., 1999), due to underestimating the line of sight extinction. This new distance results in an input luminosity of 7,320 $L_{\odot}$.

Table 4.5: UW Cen Photometry

Band	Flux (Jy)	σ (Jy)
U (0.365)	0.234	0.002
B (0.433)	0.594	0.005
V (0.550)	1.020	0.009
$R_{\rm C}$ (0.640)	1.170	0.011
$I_{\rm C}$ (0.790)	1.340	0.012
J (1.25)	1.350	0.025
H (1.60)	1.090	0.020
K (2.20)	0.879	0.016
L (3.40)	1.070	0.049
WISE/3.4	2.150	0.105
IRAC/3.6	5.260	0.026
IRAC/4.5	6.690	0.034
WISE/4.6	8.660	0.263
IRAC/5.8	7.690	0.054
IRAC/8.0	9.050	0.060
AKARI/9	9.760	0.070
IRAS/12	7.850	0.471
WISE/12	6.820	0.044
AKARI/18	5.700	0.047
WISE/ 22	4.570	0.046
MIPS/24	4.350	0.011
IRAS/25	5.750	0.345
IRAS/60	9.220	0.737
AKARI/65	6.650	0.413
MIPS/70	5.570	0.007
PACS/70	2.130	0.003
AKARI/90	7.300	0.332
IRAS/100	5.940	0.594
PACS/100	4.950	0.006
AKARI/140	4.180	0.349
MIPS/160	2.530	0.055
AKARI/160	2.810	1.020
PACS/160	2.470	0.004

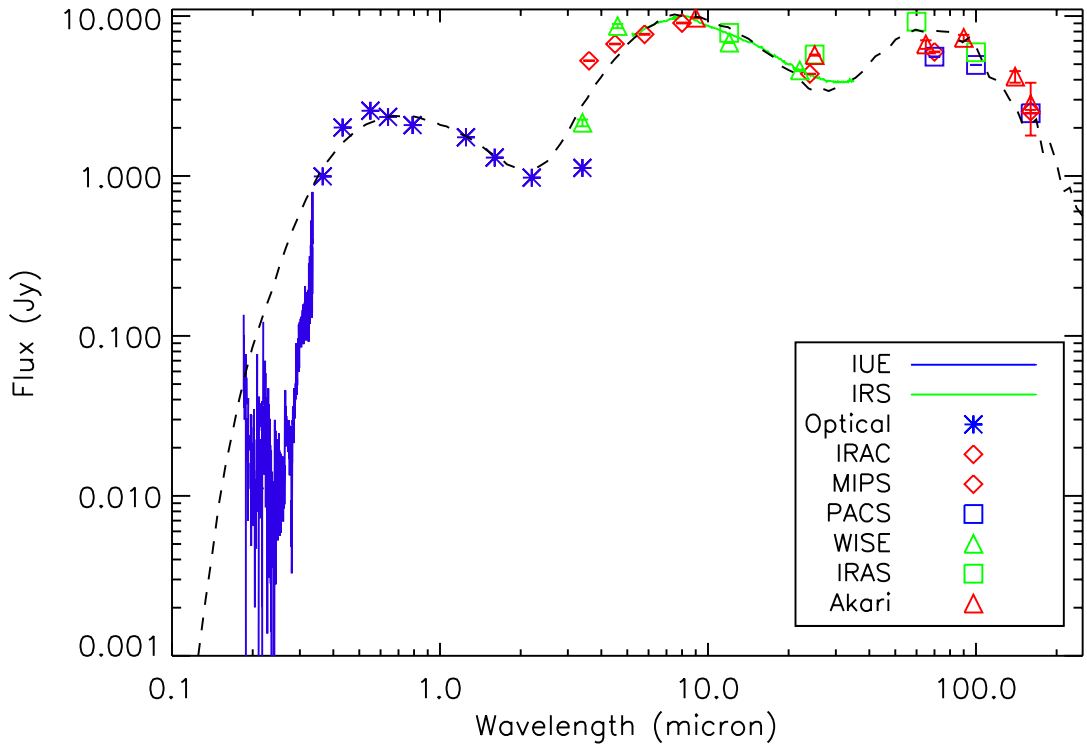

Figure 4.13: The maximum–light SED of UW Cen. Blue line: IUE spectrum; blue asterisks: $UBVR_{\rm C}I_{\rm C}JHKL$; open red diamonds: *Spitzer*/IRAC (3.6, 4.5, 5.8, 8.0 μm) and *Spitzer*/MIPS (24, 70, 160 μm); open green triangles: WISE (3.4, 4.6, 12.0, 22.0 μm); green line: *Spitzer*/IRS spectrum; open green squares: IRAS (12, 25, 60, 100 μm); open red triangles: AKARI (9, 25, 65, 90, 140 and 160 μm); open blue squares: *Herschel*/PACS (70, 100, 160 μm). The sum of the best–fit MOCASSIN models for the central source, warm, and cold dust shells is represented by the dashed black line.

The UW Cen SED begins to show the influence from CSM after 2.2 μm (K–band). A spherical envelope with inner radius at 1.55×10^{15} cm and outer radius at 4.50×10^{16} cm describes the SED from 1.60 out to ∼25.0 μm points. The dust mass of this envelope is 2.40×10^{-6} $M_{\odot}$ with temperatures ranging from ∼600 K down to ∼150 K. This part of the SED is dominated by the presence of warm dust surrounding the central star. The variability in measurements around 3 μm is due to changes in the amount of warm dust that has recently condensed around UW Cen at the times the observations were taken.

UW Cen's SED at wavelengths longer than ∼30 μm is unlike that any other known RCB star. A clear second dust component can be seen as the long–low resolution IRS spectrum starts to rise again to a peak around 70 μm before falling again at wavelengths longer than 100 μm. This component was also modeled with a spherical envelope with an inner radius at 7.00×10^{17} cm and outer radius of 2.50×10^{18} cm. The dust mass of this envelope is 5.14×10^{-3} $M_{\odot}$ with temperatures ranging from ∼70 K down to ∼40 K.

Analysis of the UW Cen SED was previously presented by both Clayton et al. (1999) and García-Hernández et al. (2011b). Clayton et al. (1999) fit only the optical to MIR with two Planck functions (blackbody fitting) of temperatures 6000±500 and 650±50 K (see their Figure 3). They do not fit wavelengths longer than 12 μm due to the possibility of contamination from IR bright cirrus clouds along the line of sight to UW Cen. However, they do comment that this contribution can be fit with a Planck function of 100 K. A dust mass of $\sim 6 \times 10^{-4}$ $M_{\odot}$ is derived with a total mass of $\sim$ 0.2 $M_{\odot}$ assuming a normal gas–to–dust ratio (Clayton et al., 1999).

A four component fit, stellar + three to account for CSM contribution, was adopted by García-Hernández et al. (2011b). Similar to Clayton et al. (1999), their fits are only comprised of Planck functions. The temperatures of the blackbody fits were 7500, 630, 120, and 50 K (García-Hernández et al., 2011b). No estimate for the dust masses of any of the components are presented.

4.6 V854 Cen

In terms of RCB stars, V854 Cen was discovered relatively recently. In 1986 V854 Cen (NSV 6708) was found to be at 7.5 mag when the previous brightest known maximum for this star was at 9.7 mag (McNaught & Dawes, 1986). Further analysis of archival plates and film by McNaught & Dawes (1986) found that the star appeared as faint as 15.5 mag. The peak V–band brightness 7 mag makes V854 Cen the third brightest RCB star in the entire sky after R CrB and RY Sgr. A star of that brightness would not have gone overlooked by the community at-large. An examination of archival plates by McNaught (1986) found that V854 Cen had been in decline since at least 1913, which implies that it had been continuously forming dust along the line of sight during the intervening years.

The abundances of V854 Cen are extremely bizarre for a class of already exotic objects. Lawson & Cottrell (1989) found that V854 Cen was much more H–rich than R CrB, and for that matter any other known RCB star. It is one of four RCB stars that compose the designation "minority" RCB stars (Lambert & Rao, 1994). This classification is made primarily by the iron abundances of these RCB stars in relation to the rest of the class. V854 Cen is also one four RCB stars that show appreciable levels of ^{13}C from the analysis of the $^{12}C^{13}C$ Swan bandhead (Hema et al., 2012). This isotope of carbon is found in FF objects like Sakuari's object, but not in the majority of RCB or HdC stars. It has been examined for any signs of ^{18}O, ^{19}F, or Li and all have resulted in no detections (Lambert & Rao, 1994; Pandey et al., 2008; García-Hernández et al., 2009). Finally, it has been found to have C_{60} emission from *Spitzer*/IRS observations (García-Hernández et al., 2011a).

4.6.1 Image Inspection

In a similar fashion to MV Sgr, the only FIR observations of V854 Cen are provided by *Spitzer*/MIPS. The 24, 70, and 160 μm observations, left to right, respectively, can be found in a 3–panel postage stamp displayed in Figure 4.14. The images are all oriented in the astronomical format of North–up and East–left and colors have

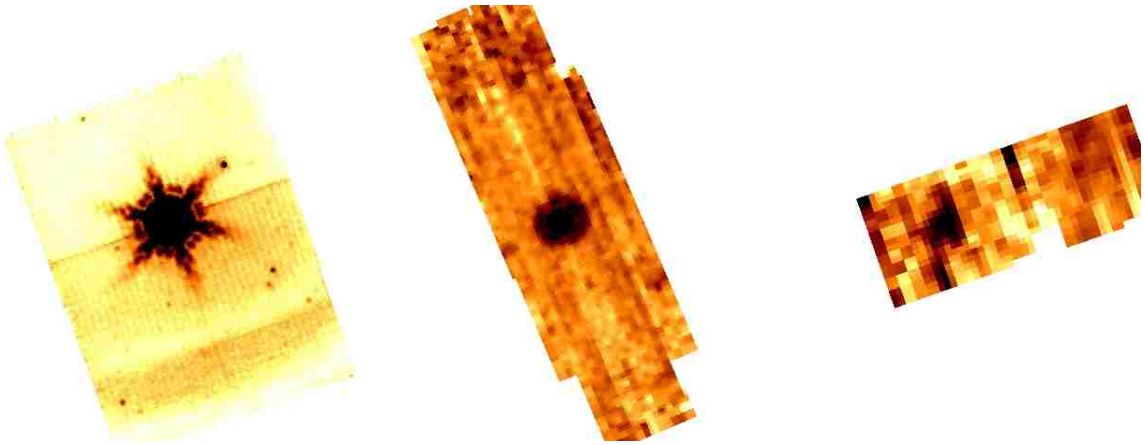

Figure 4.14: The *Spitzer*/MIPS observations of V854 Cen at 24, 70, 160 μm, respectively. The field–of–views shown (not accounting for white space) are $6.0' \times 7.8'$, $3.4' \times 7.0'$, and $5.4' \times 2.7'$, respectively. North is up and East is left.

been inverted to show positive flux as darker. Not much about the morphology of the V854 Cen CSM is able to be determined from these observations. This is likely reflected due to a large reservoir of dust that should exist surrounding V854 Cen due to its nearly half–century decline.

4.6.2 Radiative Transfer Modeling

The inputs for the maximum–light SED of V854 Cen are similar to that of MV Sgr. Specifically, this means that archival photometry and spectroscopy are combined with unpublished *Spitzer*/MIPS photometry. The SED can be seen in Figure 4.15 and all input photometry in Table 4.6. The dashed line represents the best–fit MCRT model from MOCASSIN. An input stellar blackbody with an effective temperature of 6,750 K was adopted from atmosphere modeling of Asplund et al. (2000). A distance of 2.28 kpc was determined by assuming an absolute V–band magnitude of -5 (Tisserand et al., 2009). This results in an input luminosity of 11,760 $L_{\odot}$.

Table 4.6: V854 Cen Photometry

Band	Flux (Jy)	σ (Jy)
U (0.365)	1.450	0.036
B (0.433)	3.820	0.095
V (0.550)	5.500	0.137
$R_{\rm C}$ (0.640)	6.067	0.152
$I_{\rm C}$ (0.790)	6.512	0.163
2MASS/J (1.24)	5.756	0.095
J (1.25)	6.998	0.193
H (1.60)	8.268	0.229
2MASS/H (1.66)	5.399	0.085
2MASS/$K_{\rm S}$ (2.16)	7.480	0.124
K (2.20)	12.50	0.345
L (3.40)	27.50	0.761
AKARI/9	23.00	1.170
IRAS/12	23.00	1.150
AKARI/18	7.364	0.033
MIPS/24	4.944	0.001
IRAS/25	7.820	0.469
IRAS/60	1.510	0.136
AKARI/65	0.940	Upper Limit
MIPS/70	0.641	0.001
PACS/70	2.132	0.003
AKARI/90	0.705	0.036
IRAS/100	1.030	Upper Limit
AKARI/140	0.185	Upper Limit
MIPS/160	0.068	0.001
AKARI/160	1.040	Upper Limit

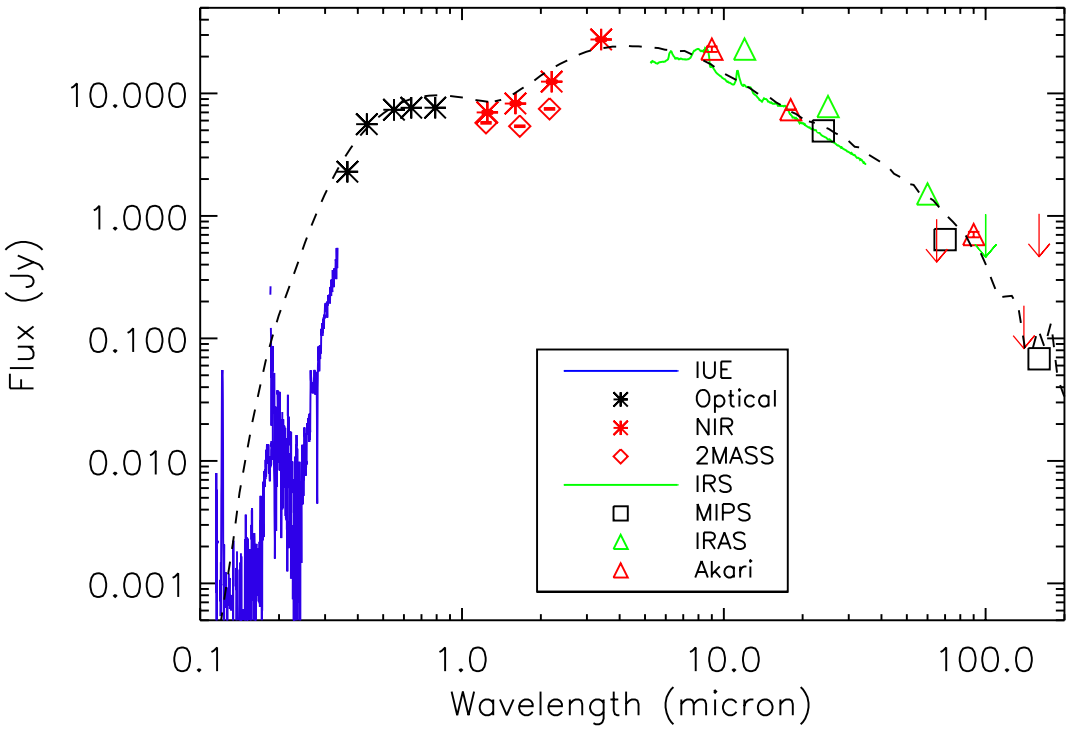

Figure 4.15: The maximum–light SED of V854 Cen. Blue line: IUE spectrum; black asterisks: $UBVR_{\rm C}I_{\rm C}$; red asterisks: $JHKL$; open red diamonds: 2MASS $JHK_{\rm S}$; green line: *Spitzer*/IRS spectrum; open black squares: *Spitzer*/MIPS (24, 70, 160 μm); open green triangles and arrow (3σ): IRAS (12, 25, 60, 100 μm); open red triangles and arrow (3σ): AKARI (9, 18, 65, 90, 140, 160 μm). The sum of the best–fit MOCASSIN models for the central source, warm, and cold dust shells is represented by the dashed black line.

Warm dust in the V854 Cen CSM starts to influence the SED after 1.6 μm. This dust component was modeled with an envelope that has an inner radius at 4.88×10^{14} cm and outer radius 1.00×10^{16} cm. The dust mass of this envelope is 3.08×10^{-7} $M_{\odot}$ with temperatures ranging from ∼1,200 K down to ∼300 K.

A second envelope was also modeled with an inner radius at 3.45×10^{16} cm and extending outward to 1.00×10^{18} cm. In order to account for a slight excess in the photometry at wavelengths longer than 60 μm, which indicates the presence of a colder reservoir of dust. The dust mass in this envelope is 2.60×10^{-5} $M_{\odot}$ with temperatures ranging from ∼200 K down to ∼50 K.

The maximum light SED was also in the blackbody fitting performed by García-Hernández et al. (2011b). A three component (star + two IR excess) was found by García-Hernández et al. to best describe the SED. V854 Cen was fit with a 6750 K blackbody, while the two IR excess with blackbodies of 900 and 140 K (García-Hernández et al., 2011b). The stellar component agrees with the temperature derived by Asplund et al. (1998), which I adopted as well for my modeling. The temperatures for the IR excesses fall within the ranges for my two modeled envelopes.

4.7 V CrA

Changes of at least 1 mag in the brightness of a star that would later be classified V CrA were first reported by Pickering & Leland (1896). V CrA was found to have an enrichment of ^{13}C by the detection of the ^{12}C^{13}C Swan bandhead (Rao & Lambert, 2008a). This makes it one of four RCB stars to have this isotope of carbon. No appreciable level of Li was found to be in its photosphere (Lambert & Rao, 1994). Pandey et al. (2008) detected only a single absorption line for ^{19}F at 6902.47 Å, which limits the reliability of claiming a definitive detection.

4.7.1 Image Inspection

The determination of a presence or absence of any diffuse nebulosity surrounding V CrA was performed with *Spitzer*/MIPS, *Herschel*/PACS, and *Herschel*/SPIRE observations. These images displayed as postage stamps can be found in Figure 4.16. They are from lower–left to top–right: *Spitzer*/MIPS 24, 70, and 160 μm, *Herschel*/PACS 70, 100, 160 μm, and *Herschel*/SPIRE 250, 350, and 500 μm. The images are all oriented with North–left and East–down and colors have been inverted to show positive flux as darker. At 24 μm, V CrA is no different than any other RCB star in that it appears as the *Spitzer*/MIPS PSF. The *Spitzer*/MIPS 70 μm detection of V CrA is predominantly the PSF in this band as well, which makes resolving any diffuse nebulosity difficult. The 160 μm field hints at a possibly seeing material associated with V CrA, illustrating the great sensitivity *Spitzer*/MIPS provides, but the resolution is not enough to definitively tell.

The improved angular resolution with *Herschel*/PACS allows accurate detections of V CrA at all three wavelengths. Unfortunately, there is nothing more than the *Herschel*/PACS PSF in these observations. There does appear to be a hint of nebulosity in the North–South direction. The V CrA images are an excellent opportunity to try performing deconvolution to separate out the PSF from diffuse nebulosity. However, the non–symmetry in the PACS PSFs make this task difficult with standard routines such as Lucy deconvolution. An effort was made to obtain code that could successfully perform deconvolution on Herschel/PACS observations. However, this code was not able to be acquired. The *Herschel*/SPIRE observations show no signs of cold, diffuse nebulosity centered around the position of V CrA.

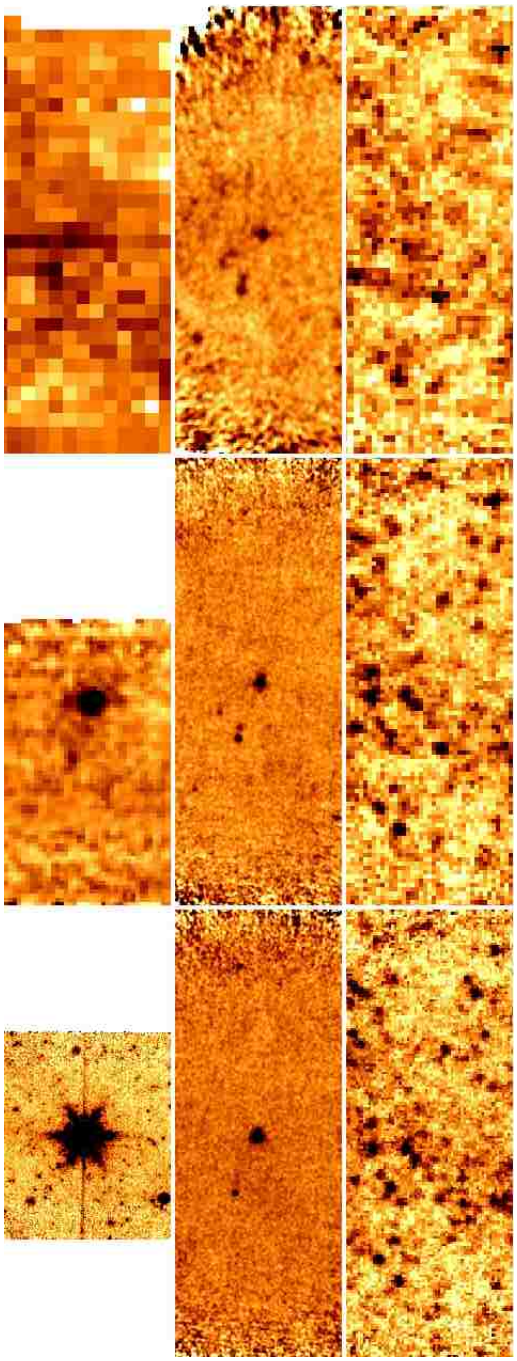

Figure 4.16: First row (starting lower left corner):*Spitzer*/MIPS observations of V CrA 24, 70, 160 μm, respectively. The field–of–view, ignoring white spaces, displayed at 24 μm is $8.5' \times 6.25'$, at 70 μm $5.5' \times 3.2'$, and at 160 μm $8.0' \times 3.1'$. for all three bands is $25' \times 10'$. Middle row: *Herschel*/PACS observations of V CrA at 70, 100, and 160 μm, respectively. The field–of–view in all three 3 columns is $8.5' \times 3.2'$. Bottom row: *Herschel*/SPIRE observations of V CrA at 250, 350, and 500 μm, respectively. The field–of–view for all three bands is $17.1' \times 6.3'$. North is left and East is down.

4.7.2 Radiative Transfer Modeling

The V CrA SED was made from available maximum–light photometry and spectroscopy, which were combined with photometry from unpublished *Spitzer*/MIPS, *Herschel*/PACS, and *Herschel*/SPIRE. The photometry can be found in Table 4.7, while the SED is displayed in Figure 4.17. The *Spitzer*/MIPS 160 μm and *Herschel*/SPIRE are all 3σ upper limits. The dashed line represents the best–fit MCRT model from MOCASSIN. A blackbody with T_{eff} = 6250 K was adopted from atmosphere modeling by Asplund et al. (2000). A distance of 5.5 kpc was determined by assuming an absolute V–band magnitude of −5 (Tisserand et al., 2009). This results in an input luminosity of 6,550 $L_{\odot}$.

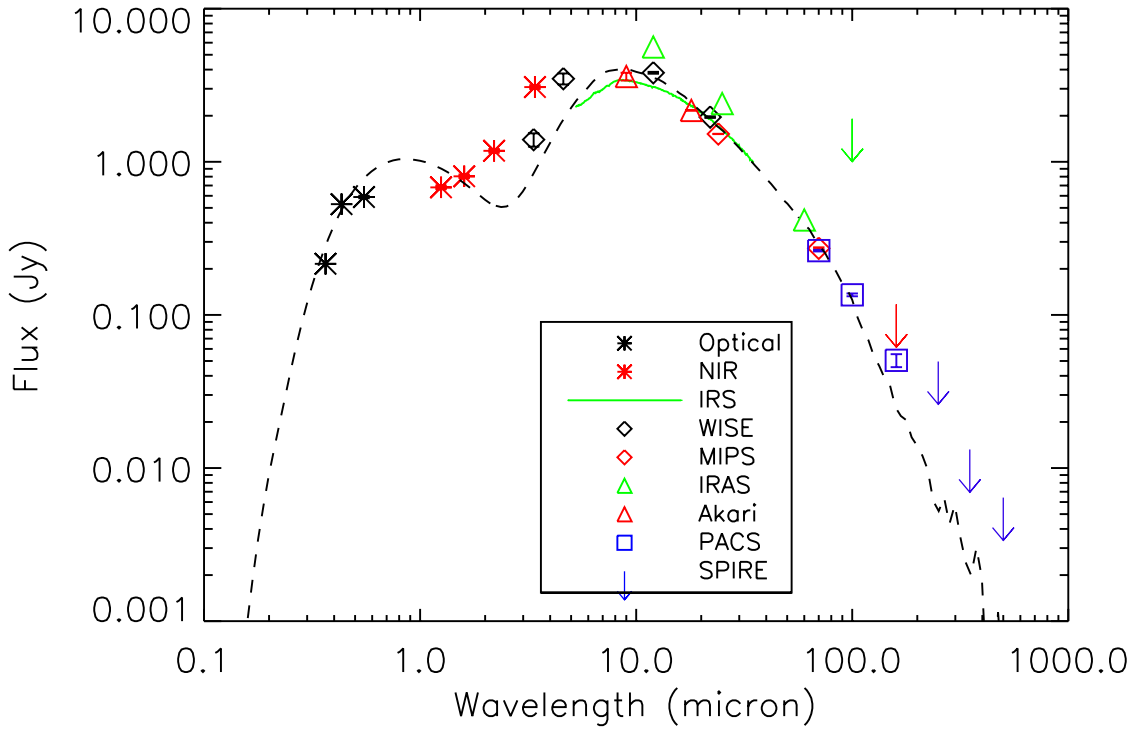

Figure 4.17: The maximum–light SED of V CrA. Black asterisks: *UBV*; red asterisks: *JHK*; open black diamonds: WISE (3.4, 4.6, 12.0, 22.0 μm); green line: *Spitzer*/IRS spectrum; open red diamonds: *Spitzer*/MIPS (24 and 70 μm); open green triangles and arrow (3σ): IRAS (12, 25, 60, 100 μm); open red triangle and arrow (3σ): AKARI (9, 18, 65, 90 μm); open blue squares: *Herschel*/PACS (70, 100, 160 μm); blue arrows (3σ): *Herschel*/SPIRE (250, 350, 500 μm). The sum of the best–fit MOCASSIN models for the central source, warm, and cold dust shells is represented by the dashed black line.

The influence from warm dust in the V CrA CSM starts to become prominent after 1.6 μm (*H*–band). This material was modeled by a spherical envelope with inner radius at 1.70×10^{15} cm and outer radius at 4.90×10^{16} cm. The dust mass of this envelope is 4.00×10^{-6} $M_{\odot}$ with temperatures ranging from ∼500 K down to

Table 4.7: V CrA Photometry

Band	Flux (Jy)	σ (Jy)
U (0.365)	0.138	0.003
B (0.433)	0.364	0.007
V (0.550)	0.444	0.008
J (1.25)	0.681	0.019
H (1.60)	0.804	0.022
K (2.20)	1.180	0.033
L (3.40)	3.080	0.085
WISE/3.4	1.400	0.139
WISE/4.6	3.490	0.286
AKARI/9	3.610	0.210
IRAS/12	5.660	0.226
WISE/12	3.820	0.053
AKARI/18	2.170	0.013
WISE/22	1.960	0.025
MIPS/24	1.520	0.003
IRAS/25	2.460	0.172
IRAS/60	0.405	0.036
MIPS/70	0.272	0.004
PACS/70	0.263	0.003
AKARI/90	1.490	0.114
IRAS/100	1.320	Upper Limit
PACS/100	0.135	0.003
MIPS/160	0.117	Upper Limit
PACS/160	0.051	0.005
SPIRE/250	0.050	Upper Limit
SPIRE/350	0.013	Upper Limit
SPIRE/500	0.006	Upper Limit

$\sim$150 K.

As with the other RCB stars, one dust envelope is not able to describe the entire SED. Thus a second envelope was modeled to describe the presence of colder CSM surrounding V CrA. This envelope was modeled with an inner radius at 1.00×10^{17} cm and extending outward to 1.00×10^{18} cm. The dust mass of this envelope is 5.90×10^{-5} $M_{\odot}$ with temperatures ranging from $\sim$130 K down to $\sim$50 K.

The blackbody fitting to the V CrA maximum light SED is among the most bizarre in the sample of García-Hernández et al. (2011b). A fit that includes only optical and *Spitzer* observations was best described by three components (star + two IR excesses); while the fitting of optical, $KLMN$, and IRAS 25μm observations yielded four components (star + three IR excesses) (García-Hernández et al., 2011b). V CrA was fit with a 6500 K blackbody in both models, which agrees with the spectroscopic effective temperature (Rao & Lambert, 2008b), and is not vastly different than the 6250 K (Asplund et al., 2000) used in my modeling. The temperatures in the two IR excess scenarios agree with the ranges determined by the two modeled envelopes. My MOCASSIN modeling also appears to point to the need of a small reservoir of hot dust close to V CrA to account for the flux values in MN and first two channels of WISE.

4.8 Sample Properties

The following analysis will focus on the sample RCB stars that comprise my thesis as a whole rather than individually. This will allow for an examination of any similarities and differences that might arise. A strong emphasis will be placed on any conclusions drawn in the context of only having a very limited number of stars in my sample. However, RCB stars are themselves very rare objects, which makes it possible that my sample is a valid representation of the total population. The average properties will also be compared against the HdC star, HD 173409, and the final flash object, V605 Aql.

4.8.1 CSM Morphology

A major surprise of the MCRT SED modeling of the individual RCB stars is that they *all* required the modeling of two discrete, thick dust shells. The SEDs of MV Sgr, RY Sgr, and UW Cen are all clear cases that a second dust component is necessary, while R CrB, SU Tau, V854 Cen, and V CrA appear like a single, continuous envelope should have been able to describe their SEDs. In fact, the modeling for all of these stars originally began with one envelope as represented by the blue dashed line in Figure 4.18. However, the models did not match the SEDs in the FIR and sub-mm. Hence, a second shell, shown as the red dashed line in Figure 4.18, was modeled to provide the necessary contribution from cold dust. This two component fit agrees with previous MCRT modeling of R CrB, which also described the observed SED with two components (disk + envelope) (Clayton et al., 2011a).

The results of my MCRT agree with those of Nagendra & Leung (1996), who performed analytic modeling (AM) and radiative transfer modeling (RTM) of the

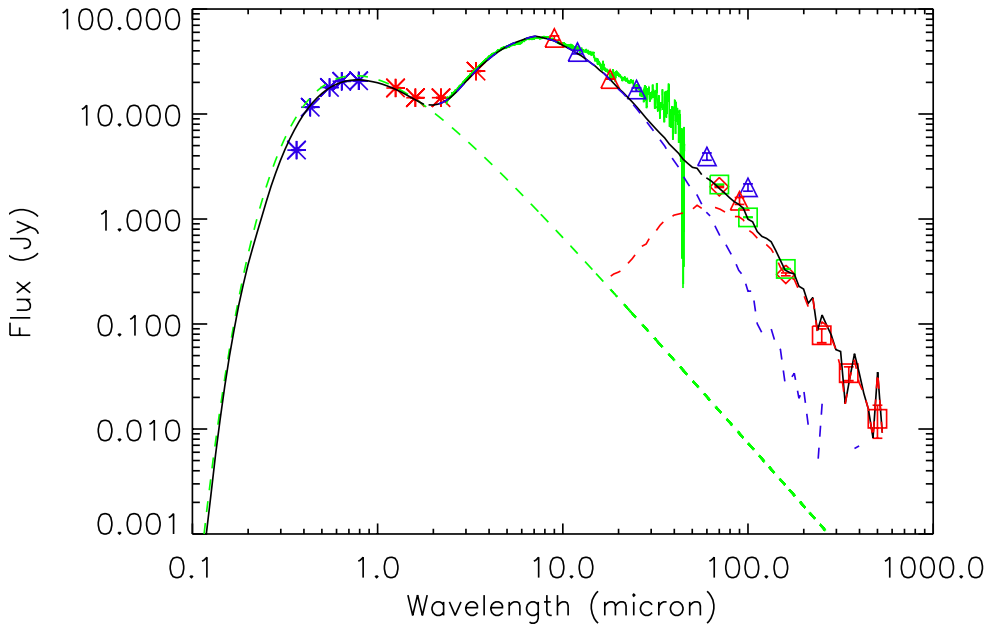

Figure 4.18: The maximum–light SED of R CrB with the same configuration as Figure 4.4. The dashed green line represents a blackbody curve with temperature equal to 6750 K. The dashed blue line represents the contribution from the inner envelope, which begins to poorly describe the R CrB SED at wavelengths longer than $\sim$25 μm. Thus, the need for a second (outer) envelope, which is represented by the dashed red line. Its begins to contribute at roughly 15 μm, and describes the FIR/sub-mm regime extremely well. The sum of the best–fit MOCASSIN models for the central source, warm, and cold dust shells is represented by the solid black line.

R CrB SED. Nagendra & Leung used the available IRAS data (Gillett et al., 1986) in their modeling and they determined that a double shell was the primary way to fit the SED. Both their AM and RTM was unable to describe emission longer than 60 μm with only one shell. However, Nagendra & Leung did investigate how to model the R CrB SED with a single dusty envelope. They had to greatly increase the contribution from the interstellar radiation field (ISRF) in order to accomplish this. They found that this increase had to be anywhere from a factor of 3–30 (depending on the density profile of the shell) the ISRF for the location of R CrB (Nagendra & Leung, 1996).

I also investigated whether or not the maximum–light SEDs could be described by "thin" dust envelopes. The qualification for an envelope as being thin was that $R_{out} = 2R_{in}$. The maximum light SED of UW Cen was modeled again (see Figure 4.19). The black dashed line is the same best–fit model as presented earlier, while the red dashed line represents the "thin" shell model. The overall behavior of the SED is recovered with thin shells, especially the location of the local maxima of both IR excesses. Nevertheless, the limitation of this modeling strategy is that it adequately describes neither the region between the maxima nor the SED.

The location for R_{out} of the outer envelope can be calculated from the *Spitzer* or

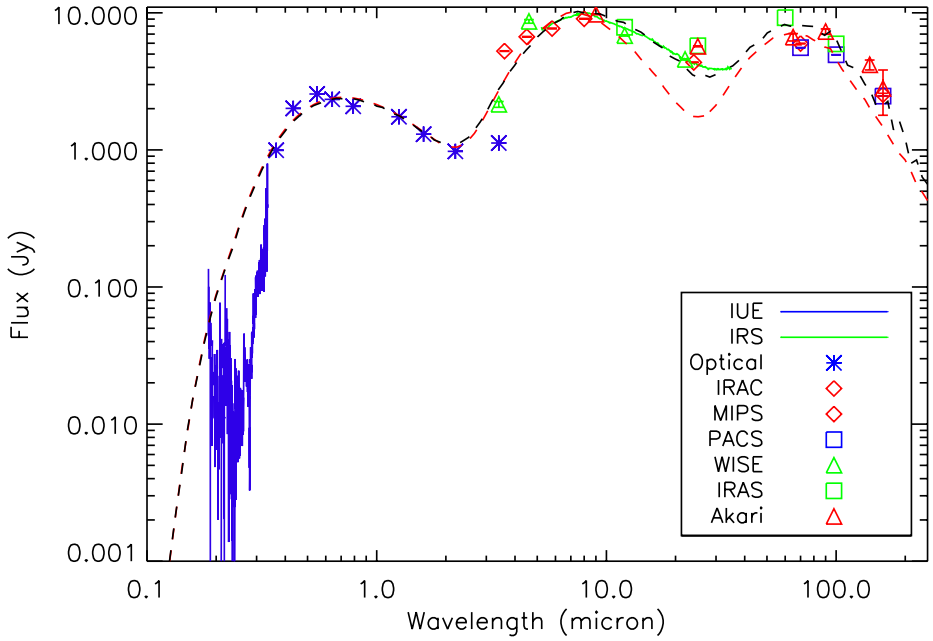

Figure 4.19: The maximum–light SED of UW Cen with the same configuration as Figure 4.17. The sum of the best–fit MOCASSIN models for the central source, warm, and cold dust shells is still represented by the dashed black line. The MOCASSIN fit for thin shells ($R_{out} = 2R_{in}$ is represented by the red dashed line. The need for larger reservoirs of "cold" dust in both the inner and outer envelopes is apparent with the fits to the right of the local maxima being well below the observations.

Herschel observations. This is derived from the angular diameter distance relation (for small angles): $\theta \approx x/d$, where θ is the angular size of the extended object, x is the physical size of the object, and d is the distance to the object. The average ratio of $R_{out-Outer}/R_{out-Measured}$, excluding UW Cen (see below), is 1.30 with minimum and maximum values of 0.68 (V854 Cen) and 3.31(RY Sgr), respectively (see Table 5.1 for the entire sample). $R_{out-Outer}$ is the outer radius of the outer envelope derived from my MCRT modeling, while $R_{out-Measured}$ is the value of the same parameter as calculated from the FIR imaging.

The large differences between the modeled and measured outer radii at the minimum, 30% below the expected size, and maximum, 330% higher than the expected size, are likely due to the uncertainties in the distance to the Galactic RCB stars.When these uncertainties, which are estimated to be up to a factor of 2, are taken into account then the differences between the modeled and calculated values for V854 Cen and RY Sgr become less severe. The uncertainties in my calculated distances are tied to the effective temperatures chosen for my MCRT modeling (Asplund et al., 1997, 2000; De Marco et al., 2002) and that the absolute brightness of my sample RCB stars range between $M_V = -3$ and $M_V = -5$ (Alcock et al., 2001; Tisserand et al., 2009). These assumptions are not independent of each other. A different choice of temperature would lead to a different absolute brightness, estimated distance, and measured outer radius.

UW Cen is the only case that two different outer radii can be calculated because of its reflection nebula, which is observed at optical wavelengths. The diameter of the reflection nebula has been measured at 15″ (Pollacco et al., 1991; Clayton et al., 1999). Clayton et al. (1999) calculated $R_{out-Measured}$ as being 6.00×10^{17} cm assuming a distance of 5.5 kpc (Lawson et al., 1990a). I derived a distance of 3.5 kpc from a higher E(B–V) than Clayton et al. assumed was present for the line of sight to UW Cen. This corresponds to the slightly smaller value of 4.01×10^{17} cm for $R_{out-Measured}$. The value of $R_{out-Measured}$ derived from the FIR observations is 2.62×10^{18} cm.

First, it is important to note that the inner envelope suggested to exist by my MOCASSIN modeling lies entirely within $R_{out-Measured}$ for the reflection nebula. Next, that the two values for $R_{out-Measured}$ roughly correspond to the modeled values for $R_{in,Outer}$ and $R_{out-Outer}$. $R_{in,Outer}$ is 7.00×10^{17} cm, which is larger than my derived value but in good agreement with the Clayton et al. (1999) calculation. This indicates that the outer edge of the reflection nebula possibly represents the beginning of the second envelope containing the large reservoir of cold dust predicted by MCRT. Further, there is an excellent agreement (<5%) between the modeled value of $R_{out-Outer}$ and my calculation of $R_{out-Measured}$ from the FIR observations.

4.8.2 Envelope Masses & Decline Activity

One of the goals of this thesis is to determine the likelihood that these large, diffuse shells could have formed during the RCB phase. Hence, I searched for a relationship between the physical size and dust mass of the inner and outer envelopes and frequency of declines. It is commonly accepted that the declines are caused when a cloud of carbon dust condenses, along our line of sight, near the central RCB star. Over time radiation pressure from the central star acts on the cloud driving it outward into the larger circumstellar environment. Thus, the frequency and/or length of time an RCB star spends near minimum light is evidence for the formation of fresh dust, at least along the line of sight. Long term monitoring at 3.4 μm (L–band) is able to follow the creation of new clouds out of the line of sight (i.e. Feast et al., 1997; Feast, 1997; Bogdanov et al., 2010). It is the outward expansion of these new dust clouds that will eventually construct the observed large envelopes in a scenario that favors dust envelopes formed during the current RCB phase.

Jurcsik (1996) examined how many declines (N_{fades}) have been recorded against how many years (N_{years}) an RCB star has been observed for (see her Table 1). The time, in days, between declines (ΔT_{fades}) is also provided and calculated from N_{fades}/ N_{years}. All seven of the RCB stars in my thesis are in the Jurcsik sample.

The minimum inner envelope mass, as determined from my MOCASSIN modeling, is 7.59×10^{-8} $M_{\odot}$ (MV Sgr) while the maximum is 4.00×10^{-6} $M_{\odot}$ (V CrA). MV Sgr is among the least active RCB stars with ΔT_{fades} quoted at 6900 days from 2 declines in, at the time, 38 years of observations (Jurcsik, 1996). V CrA is among the most active RCB stars with ΔT_{fades} given as 900 days from 16 declines in 39 years (again at the time of publication) (Jurcsik, 1996). V CrA has experienced more declines (see the lower panel in Figure 2.3), while MV Sgr has remained near maximum light (see Figure 2.4) since Jurcisk's publication. This implies that, recently, MV Sgr has

not been forming as much dust as the other RCB stars. This would allow the star, via radiation pressure, to move the dust farther outward to colder temperatures, effectively emptying out the inner envelope

This is reinforced by the dust mass derived to be in the outer shell modeled around MV Sgr, 3.27×10^{-4} $M_{\odot}$. It is comparable in size to the outer envelopes of R CrB (2.42×10^{-4} $M_{\odot}$), RY Sgr (7.25×10^{-4} $M_{\odot}$), and SU Tau (6.80×10^{-4} $M_{\odot}$), which are all extremely more active (see light curves in Chapter 2). The most massive modeled envelope,5.14×10^{-3} $M_{\odot}$, belongs to UW Cen. The mass of UW Cen's inner shell is 2.40×10^{-6} $M_{\odot}$, which is the second largest in my sample. It is among the more active RCB stars in the Jurcsik (1996) sample with 13 declines in 40 years of observations (ΔT_{fades} = 1100 days). It has also experienced at least two deep decline events since Jurcsik (1996) was published (see the bottom panel of Figure 2.2). UW Cen also has the visual reflection nebula that surrounds (diameter $\sim 15''$) (Pollacco et al., 1991; Clayton et al., 1999). The combination of UW Cen's proficient dust production and reflection nebula most likely contribute to the high dust masses from the MCRT modeling.

A peculiar case for establishing whether the envelopes being generated during the current RCB phase is V854 Cen. The dust masses of the inner and outer envelopes are 3.08×10^{-7} $M_{\odot}$ and 2.60×10^{-5} $M_{\odot}$, respectively. These values are the second lowest and lowest for my sample. This seems paradoxical since V854 Cen was in decline for nearly half of a century (McNaught, 1986). It has also been extremely active since its return to maximum light in the 1980s with 9 declines in 9 years of monitoring (ΔT_{fades} = 370 days) (Jurcsik, 1996) and more since then (see the upper panel in Figure 2.3).

One possible resolution for this discrepancy is that the total time each star has been in the RCB phase is unknown (i.e., what are the relative ages of the different RCB stars to each other?). This issue is not able to be resolved by my thesis, but should V854 Cen be younger than the rest of the RCB stars then the derived smaller nature of its envelopes would make sense, even with its near half century decline. Analysis of wind features via the He I λ10830 line (Clayton et al., 2013a), which has been used an indicator of dust expansion velocities (see further below), has found that V854 Cen behaves differently than all other RCB stars. Clayton et al. found times when this feature almost disappeared completely near the end of a decline, which indicates very little wind coming from V854 Cen, and times when the wind was a strong as 700 km s^{-1}. Further underlying all of this is that V854 Cen is also the most H–rich of any RCB star and it is unknown how much this enrichment affects both V854 Cen itself and its CSM.

An important parameter of this analysis is establishing the true expansion velocity of the dust. Estimates for this motion range from tens to hundreds of km s^{-1}. The case for slower moving dust has been attributed to either the natural expansion of a PN shell (Clayton et al., 2011a) or from high resolution (R $\sim$ 30,000), high S/N spectrum of scattered star light during deep declines (García-Hernández et al., 2011b, and references therein). Observations of the He I λ10830 line suggest that the dust is rapidly accelerated up to 400 km s^{-1} (Clayton et al., 1992a, 2003, 2013a).

Therefore dust forming at 2 R_* (170 $R_{\odot}$ or 1.2×10^{13} cm) would take 2 to 20

years to reach 10^{14} to 10^{15} cm, typical values of R_{in} for the inner shell from my RT modeling, at 20 km s^{-1}, respectively. Dust moving at higher implied velocities would cover the same distances in 3 to 9 months. These timescales are much shorter than the lower limit on the lifetime of an RCB star: ∼200 years from R CrB (Pigott & Englefield, 1797). This seems to indicate that at least the inner envelopes are entirely able to be constructed from dust ejected during the RCB phase.

The critical issue to resolve is whether or not the continued outward expansion of this dust is also responsible for the observed cold envelopes. Dust moving at 400 km s^{-1} would take about 10^3 to 10^4 years to reach anywhere from 10^{18} cm to 10^{19} cm, respectively. It would take an order of magnitude longer for dust moving at 20 km s^{-1} to reach those same distances. The slower dust expansion has also led Rao & Nandy (1986) to put forth that these envelopes could be remnant material from the initial red giant phase of these stars.

Getting dust to these locations is not a problem since it is just the passage of time and the dust has already been observed to be at these locations. A major concern is whether or not enough material can accumulate to the observed levels. Evidence for material moving with different velocities has been observed very near the central stars in the case of R CrB and UW Cen (Clayton et al., 2011a). Cometary–like features, which are also observed in PNe, were discovered to exist near the central stars and point to material moving with multiple velocities.

4.8.3 Comparison to an HdC Star & FF Object

The FF object, V605 Aql, experienced an event in the early 20th century that took it from below the limits of photographic plates (m = 15) all the way up to a peak magnitude of 10.2 in 1919 (Wolf, 1920). Woods (1921) found that the rise to its maximum brightness was a slow climb over the preceding two years. The languid nature of this outburst originally earned V605 Aql a classification as a slow nova (Lundmark, 1921). V605 Aql did not spend a significant time at its peak brightness. It began to fade quickly and within a year had fallen below 15th magnitude only to return in 1921, before ultimately fading for good in 1923 (Clayton & De Marco, 1997; Clayton et al., 2006, 2013b).

During V605 Aql's 1921 re-brightening spectra were acquired at the 0.91–m Crossley telescope (Lick Observatory) with both the small (Keeler) and large (Wright) quartz spectrographs (Lundmark, 1921). Lundmark discovered that the spectra pointed to V605 Aql as a cool carbon (R0) star and not a classical nova in the late stages of an outburst. This was the last major study of V605 Aql for nearly 50 years. Deep observations obtained independently and published simultaneously by Ford (1971) and van den Bergh (1971) revealed that V605 Aql sat the center of the old PN Abell 58 (Abell, 1966). Further, re-analysis of the Lundmark (1921) spectra confirmed the spectral type and found that V605 Aql was hydrogen–deficient (Bidelman, 1973).

Table 4.8: V605 Aql Photometry

Band	Flux (Jy)	σ (Jy)
J (1.25)	3.21e-05	1.50e-05
H (1.60)	2.27e-04	3.00e-05
K (2.20)	8.56e-04	8.00e-05
WISE/3.4	1.44e-02	3.05e-04
WISE/4.6	1.13e-01	2.07e-03
AKARI/9	2.85e+00	1.68e-02
IRAS/12	4.99e+00	2.00e-01
WISE/12	8.56e+00	5.52e-02
AKARI/18	1.53e+01	1.20e-01
WISE/22	2.22e+01	1.02e-01
MIPS/24	1.57e+01	8.01e-02
IRAS/25	2.95e+01	1.18e+00
IRAS/60	4.07e+01	4.10e+00
AKARI/65	2.67e+01	2.50e+00
MIPS/70	1.78e+01	1.85e-01
AKARI/90	2.08e+01	9.87e-01
IRAS/100	1.83e+01	2.00e+00
MIPS/160	2.82e+00	1.12e-01

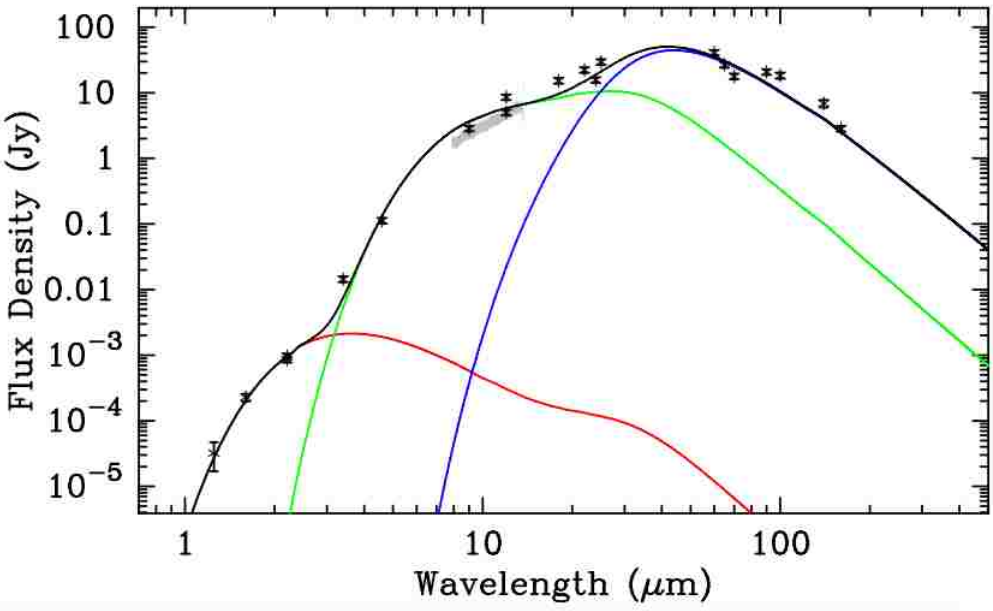

Figure 4.20: The V605 Aql SED presented by Clayton et al. (2013b). The black symbols represent photometry from ground–based JHK (Hinkle et al., 2008), WISE, AKARI, IRAS, and *Spitzer*/MIPS. The gray line is a spectrum observed with the MID–infrared Interferometric instrument (MIDI) at the Very Large Telescope Interferometer (VLTI). The photometry presented by Clayton et al. are provided Table 4.9. The red, green, and blue lines are individual fits using the emission curves of amorphous carbon dust with temperatures of 810 K, 235 K, and 75 K, respectively. The black line is the sum of the three fits.

Clayton et al. (2013b) presented the modern SED of V605 Aql, which is presented here in Figure 4.20. The SED was made from ground–based NIR photometry (Hinkle et al., 2001), ground–based MIR spectroscopy, and IR photometry from several satellites. Optical photometry is not available due to obscuration by the material ejected during the 1919 outburst. In addition to this obscuring dust, a large reservoir of cold dust associated with V605 Aql is immediately apparent since the SED continues to rise to a maximum around 40 μm.

The SED was fit with emission curves of amorphous carbon dust with temperatures and masses of: 810 K, 1.0×10^{-11}M$_{\odot}$; 235K, 9.0×10^{-6}M$_{\odot}$; 75 K, 2.0×10^{-3}M$_{\odot}$ (Clayton et al., 2013b). These temperatures are in agreement with dust temperatures found in either the first or second envelope of my MCRT for RCB stars. The dust masses calculated by Clayton et al. from the second and third emission curves correspond with those derived for the inner and outer shells, respectively, of my RCB sample. However, the evolution of V605 Aql, itself, has been too rapid when compared to RCB stars. Clayton & De Marco (1997) commented that in 1921 the spectrum of V605 Aql resembled a cool RCB star with $T_{eff} \simeq 5000$ K. However, it has not remained at this low temperature. Optical spectra obtained in 2001 revealed the presence of C IV emission, which indicate that V605 Aql has evolved horizontally back across the HR diagram to an object with $T_{eff} \sim 95,000$ K (Clayton et al., 2006).

That is an evolution of 90,000 K in only 80 years, which is a temperature gain not seen in any RCB stars including the hot RCB stars.

HD 173409 is not an RCB star in the traditional sense, but designated as a hydrogen–deficient carbon (HdC) star. These stars are spectroscopically similar to RCB stars, but have neither the characteristic declines in brightness nor display any evidence for IR excess (Warner, 1967; Goswami et al., 2010; Tisserand, 2012). The spectrum of HD 173409 was first noted as being different from the majority of other stars by Pickering & Fleming (1896) and identified as being hydrogen–deficient by Bidelman (1953). The HdC stars are also known to have an overabundance of ^{18}O (Clayton et al., 2005, 2007; García-Hernández et al., 2010), however the effective temperature of HD 173409 is too hot for molecular bands to be detected in its spectrum.

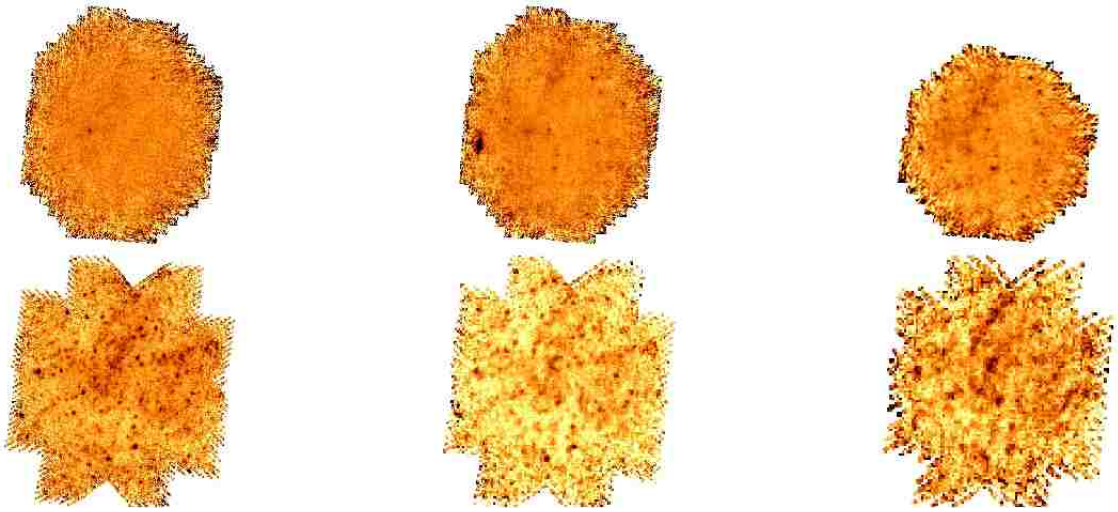

Figure 4.21: Top row: *Herschel*/PACS observations of HD 173409 at 70, 100, and 160 μm, respectively. The 70 and 100 μm fields are both $9' \times 11'$, while the 160 μm field is $9' \times 9'$. Bottom row: *Herschel*/SPIRE observations of HD 173409 at 250, 350, and 500 μm, respectively. The fields are all $20' \times 20'$. The lack of a point source or any nebulosity centered on the position of HD 173409 is consistent with HdC stars having no IR excess.

HD 173409 was included in the *Herschel* observing campaign by G. Clayton to learn if any cold dust could be surrounding the central star that would have gone previously undetected. This is an excellent test to determine if HdC stars are, in fact, RCB stars that either are in an extended period of low decline activity or oriented in such a way that dust clouds do not condense along our line of sight. The *Herschel* PACS and SPIRE observations of HD 173409 can be seen in Figure 4.21. The image colors are inverted so that positive flux detections are black and oriented such that North is up and East is left. No discernible material associated with HD 173409 is found at these wavelengths.

Table 4.9: HD 173409 Photometry

Band	Flux (Jy)	σ (Jy)
U (0.365)	0.095	0.002
B (0.433)	0.324	0.006
V (0.550)	0.626	0.012
$R_{\rm C}$ (0.640)	0.733	0.014
$I_{\rm C}$ (0.790)	0.770	0.014
2MASS/J (1.24)	0.698	0.017
J (1.25)	0.739	0.020
H (1.60)	0.531	0.015
2MASS/H (1.66)	0.475	0.020
2MASS/$K_{\rm S}$ (2.16)	0.354	0.012
K (2.20)	0.356	0.010
L (3.40)	0.190	0.009
WISE/3.4	0.185	0.004
WISE/4.6	0.102	0.002
WISE/12	0.020	0.0004
WISE/25	0.004	0.001
PACS/70	7.06e-05	Upper Limit
PACS/100	1.47e-04	Upper Limit
PACS/160	1.48e-04	Upper Limit
SPIRE/250	0.113	Upper Limit
SPIRE/350	0.001	Upper Limit
SPIRE/500	0.002	Upper Limit

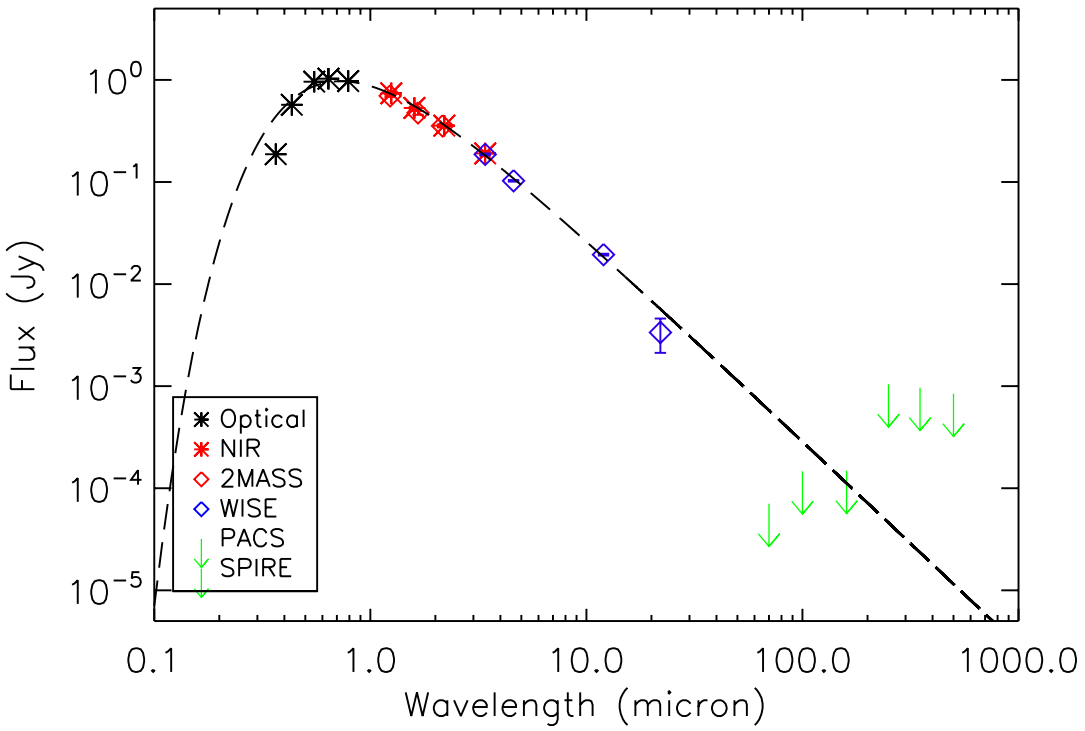

Figure 4.22: The HD 173409 SED. Black asterisks: $UBVR_{\rm C}I_{\rm C}$; red asterisks: $JHKL$; open blue diamonds: WISE (3.4, 4.6, 12.0, 22.0 μm); green arrows: *Herschel* PACS and SPIRE 3σ upper limits.

HD 173409 was in the Tisserand (2012) sample, which examined the early data release by the WISE science team. No excess was found in the NIR/MIR from the WISE observations. I have constructed the HD 173409 SED from archival photometry and photometry from the ALLWISE catalog (see Chapter 2). Additionally, 3σ upper limits were determined for these observations using a $30''$–diameter aperture centered on the position of HD 173409. These upper limits were then included in the HD 173409 SED, which can be found in Figure 4.21 with a 7000K blackbody overplotted. The photometry that has gone into the HD 173409 SED can be found in Table 4.10. The SED reinforces that there is no detectable dust surrounding this HdC star.

However, the HdC star HD 175893 was discovered to have an IR excess from WISE photometry (Tisserand, 2012).Tisserand established an 8 tiered system of progressive criteria that needed to be satisfied by a candidate RCB star. HD 173409 did not meet them as it was disqualified by having a WISE color of $[4.6]-[12]<0.75$, while HD 175893 passed all of them (Tisserand, 2012). This means that HD 175893 could represent a type of missing link between HdC and RCB stars, or be a clear example of an RCB star in a phase of low activity in terms of dust production (Tisserand, 2012).

4.9 MCRT Model Summary

Observations with *Spitzer* and *Herschel* have revealed either extraordinary features or the the presence of large reservoirs of cold dust around several RCB stars in this sample. Highlighting the individual findings:

MV Sgr – The only hot RCB star in my sample. MV Sgr is thought to have a still ionized PN from spectroscopy, which reveals strong Hα as well as nebular emission lines (De Marco et al., 2002). The *Spitzer* imaging reveals the existence of dust emission out to 70 μm. This improved the coverage in the FIR for the MV Sgr SED and improves the robustness of my MOCASSIN modeling, since AKARI and IRAS have conflicting views in this regime. The presence of colder material has been suggested before by García-Hernández et al. (2011b, 2013). They were, however, limited by the longest wavelength of the *Spitzer*/IRS observations (about 40 μm) used in their analysis.

R CrB – New imaging and SED modeling of R CrB was presented previously by Clayton et al. (2011a). I have added *Herschel*/PACS observations of R CrB and its diffuse shell. These observations support previous FIR imaging, which finds that the envelope appears spherical (Clayton et al., 2011a, and references therein). The MCRT modeling of the maximum–light SED with MOCASSIN was best–fit by a two shell model with 2.42×10^{-4} M$_{\odot}$ of dust in the outer shell. This is two orders of magnitude lower than Clayton et al. (2011a) found with their own modeling.

RY Sgr – FIR and sub-mm images show the existence of a strong dust envelope that is reliably detected out to 500 μm. The modeling of the RY Sgr SED finds a large amount,7.25×10^{-4} M$_{\odot}$, of cold dust in the RY Sgr CSM. This is the second most massive shell in my sample, and could be constructed by multiple dust formation events.

SU Tau – The bow shock associated with SU Tau was a completely unexpected discovery and only possible thanks to the high angular resolution provided by *Herschel*. The association with SU Tau and not being background or foreground dust is best seen in 3–color *Herschel* imaging. MOCASSIN modeling of the SU Tau SED suggests that the CSM contains a high amount of cold dust, 6.80×10^{-4} M$_{\odot}$, which is the third highest mass in the sample. The SED modeling did not include contributions from the bow shock.

UW Cen – The reflection nebula surrounding UW Cen has been known about for 25 years (Pollacco et al., 1991). However, a more full picture of UW Cen's CSM has been achieved with the *Spitzer* and *Herschel* observations. The higher angular resolution with *Herschel* reveals diffuse nebulosity outside of the boundaries set by the reflection nebula. The UW Cen SED shows a distinct second peak in the FIR, which is unique among the stars in my sample and possibly all RCB stars. The MCRT modeling finds that there is 5.14×10^{-3} M$_{\odot}$, which makes this the most massive envelope in my sample.

V854 Cen – A bizarre member of an already bizarre group of stars. *Spitzer*/MIPS observations are the best available in the FIR as V854 Cen was not observed with *Herschel*. A large amount of cold dust surrounding V854 Cen is indicated since the 24 and 70 μm images are essentially the MIPS PSFs at these wavelengths. A well defined

extended source is also seen at 160 μm. The MC RT modeling with MOCASSIN of the V854 Cen SED finds that there is 2.85×10^{-5} $M_{\odot}$ in a suggested outer spherical envelope.

V CrA – This RCB star is also one of four to have been observed with both *Spitzer* and *Herschel*. The *Spitzer* observations show very weak dust emission at 70 and 160 μm (the 24 μm is the MIPS PSF at this wavelength, which is consistent for all the stars in this sample). The higher angular resolution provided by *Herschel* does not improve on the *Spitzer* findings. A simple point source or unresolved extended source appears at the PACS wavelengths, and no material is seen at SPIRE wavelengths. SED modeling also suggests a low mass, low density diffuse envelope.

The results of the MOCASSIN RT modeling found that all of the RCB stars were best described by two extended, separated envelopes. This is in agreement with prior modeling by Nagendra & Leung (1996), who found that they could only fit the R CrB SED if the ISRF was artificially increased above its expected levels. The sizes of the inner and outer envelopes were also examined in the context of the expansion velocity of dust generated during the RCB phase. If the dust moves with a velocity of 20 – 30 km s^{-1} (García-Hernández et al., 2011b, and references therein), then these envelopes would take over 10^5 years to construct. If the dust moves at 400 km $s^{-}1$ (Clayton et al., 1992a, 2003, 2013a), then the time lowers to 10^4 years. Each of these times is much longer than the lifetime of RCB stars, which is unknown but is at least >200 years (Pigott & Englefield, 1797). The inner envelopes are most likely constructed during the RCB phase regardless of the speed of the dust.

The derived dust masses were also compared with objects that appear to be spectroscopically similar to RCB stars, namely HdC stars and final flash objects. The HdC star HD 173409 was found to be well described by simply a 7000K blackbody representing the star with no IR excess. An upper limit for the dust mass from our RT modeling is on the order of 10^{-10} $M_{\odot}$. However, another HdC star, HD 175893 was discovered to be surrounded by a warm, diffuse shell from WISE observations (Tisserand, 2012). The final flash object V605 Aql was estimated by Clayton et al. (2013b) to have a shell that might contain up to 10^{-3} $M_{\odot}$ of cold (75 K) dust. This is on par with the derived dust masses from my MCRT. However, V605 Aql has already been observed to go from a star with a spectrum like a 5000 K RCB star to star with a temperature of 95000 K (Clayton et al., 2006). No RCB star has ever been observed to evolve as rapidly as V605 Aql.

5. Discussion & Conclusions

The goals of my thesis project were to better characterize the dusty, diffuse nebulosity surrounding a sample of R Coronae Borealis (RCB) stars and to determine the HI abundance of the envelope known to surround R Coronae Borealis, itself. Three possible interpretations have been explored in order to explain the origin of these envelopes: (1) they are fossil planetary nebulae (PNe); (2) they are remnant material from the merger of a CO and a He white dwarf binary, (3) they have been constructed from dust ejection events during the current RCB phase. My sample of RCB stars included: the hot RCB star ($T_{eff} > 15{,}000$ K) MV Sagittarii (MV Sgr); and the warm (6,000 K $< T_{eff} <$ 7,500 K) RCB stars R Coronae Borealis (R CrB), RY Sagittarii (RY Sgr), SU Tauri (SU Tau), UW Centauri (UW Cen), V854 Centauri (V854 Cen), and V Coronae Australis (V CrA).

I performed an investigation into the origin of the R CrB envelope in the context of the three scenarios presented above. The large, diffuse dust envelope surrounding R CrB has been known about since the IRAS mission (Walker, 1985; Gillett et al., 1986). Gillett et al. (1986) was the first to undertake an in–depth analysis of this shell in the context that the shell was a fossil remnant from an earlier PN stage. This conclusion for its origin would make the nebulosity hydrogen rich (H–rich). Mass estimates of this envelope based of the projected physical size (r $\sim$ 4 pc) and dust mass (10^{-2} $M_{\odot}$) suggested a total mass of 1–2 $M_{\odot}$ (Gillett et al., 1986; Clayton et al., 2011a). In this case, R CrB has been in its RCB phase for at least 10^5 years (Clayton et al., 2011a).

The fossil nature of the shell means that any hydrogen present in the shell should have recombined and now be emitting in the radio regime. Archival L–band (λ = 21-cm) observations containing R CrB were acquired from the GALFA-HI survey (Peek et al., 2011). The analysis of these data yielded no detection of H I emission associated with the extended shell. A 3σ upper limit of 0.3 $M_{\odot}$ was placed for any H I present with the data, which does not entirely rule out that the shell could have been a low mass PN. Further, comparisons to NGC 6781, an active and large PN (Ueta et al., 2014), suggested a gas-to-dust ratio closer to 200 instead of the typical Galactic value of 100. If the gas-to-dust behaves similarly in the R CrB envelope then there would be $\lesssim 10^{-3}$ $M_{\odot}$ of dust in the envelope.

If the R CrB envelope formed from either remnant material after a WD merger or during the current RCB phase, then the gas within the envelope would be H–poor and He–rich. The results from fully three-dimensional hydrodynamics code with adaptive mesh refinement (AMR) (Marcello et al. 2016, in prep) indicate that $\sim 10^{-2}$ $M_{\odot}$ of

gas escapes the merger to contribute to forming an extended shell. This material would be expanding with velocities 600–900 km s^{-1} and take $\sim 10^4$ yr to expand to the size of the R CrB shell. However, since this gas is 95% He, a maximum of 5% is left that could act a site for dust to form. If a typical gas-to-dust ratio, 100 (Whittet, 2003), is assumed then $M_{Dust} \leq 10^{-6}$ $M_{\odot}$ could form in such a shell. This is much, much lower than the dust mass derived by Clayton et al. (2011a).

Calculations for the amount of dust that can be produced during the RCB phase were performed with the assumption that the average puff that forms around an RCB star has a dust mass of $\sim 10^{-8}$ $M_{\odot}$ (Clayton et al., 1992a, 2011a). Thus, if a dust puff were to form somewhere around R CrB every 50 days then $\sim 10^{-7}$ $M_{\odot}$ of dust will form per year around the star. When this is combined with evidence, provided from observations following He I λ10830, that the dust is rapidly accelerated up to $\sim$400 km s^{-1} (Clayton et al., 1992a, 2003, 2013a) then dust produced during the RCB phase could fill the R CrB shell in only $\sim 10^4$ yr. In this time, R CrB will have produced at least 10^{-3} $M_{\odot}$.

I have increased the number of RCB stars that have had their maximum–light spectral energy distributions (SEDs) modeled by Monte Carlo Radiative Transfer (MCRT). The results of my MOCASSIN models are presented in Table 5.1. The name of the star is given in column 1. The inner radius (R_{in}) in centimeters, outer radius (R_{out}) in centimeters, and dust mass (M_{Dust}) in solar masses are presented in columns 2–4, respectively. These columns are further subdivided where the modeled inner and outer envelope are given in the first and second rows of each cell, respectively. The outer radius of the outer envelope ($R_{out-Measured}$), as calculated from the angular diameter distance formula, in centimeters is found in column 5.

The MCRT modeling of these SEDs suggests the existence of two discrete, concentric spherical shells around each of my sample RCB stars. Some polarization observations imply that the mass loss experienced by RCB stars is bipolar (Clayton et al., 1997). However, this is not supported by the analysis of high angular resolution and high sensitivity far infrared (FIR) and submillimeter (sub–mm) observations, which shows that the dust shells are spherical. Regardless, it is these outer envelopes that are of particular interest as they are the structures that need to be examined in the context of the three origin scenarios presented above.

It is unlikely that any of these extended outer shells are the remnant material of a WD merger. They have a mean mass of 1.02×10^{-3} $M_{\odot}$, which is much greater than the value predicted ($M_{Dust} \leq 10^{-6}$ $M_{\odot}$) by this origin scenario. Even when this average is adjusted for UW Cen, which MOCASSIN modeling suggests that 5.14×10^{-3} $M_{\odot}$ may be present in this envelope alone, the mean mass for the outer envelopes remains 3.43×10^{-4} $M_{\odot}$. Further, the least massive envelope (V854 Cen) is implied to contain 2.60×10^{-5} $M_{\odot}$ of dust. This is still an order of magnitude higher than predicted for a WD merger.

The construction of these shells during the current RCB phase is critically tied to the number of dust puffs produced, the expansion velocity of the dust puffs, and the lifetime of RCB stars. The number of puffs produced can be approximated by the time between declines (see Figure 5.1), which has been found to range from 370 to 36,000 days (Jurcsik, 1996), and the analysis of the NIR flux of the warmer inner

Table 5.1: Derived MOCASSIN Properties and Measured Outer Radii

Star	R_{in} (cm)	R_{out} (cm)	M_{Dust} ($M_\odot$)	$R_{out-Measured}$ (cm)
MV Sgr	3.25×10^{14}	9.45×10^{15}	7.59×10^{-8}	1.03×10^{18}
	3.25×10^{16}	9.45×10^{17}	3.27×10^{-4}	
R CrB	1.00×10^{15}	3.00×10^{16}	9.09×10^{-7}	1.23×10^{19}
	3.40×10^{17}	1.00×10^{19}	2.42×10^{-4}	
RY Sgr	8.62×10^{14}	2.50×10^{16}	8.90×10^{-7}	1.36×10^{18}
	5.15×10^{17}	4.50×10^{18}	7.25×10^{-4}	
SU Tau	2.10×10^{15}	4.25×10^{16}	2.27×10^{-6}	6.91×10^{18}
	1.00×10^{18}	9.00×10^{18}	6.80×10^{-4}	
UW Cen	1.55×10^{15}	4.50×10^{16}	2.40×10^{-6}	4.01×10^{17}
	7.00×10^{17}	2.50×10^{18}	5.14×10^{-3}	2.62×10^{18}
V854 Cen	4.90×10^{14}	1.00×10^{16}	3.08×10^{-7}	1.48×10^{18}
	3.45×10^{16}	1.00×10^{18}	2.60×10^{-5}	
V CrA	1.70×10^{15}	4.90×10^{16}	4.00×10^{-6}	1.39×10^{18}
	1.00×10^{17}	1.00×10^{18}	5.90×10^{-5}	

envelope (Feast et al., 1997; Feast, 1997; García-Hernández et al., 2011b; Rao & Lambert, 2015). These track the recent mass loss history.

The velocity of the expanding dust has been estimated as being tens to hundreds of km s^{-1}. Slower expansion velocities have been suggested by (García-Hernández et al., 2011b, and references therein). Faster outward movement is suggested by the He I λ10830 line, which suggests that the dust is rapidly accelerated up to 400 km s^{-1} (Clayton et al., 1992a, 2003, 2013a). The outer envelopes in my sample have implied outer radii that range from 10^{18} cm to 10^{19} cm (see Table 5.1). Material at these distances represents the oldest material to be shed by RCB stars. Dust moving with slower velocities, 20 km s^{-1}, would take about 10^4 to 10^5 years to reach anywhere from 10^{18} cm to 10^{19} cm, respectively. These times drop by an order of magnitude if the dust velocities agree more with the results of the He I λ10830 analysis. These timescales are both much longer than we have known about the RCB phenomenon (Pigott & Englefield, 1797).

A knowledge of the hydrogen abundance in these shells would help determine whether they are fossil PN shells or not. If the envelopes are fossil PNe then they should be H–rich. There are no observations of the H I abundance in any RCB shells other than R CrB, itself. Thus, the classification of the extended, dust envelopes around the other RCB stars in my sample as fossil PN shells cannot be ruled out at this time.

This circumstellar material (CSM) is a direct representation of the mass loss history experienced by RCB stars. An unexpected and interesting result of the MCRT modeling is that two discrete, thick shells are needed to fit the observed SEDs of all the RCB stars in the sample. If the mass loss experienced by RCB stars is continuous

as indicated by long term NIR monitoring (e.g., Feast et al., 1997), then one would expect that the SEDs could be described by a single large, extended envelope. This does not seem to be the case. Moreover, it seems to suggest that at some point dust formation ceased and then restarted, or that the inner and outer shells have different origins. For example, the inner shell could be from the RCB phase and the outer shell could be a fossil PN shell. It is critical to mention, again, that the lifetime of the RCB phase is unknown and that the implied ages of these structures, 10^4 to 10^5 years, are much older than the coverage of the NIR monitoring.

Potentially, an improved understanding of the IR shells of the RCB stars will help to distinguish between their suggested progenitors. Two scenarios have been proposed to explain the origins of RCB stars. One scenario states that RCB stars are the product of the merger of a white dwarf (WD) binary (Webbink, 1984; Saio & Jeffery, 2002). This would make RCB stars the byproduct of the same processes that possibly produce Type Ia supernovae at higher masses. The second scenario suggests RCB stars occur after a single WD experiences an outburst that temporarily restores it to being a cool giant (Fujimoto, 1977; Renzini, 1979; Iben et al., 1996).

I have compared the observations of the RCB stars to the hydrogen–deficient carbon (HdC) stars and stars that have been observed to undergo a final flash. HdC stars are essentially spectroscopic twins of RCB stars. HdC stars, however, do not experience decline events and lack any IR excess. The HdC star, HD 173409, was observed with both PACS and SPIRE on *Herschel*. No emission associated with HD 173409 was detected in any of the *Herschel* observations. The SED for this star also shows no evidence for any IR excess when fit by a single 7000 K blackbody. Recently, one HdC star, HD 175893, was found to have an IR excess from analysis of WISE colors and could either represent a missing link between the two classes of objects or an RCB star going through an extended period of low dust formation (Tisserand, 2012).

V605 Aql was observed to undergo an outburst in 1919 that was later classified as a FF object (Clayton et al., 2013b, and references therein). V605 Aql lies near the center of the planetary nebula (PN) Abell 58 (Ford, 1971; van den Bergh, 1971). Clayton et al. (2013b) presented the SED for V605 Aql, which indicated the presence of $\sim 10^{-3}$ $M_{\odot}$ of dust in the 1919 ejecta. This is on a similar level to the dust masses derived from my MOCASSIN modeling for the outer shells. Additionally, V605 Aql was found to be spectroscopically similar to an RCB star with $T_{eff} \simeq 5000$ K. The star has since then undergone rapid evolution back to an object with $T_{eff} = 95{,}000$ K (Clayton et al., 2006). No RCB star has been observed to have a similar change in temperature in under a century.

My thesis has presented a considerable amount of new information about RCB stars and the diffuse shells known to surround them especially at wavelengths between 70 and 500 μm. The improvements in this regime provided by *Spitzer* and *Herschel* have revealed a wealth of new information about the cold, extended envelopes both in terms of their morphology and the amount of cold dust. The *Herschel* observations of SU Tau with the PACS and SPIRE instruments have led to the discovery of a bow shock like structure. This is the first known RCB star to exhibit this type of feature, which represents interactions between the SU Tau CSM and the local interstellar

medium (ISM). The bow shock extends between 30″ to 50″ from the central position of SU Tau with a brighter feature in the southeast possibly indicating a location where more material is beginning to pile up.

Although these findings have come only for a small sample of well studied RCB stars. I would like to extend my thesis work to survey all known Galactic and in the Magellanic Clouds (MCs) RCB stars at these wavelengths with facilities such as the Atacama Large Millimeter Array, Stratospheric Observatory for Infrared Astronomy (SOFIA), or the Submillimeter Array (SMA). We will be able to better determine the behavior of their SEDs and by extension the cold dust that may (or may not) be present, as our instrumentation continues to improve in both sensitivity and angular resolution. Further, the improvements in angular resolution will reveal new insights into the interactions between the CSM of RCB stars and the ISM such as in the case of SU Tau.

I have also provided the first constraints on the hydrogen abundance for any cold, dust nebulosity surrounding any RCB star. While my derived upper limit is lower than those predicted earlier for R CrB, it is still not low enough to rule out whether or not the shell was once small PN. I have acquired new L-band observations of the field containing R CrB with the 100–m Robert C. Byrd Green Bank Telescope in Green Bank, WV. These observations were completed at the beginning of May 2016 and await reduction, analysis, and eventual publication. They should be able to lower the mass limit for any H I, if present, to < 0.1 $M_{\odot}$, which will greatly limit the probability that this envelope is a fossil PN. I would like to extend 21–cm observations to as many of the Galactic RCB stars as possible to determine if any of the envelopes have the possibility of being fossilized PNe.

RCB stars are among the most uncommon and bizarre objects discovered in the Universe. However, they provide the opportunity to greatly advance our knowledge in areas such as stellar evolution and stellar chemistry. We have only nascently entered into an era where both observations and theory can begin to answer many of the long standing questions about RCB stars. The continued study of RCB stars in the 21st century should even be able to finally address what the proper progenitors of RCB stars are.

Bibliography

Abell, G. O. 1966, ApJ, 144, 259

Alcock, C., et al. 2001, ApJ, 554, 298

Asplund, M., Gustafsson, B., Kameswara Rao, N., & Lambert, D. L. 1998, A&A, 332, 651

Asplund, M., Gustafsson, B., Kiselman, D., & Eriksson, K. 1997, A&A, 318, 521

Asplund, M., Gustafsson, B., Lambert, D. L., & Rao, N. K. 2000, A&A, 353, 287

Asplund, M., Lambert, D. L., Kipper, T., Pollacco, D., & Shetrone, M. D. 1999, A&A, 343, 507

Barnard, F. A. P. 1916, Harvard College Observatory Bulletin, 617, 1

Bergeron, P., Gianninas, A., & Boudreault, S. 2007, in A. S. P. Conf. Ser., Vol. 372, 15th European Workshop on White Dwarfs, ed. R. Napiwotzki & M. R. Burleigh, 29

Bertin, E., & Arnouts, S. 1996, A & AS, 117, 393

Bidelman, W. P. 1953, ApJ, 117, 25

Bidelman, W. P. 1973, in BAAS, Vol. 5, Bulletin of the American Astronomical Society, 442

Boffi, F. R., & Stanghellini, L. 1994, A&A, 284, 248

Bogdanov, M. B., Taranova, O. G., & Shenavrin, V. I. 2010, Astronomy Reports, 54, 620

Bright, S. N., Chesneau, O., Clayton, G. C., de Marco, O., Leão, I. C., Nordhaus, J., & Gallagher, J. S. 2011, MNRAS, 414, 1195

Cameron, A. G. W., & Fowler, W. A. 1971, ApJ, 164, 111

Campbell, L., & Jacchia, L. 1946, The Story of Variable Stars (Blakiston, MA: Harvard Monographs)

Cannon, A. J., & Pickering, E. C. 1908, Harvard College Observatory Circular, 140, 1

Clayton, G. C. 1996, PASP, 108, 225

—. 2012, Journal of the American Association of Variable Star Observers (JAAVSO), 40, 539

Clayton, G. C., Bjorkman, K. S., Nordsieck, K. H., Zellner, N. E. B., & Schulte-Ladbeck, R. E. 1997, ApJ, 476, 870

Clayton, G. C., & De Marco, O. 1997, AJ, 114, 2679

Clayton, G. C., Geballe, T. R., & Bianchi, L. 2003, ApJ, 595, 412

Clayton, G. C., Geballe, T. R., Herwig, F., Fryer, C., & Asplund, M. 2007, ApJ, 662, 1220

Clayton, G. C., Geballe, T. R., & Zhang, W. 2013a, AJ, 146, 23

Clayton, G. C., Herwig, F., Geballe, T. R., Asplund, M., Tenenbaum, E. D., Engelbracht, C. W., & Gordon, K. D. 2005, ApJL, 623, L141

Clayton, G. C., Kerber, F., Gordon, K. D., Lawson, W. A., Wolff, M. J., Pollacco, D. L., & Furlan, E. 1999, ApJL, 517, L143

Clayton, G. C., Kerber, F., Pirzkal, N., De Marco, O., Crowther, P. A., & Fedrow, J. M. 2006, ApJL, 646, L69

Clayton, G. C., Whitney, B. A., Stanford, S. A., & Drilling, J. S. 1992a, ApJ, 397, 652

Clayton, G. C., Whitney, B. A., Stanford, S. A., Drilling, J. S., & Judge, P. G. 1992b, ApJL, 384, L19

Clayton, G. C., et al. 2011a, ApJ, 743, 44

—. 2011b, AJ, 142, 54

—. 2013b, ApJ, 771, 130

Cohen, M., Wheaton, W. A., & Megeath, S. T. 2003, AJ, 126, 1090

Cox, N. L. J., et al. 2012, A&A, 537, A35

Crause, L. A., Lawson, W. A., & Henden, A. A. 2007, MNRAS, 375, 301

Cutri, R. M. 2014, VizieR Online Data Catalog, 2328

Cutri, R. M., et al. 2003, 2MASS All Sky Catalog of point sources.

—. 2012, Explanatory Supplement to the WISE All-Sky Data Release Products, Tech. rep.

De Marco, O., Clayton, G. C., Herwig, F., Pollacco, D. L., Clark, J. S., & Kilkenny, D. 2002, AJ, 123, 3387

Decin, L., et al. 2012, A&A, 548, A113

Dickey, J. M., & Lockman, F. J. 1990, ARA&A, 28, 215

Diolaiti, E., Bendinelli, O., Bonaccini, D., Close, L., Currie, D., & Parmeggiani, G. 2000a, in Astronomical Society of the Pacific Conference Series, Vol. 216, Astronomical Data Analysis Software and Systems IX, ed. N. Manset, C. Veillet, & D. Crabtree, 623

Diolaiti, E., Bendinelli, O., Bonaccini, D., Close, L. M., Currie, D. G., & Parmeggiani, G. 2000b, in SPIE, Vol. 4007, Adaptive Optical Systems Technology, ed. P. L. Wizinowich, 879–888

Drilling, J. S., Schonberner, D., Heber, U., & Lynas-Gray, A. E. 1984, ApJ, 278, 224

Engelbracht, C. W., et al. 2007, PASP, 119, 994

Ercolano, B., Barlow, M. J., & Storey, P. J. 2005, MNRAS, 362, 1038

Ercolano, B., Barlow, M. J., Storey, P. J., & Liu, X.-W. 2003, MNRAS, 340, 1136

Ercolano, B., Young, P. R., Drake, J. J., & Raymond, J. C. 2008, ApJS, 175, 534

Even, W., & Tohline, J. E. 2009, ApJS, 184, 248

Fazio, G. G., et al. 2004, ApJS, 154, 10

Feast, M. W. 1986, IAU Colloq. 87, 128, p. 151

—. 1997, MNRAS, 285, 339

Feast, M. W., Carter, B. S., Roberts, G., Marang, F., & Catchpole, R. M. 1997, MNRAS, 285, 317

Fernie, J. D., & Lawson, W. A. 1993, MNRAS, 265, 899

Ford, H. C. 1971, ApJ, 170, 547

Fujimoto, M. Y. 1977, PASJ, 29, 331

Gaposchkin, S. 1952, Annals of Harvard College Observatory, 115, 61

García-Hernández, D. A., Hinkle, K. H., Lambert, D. L., & Eriksson, K. 2009, ApJ, 696, 1733

García-Hernández, D. A., Kameswara Rao, N., & Lambert, D. L. 2011a, ApJ, 729, 126

—. 2011b, ApJ, 739, 37

—. 2012, ApJL, 759, L21

García-Hernández, D. A., Lambert, D. L., Kameswara Rao, N., Hinkle, K. H., & Eriksson, K. 2010, ApJ, 714, 144

García-Hernández, D. A., Rao, N. K., & Lambert, D. L. 2013, ApJ, 773, 107

Geballe, T. R., Evans, A., Smalley, B., Tyne, V. H., & Eyres, S. P. S. 2002, Ap&SS, 279, 39

Gillett, F. C., Backman, D. E., Beichman, C., & Neugebauer, G. 1986, ApJ, 310, 842

Goldsmith, M. J., Evans, A., Albinson, J. S., & Bode, M. F. 1990, MNRAS, 245, 119

Gonzalez, G., Lambert, D. L., Wallerstein, G., Rao, N. K., Smith, V. V., & McCarthy, J. K. 1998, ApJS, 114, 133

Gordon, K. D., et al. 2005, PASP, 117, 503

—. 2007, PASP, 119, 1019

Goswami, A., Karinkuzhi, D., & Shantikumar, N. S. 2010, ApJL, 723, L238

Griffin, M. J., et al. 2010, A&A, 518, L3

Guerrero, M. A., & Manchado, A. 1996, ApJ, 472, 711

Hachisu, I. 1986, ApJS, 61, 479

Han, Z. 1998, MNRAS, 296, 1019

Hecht, J. H., Holm, A. V., Donn, B., & Wu, C.-C. 1984, ApJ, 280, 228

Helou, G., & Walker, D. W., eds. 1988, Infrared astronomical satellite (IRAS) catalogs and atlases. Volume 7: The small scale structure catalog, Vol. 7

Hema, B. P., Pandey, G., & Lambert, D. L. 2012, ApJ, 747, 102

Herbig, G. H. 1964, ApJ, 140, 1317

Herwig, F. 2001, ApJL, 554, L71

Higdon, S. J. U., et al. 2004, PASP, 116, 975

Hinkle, K. H., Joyce, R. R., & Hedden, A. 2001, A&A, 367, 250

Hinkle, K. H., Lebzelter, T., Joyce, R. R., Ridgway, S., Close, L., Hron, J., & Andre, K. 2008, A&A, 479, 817

Hoffleit, D. 1958, AJ, 63, 50

—. 1959, AJ, 64, 241

Holm, A. V. 1999, Journal of the American Association of Variable Star Observers (JAAVSO), 27, 113

Houck, J. R., et al. 2004, ApJS, 154, 18

Iben, Jr., I., Tutukov, A. V., & Yungelson, L. R. 1996, ApJ, 456, 750

Ishihara, D., et al. 2010, A&A, 514, A1

Jeffery, C. S. 1995, A&A, 299, 135

Johnson, H. L. 1966, ARA&A, 4, 193

Jurcsik, J. 1996, Acta Astronomica, 46, 325

Kameswara Rao, N., & Lambert, D. L. 1993, AJ, 105, 1915

Kawada, M., et al. 2007, PASJ, 59, S389

Keenan, P. C., & Greenstein, J. L. 1963, Contr. Perk. Obs., 2

Kilkenny, D. 1982, MNRAS, 200, 1019

Kilkenny, D., & Whittet, D. C. B. 1984, MNRAS, 208, 25

Kraemer, K. E., Sloan, G. C., Wood, P. R., Price, S. D., & Egan, M. P. 2005, ApJL, 631, L147

Lambert, D. L., & Rao, N. K. 1994, Journal of Astrophysics and Astronomy, 15, 47

Lambert, D. L., Rao, N. K., Pandey, G., & Ivans, I. I. 2001, ApJ, 555, 925

Lawson, W. A., & Cottrell, P. L. 1989, MNRAS, 240, 689

—. 1997, MNRAS, 285, 266

Lawson, W. A., Cottrell, P. L., Kilmartin, P. M., & Gilmore, A. C. 1990a, MNRAS, 247, 91

—. 1990b, MNRAS, 247, 91

Lawson, W. A., et al. 1999, AJ, 117, 3007

Leavitt, H. S., & Pickering, E. C. 1906, Harvard College Observatory Circular, 122, 1

Lebouteiller, V., Barry, D. J., Spoon, H. W. W., Bernard-Salas, J., Sloan, G. C., Houck, J. R., & Weedman, D. W. 2011, ApJS, 196, 8

Lebouteiller, V., Bernard-Salas, J., Sloan, G. C., & Barry, D. J. 2010, PASP, 122, 231

Leech, K., et al. 2003, The ISO Handbook, Volume V - SWS - The Short Wavelength Spectrometer

Longland, R., Lorén-Aguilar, P., José, J., García-Berro, E., & Althaus, L. G. 2012, A & A, 542, A117

Loreta, E. 1935, Astronomische Nachrichten, 254, 151

Lundmark, K. 1921, PASP, 33, 314

Marang, F., Kilkenny, D., Menzies, J. W., & Jones, J. H. S. 1990, South African Astronomical Observatory Circular, 14, 1

Marraco, H. G., & Milesi, G. E. 1982, AJ, 87, 1775

Mathis, J. S., Rumpl, W., & Nordsieck, K. H. 1977, ApJ, 217, 425

McNaught, R. 1986, IAU Circ., 4245

McNaught, R. H., & Dawes, G. 1986, Information Bulletin on Variable Stars, 2928

Menon, A., Herwig, F., Denissenkov, P. A., Clayton, G. C., Staff, J., Pignatari, M., & Paxton, B. 2013, ApJ, 772, 59

Menzies, J. W., & Feast, M. W. 1997, MNRAS, 285, 358

Mitronova, S. N., Karachentsev, I. D., Karachentseva, V. E., Jarrett, T. H., & Kudrya, Y. N. 2004, Bulletin of the Special Astrophysics Observatory, 57, 5

Montiel, E. J., Srinivasan, S., Clayton, G. C., Engelbracht, C. W., & Johnson, C. B. 2015, AJ, 149, 57

Moshir, M., & et al. 1990, in IRAS Faint Source Catalogue, version 2.0 (1990)

Murakami, H., et al. 2007, PASJ, 59, 369

Nagendra, K. N., & Leung, C. M. 1996, MNRAS, 281, 1139

Neugebauer, G., et al. 1984, ApJL, 278, L1

O'Keefe, J. A. 1939, ApJ, 90, 294

Onaka, T., et al. 2007, PASJ, 59, S401

Pandey, G., Lambert, D. L., & Rao, N. K. 2008, ApJ, 674, 1068

Peek, J. E. G., et al. 2011, ApJS, 194, 20

Pickering, E. C. 1896, ApJ, 4

Pickering, E. C., & Fleming, W. P. 1896, ApJ, 4

Pickering, E. C., & Leland, E. F. 1896, ApJ, 4

Pigott, E., & Englefield, H. C. 1797, Royal Society of London Philosophical Transactions Series I, 87, 133

Pilbratt, G. L., et al. 2010, A&A, 518, L1

Poglitsch, A., et al. 2010, A&A, 518, L2

Pollacco, D. 1999, MNRAS, 304, 127

Pollacco, D. L., Hill, P. W., Houziaux, L., & Manfroid, J. 1991, MNRAS, 248, 1P

Pollacco, D. L., Lawson, W. A., Clegg, R. E. S., & Hill, P. W. 1992, MNRAS, 257, 33P

Rachford, B. L., et al. 2009, ApJS, 180, 125

Rao, N. K., & Lambert, D. L. 2008a, MNRAS, 384, 477

—. 2008b, MNRAS, 384, 477

Rao, N. K., & Lambert, D. L. 2010, in Recent Advances in Spectroscopy Theoretical, Astrophysical and Experimental Perspectives, ed. R. K. Chaudhuri, M. V. Mekkaden, A. V. Raveendran, & A. Satya Narayanan , 177

—. 2015, MNRAS, 447, 3664

Rao, N. K., Lambert, D. L., García-Hernández, D. A., Jeffery, C. S., Woolf, V. M., & McArthur, B. 2012, ApJL, 760, L3

Rao, N. K., & Nandy, K. 1986, MNRAS, 222, 357

Renzini, A. 1979, in ASSL Vol. 75: Stars and star systems, ed. B. E. Westerlund, 155

Renzini, A. 1990, in Astronomical Society of the Pacific Conference Series, Vol. 11, Confrontation Between Stellar Pulsation and Evolution, ed. C. Cacciari & G. Clementini, 549

Robitaille, T. P., Whitney, B. A., Indebetouw, R., Wood, K., & Denzmore, P. 2006, ApJS, 167, 256

Roussel, H. 2013, PASP, 125, 1126

Saio, H. 2008, in A. S. P. Conf. Ser., Vol. 391, Hydrogen-Deficient Stars, ed. A. Werner & T. Rauch, 69

Saio, H., & Jeffery, C. S. 2002, MNRAS, 333, 121

Schaefer, B. E. 1986, ApJ, 307, 644

Schlafly, E. F., & Finkbeiner, D. P. 2011, ApJ, 737, 103

Schlegel, D. J., Finkbeiner, D. P., & Davis, M. 1998, ApJ, 500, 525

Shears, J. 2011, ArXiv e-prints

Skrutskie, M. F., et al. 2006, AJ, 131, 1163

Sloan, G. C., Kraemer, K. E., Price, S. D., & Shipman, R. F. 2003, ApJS, 147, 379

Staff, J. E., et al. 2012, ApJ, 757, 76

Stansberry, J. A., et al. 2007, PASP, 119, 1038

Tisserand, P. 2012, A&A, 539, A51

Tisserand, P., Clayton, G. C., Welch, D. L., Pilecki, B., Wyrzykowski, L., & Kilkenny, D. 2013, A&A, 551, A77

Tisserand, P., et al. 2008, A&A, 481, 673

—. 2009, A&A, 501, 985

Ueta, T., et al. 2006, ApJL, 648, L39

—. 2014, A&A, 565, A36

van den Bergh, S. 1971, PASP, 83, 819

van Hoof, P. A. M., & van de Steene, G. C. 1999, MNRAS, 308, 623

Walker, H. J. 1985, A&A, 152, 58

Walker, H. J. 1986, in Astrophysics and Space Science Library, Vol. 128, IAU Colloq. 87: Hydrogen Deficient Stars and Related Objects, ed. K. Hunger, D. Schoenberner, & N. Kameswara Rao, 407

Walker, H. J., Heinrichsen, I., Richards, P. J., Klaas, U., & Rasmussen, I. L. 1996, A&A, 315, L249

Warner, B. 1967, MNRAS, 137, 119

Webbink, R. F. 1984, ApJ, 277, 355

Werner, M. W., et al. 2004, ApJS, 154, 1

Whitney, B. A., Wood, K., Bjorkman, J. E., & Cohen, M. 2003a, ApJ, 598, 1079

Whitney, B. A., Wood, K., Bjorkman, J. E., & Wolff, M. J. 2003b, ApJ, 591, 1049

Whittet, D. C. B. 2003, Dust in the galactic environment, 2nd edn. (Bristol: Institute of Physics (IOP) Publishing)

Woitke, P., Goeres, A., & Sedlmayr, E. 1996, A&A, 313, 217

Wolf, M. 1920, Astronomische Nachrichten, 211, 119

Woods, I. 1921, Harvard College Observatory Bulletin, 753, 2

Woods, I. E. 1928, Harvard College Observatory Bulletin, 855, 22

Wright, E. L., et al. 2010, AJ, 140, 1868

Yamamura, I., et al. 2009, in Astronomical Society of the Pacific Conference Series, Vol. 418, AKARI, a Light to Illuminate the Misty Universe, ed. T. Onaka, G. J. White, T. Nakagawa, & I. Yamamura, 3

Young, K., Phillips, T. G., & Knapp, G. R. 1993a, ApJ, 409, 725

—. 1993b, ApJS, 86, 517

Zaniewski, A., Clayton, G. C., Welch, D. L., Gordon, K. D., Minniti, D., & Cook, K. H. 2005, AJ, 130, 2293

Zhang, X., & Jeffery, C. S. 2012, MNRAS, 426, L81

Zhang, X., Jeffery, C. S., Chen, X., & Han, Z. 2014, MNRAS, 445, 660

Appendix. Permission to Reproduce Copyrighted Material

A.1 Copyright Agreement with AAS

The following is reproduced from the website of the Institute of Physics (IOP), which allows me the right to reproduce the materials in Chapter 3, for which I am the author and for which the manuscript has been cited in the text. It also will apply to the material presented in Chapter 4, which is currently in the process of submission:

Before your article can be published in an American Astronomical Society (AAS) journal, we require you to grant and assign the entire copyright in it to the AAS. The copyright consists of all rights protected by the copyright laws of the United States and of all foreign countries, in all languages and forms of communication, including the right to furnish the article or the abstracts to abstracting and indexing services, and the right to republish the entire article in any format or medium. In return, the AAS grants to you the non-exclusive right of republication, subject only to your giving appropriate credit to the journal in which your article is published. This non-exclusive right of republication includes your right to allow reproduction of parts of your article wherever you wish, and permits you to post the published (PDF) version of your article on your personal web site. To protect the copyright in your article, the original copyright notice as it appears in the journal should be included in the credit.

The AAS is eager for the information published in its journals to reach the widest possible audience and it encourages the reuse of figures, tables, or other materials in review articles, textbooks, and other appropriate means of scholarly communication. To ensure the long-term access of the research community to its archives, the AAS holds the copyright on all copyrightable materials published in its journals, but the Society grants control of the right to reproduce the material to the original authors as long as they are alive.

Hyperlink: http://iopscience.iop.org/0004-637X/page/Copyright+and+permissions

A.2 Permission to use Figure 1.2

Email correspondence between myself (edward.j.montiel@gmail.com) and Dr. Hideyuki Saio (saio@astr.tohoku.ac.jp):

Hi Dr. Saio,

As I'm sure that you already know, I'm Geoff Clayton's current graduate student working with him on the study of RCB stars. I'm writing to request permission to

reproduce Figure 3 from your 2008 conference proceeding (2008ASPC..391...69S) in my dissertation.

Cheers,

–

Hi Ed,

Sure. I am happy with the figure being reproduced in your dissertation. Good luck! Best wishes, Hideyuki Saio

A.3 Permission to use Figure 1.3

Email correspondence between myself (edward.j.montiel@gmail.com) and Dr. Geoffrey Clayton (gclayton@fenway.phys.lsu.edu):

Hi Geoff,

Do I have your permission to reproduce Figure 2 from your 2007 paper (2007ApJ...662.1220C) as Figure 1.3 in my dissertation?

–

yes

A.4 Permission to use Figure 1.4

Email correspondence between myself (edward.j.montiel@gmail.com) and Dr. Gajendra Pandey (pandey@iiap.res.in):

Hi Gajendra,

My name is Ed Montiel and I am currently a graduate student at LSU working with Geoff Clayton on RCB stars. I'm writing to ask for permission to reproduce Figure 1 from your 2008 paper on the discovery of 19F in RCB stars (2008ApJ...674.1068P) in my dissertation.

Cheers,

–

Dear Ed Montiel,

Yes, please go ahead with the reproduction.

All the best for your dissertation.

Gajendra Pandey

A.5 Permission to use Figure 1.5

Email correspondence between myself (edward.j.montiel@gmail.com) and Dr. Dana Backman[1] (dbackman@sofia.usra.edu):

Hi Dana,

My name is Ed Montiel and I am currently a graduate student at LSU working with Geoffrey Clayton. I'm in the process of finishing up my dissertation and am contacting you to ask for permission to reproduce Figure 2 from Gillett et al. (1986, ApJ...310..842G). LSU requires that permission be given for the reproduction of any

[1]Dr. Fred Gillett passed away in 2001. Dr. Backman is the second author on their 1986 paper

figures. Unfortunately, as you are certainly aware, Fred Gillett passed away back in 2001. I have already contacted the ApJ and they informed me that any of the remaining co-authors can provide consent and since you're next in line on the paper I've contacted you first.

If you aren't the D. E. Backman from that paper, then I apologize for the email.

Cheers,

– Hi, Ed,

I am that D. E. Backman. Fred Gillett and Gerry Neugebauer have both passed away.

I am pleased to grant you permission to reproduce the figure from our paper in your thesis.

Sincerely,

Dana Backman SOFIA /SETI Institute

A.6 Permission to use Figure 4.20

Email correspondence between myself (edward.j.montiel@gmail.com) and Dr. Geoffrey Clayton (gclayton@fenway.phys.lsu.edu):

I also need permission to reproduce Figure 2 from Clayton et al. (2013ApJ...771..130C) as my Figure 4.20.

–

yes

Vita

Edward Joseph Montiel was born June 1988 in Alexandria, VA. He graduated from T. C. Williams High School in June 2006 and then enrolled at The University of Arizona in Tucson, AZ in August of the same year. He received his Bachelor of Science in Astronomy and Applied Mathematics from The University of Arizona in May 2010. After graduation (June 2010) he began a job as a Research Specialist in the Infrared Group at Steward Observatory (Tucson, AZ). It was during this time he began to collaborate with Dr. Geoffrey Clayton, who would become his future thesis advisor. He left his job in May 2012 and enrolled in graduate school at Louisiana State University in August of the same year. He earned his M.S. degree in May 2015, and is expecting his doctoral degree in August 2016.